PHOTONIC INTEGRATION IN InGaAs/InGaAsP MULTIPLE-QUANTUM WELL LASER STRUCTURES USING QUANTUM WELL INTERMIXING

Bocang Qiu

January 1998

A thesis submitted to the Faculty of Engineering

of the University of Glasgow

for the degree of Doctor of Philosophy

Acknowledgements

I am extremely grateful to my supervisor Professor John Marsh for his guidance, encouragement and continual support throughout the duration of this project.

I would like to thank Dr. Catrina Bryce for her help, encouragement and patient correction to the draft of this thesis.

I also wish to express my sincere gratitude to those whose help and support have been proven to be very important to the success of this work. Dr. B.S. Ooi, Dr. Olek. Kowalski, Dr. Stewart McDougall, Dr. Fernado Camacho, Dr. Siyuan Yu, Dr. Andrew McKee, Dr. Karen McIlvaney, Dr. Steve Ayling.

Special thanks must go to the technical staff of the department particularly Jim Gray, Jimmy Young, Ian McNicholl, the dry etch team and all members of the cleanroom staff.

I would also like to acknowledge the practical assistance given by Chris Button at Sheffield University who supplied all of the epi-wafers used in this project.

I would like to thank all of my fellow post-graduate students and research assistants who helped to create a friendly and enjoyable atmosphere both within and outwith the department.

I would like to express my thanks to my family for their support, understanding, and love.

I was financially supported by a studentship under the Sino-British Friendship Scholarship Scheme (SBFSS) for a 3 year period, and by a departmental studentship for the final 4 months.

Abstract

The damage introduced into an InGaAs/InGaAsP quantum well structure during CH_4/H_2 reactive ion etching (RIE) processes was measured, for plasma powers from 20 W to 100 W, using low temperature photoluminescence. The damage depth profile is estimated to be around 12 nm - 70 nm after annealing at 500 °C for 60 seconds using a rapid thermal annealer (RTA). A reduced damage RIE process has been developed to fabricate InGaAs/InGaAsP multi-quantum well ridge waveguide lasers. The performance of these lasers has been compared to that of lasers fabricated from the same epilayer using wet etching to form the ridge. The resultant threshold currents were essentially indistinguishable, being 44.5 mA and 43 mA respectively for dry and wet etched lasers with 500 μm long laser cavities.

Quantum well intermixing in the InGaAs/InGaAsP material system was demonstrated using two techniques. The first was a laser irradiation process, which combines irradiation by continuous wave and Q-switched pulsed Nd:YAG lasers. Differential shifts up to 70 nm have been obtained. The second was a plasma process which involves sputtering a thin layer of SiO_2 and subsequent high temperature annealing using either a CW laser or rapid thermal annealer (RTA). Differential blue-shifts of the bandgap of up to 120 nm were obtained. The bandgap shift in the control regions is very insignificant. Measurement of the spatial selectivity of this technique shows that the spatial resolution is better than 50 μm.

The design, fabrication and characterisation for 3-dB MMI couplers were carried out using both as-grown (peak emission wavelength of 1.48 μm) and bandgap widened material. The measured results show good agreement with the design. A splitting ratio of around 0.12 dB (51:49) has been achieved for an MMI section length of 470 μm.

Low loss waveguides have been fabricated using the laser process. A loss as low as 2.1 dB/cm was obtained for an operation wavelength of 1.556 um.

Extended cavity ridge lasers (ECL) in InGaAs/InGaAsP multiple-quantum well structures have been successfully fabricated using the two QWI technique developed. The increases in threshold current were only 10 mA and 8 mA for cavity length of 800 μm active section and 1000 μm passive section, compared to the all active lasers with cavity length of 800 μm, and the losses in the passive sections of ECLs were calculated which were 2.4 cm^{-1} and 4.4 cm^{-1}, for the two processes, respectively.

Considerable theoretical work was carried out, which included the calculation of the optical confinement and gain in the InGaAs/InGaAsP MQW structure used throughout this thesis. Modelling of the intermixing of quantum wells was also performed and the results indicate that the changes of bulk bandgap energy are mainly responsible for the blue-shift of the photoluminescence.

Publications

Journal Publications

1. B.C. Qiu, B.S. Ooi, A.C. Bryce, S.E. Hicks, C.D.W. Wilkinson, R.M. De La Rue and J.H. Marsh, "Reduced damage reactive ion etching process for fabrication of InGaAsP/InGaAs multiple quantum well ridge waveguide lasers", J. Vac. Sci. and Technol. **(B)16**, pp.1818-1822, 1998

2. B.C. Qiu, A.C. Bryce, R.M. De La Rue, and J.H. Marsh, "Monolithic integration in InGaAsP/InP multiple quantum well structures using laser processing", IEEE Photonics Technol. Lett., **10**, pp. 769-771, 1998

3. J.H. Marsh, O.P. Kowalski, S.D. McDougall, B.C. Qiu, A. McKee, C.J. Hamilton, R.M. De La Rue, A.C. Bryce, "Quantum well intermixing in material system for 1.5 μm", J. Vac. Sci. and Technol. (A), **16**, pp. 810-816, 1998

4. Stewart D. McDougall, Olek P. Kowalski, Craig J. Hamilton, Fernando Camacho, Bocang Qiu, Maolong Ke, Richard M. De La Rue, A. Catrina Bryce, John H. Marsh, "Monolithic integration via a universal damage enhanced quantum well intermixing technique", Accepted by IEEE J. Selected Topics on Quantum Electron.

5. B. C. Qiu, C.J. Hamilton, M. Ke, O. P. Kowalski, S.D. Mcdougall, A. C. Bryce and J.H. Marsh, "Extended Cavity Lasers in InGaAs-InGaAsP and GaInP-AlGaInP Multi-Quantum Well Structure Using Sputtered SiO_2 Technique", Accepted by Japanese J. of Appli. Phys. Special issue on "Indium Phosphide and Related Materials"

Conference Publications

1. A.C. Bryce, R.M. De La Rue, and J.H. Marsh, B.S. Ooi, B. Qiu, "Quantum well intermixing in GaInAs/GaInAsP and GaAs/AlGaAs structures using pulsed laser irradiation", MRS Symposium Proceedings, Vol. 450, pp. 413-418 (1996)

2. B.C. Qiu, B.S. Ooi, A.C. Bryce, S.E. Hicks, C.D.W. Wilkinson, R.M. De La Rue and J.H. Marsh, "Low damage reactive ion etching process for fabrication of ridge waveguide lasers", IRPM'97 Proceedings, pp. 578-581 (1997).

3. A. McKee, G. Lullo, C.J. McLean, B.C. Qiu, A.C. Bryce, R.M. De La Rue, and J.H. Marsh, "Extended cavity lasers fabricated using photo-absorption induced disordering", IRPM'97 Proceedings, pp. 288-291 (1997).

4. B.C. Qiu, O.P. Kowalski, A.C. Bryce, R.M. De La Rue and J.H. Marsh, "Monolithic integration in InGaAsP/InP multiple quantum well structures using laser and plasma processing", Proceedings of IEE Colloquium on Optoelectronic Integration and Switching (1997)

5. B. C. Qiu, C.J. Hamilton, M. Ke, O. P. Kowalski, S.D. Mcdougall, A. C. Bryce and J.H. Marsh, "Extended Cavity Lasers in InGaAs-InGaAsP and GaInP-AlGaInP Multi-Quantum Well Structure Using Sputtered SiO_2 Technique", IPRM'98 proceedings (1998)

Contents

1. Introduction

2. InGaAs/InGaAsP MQW Laser Structures

3. Quantum Well Intermixing Using Laser Process and Plasma Process

4. Multimode Interference Coupler Design, Fabrication and Characterisation

7. Fabrication of Extended Cavity Ridge Waveguide Laser

8. Conclusions and Future Work

1. Introduction

1.1 The Significance of Monolithic Integration

Monolithic integration of semiconductor optical devices, as in the implementation of various functions with light, such as generation, modulation, switching, and detection onto one substrate, offers similar advantages to those from Si based integrated electronics circuits. These advantages include the elimination of problems due to vibration and alignment associated with discrete components, because of the improved mechanical stability and reliability. Another advantage is device miniaturisation, which leads to the potential for fabrication economy of devices, and enhanced performance such as higher speed operation than that of their bulk counterparts.

Monolithic integration potentially has a wide range of applications in optoelectronics. In Particular, with the advances in high speed and large capacity optical fibre communications, monolithic integration in long wavelength material systems e.g. InGaAs-InGaAsP, is increasingly important. Examples of key devices (mostly applying monolithic integration of different optical functional components) for optical time division multiplexing (TDM) systems are:

Monolithic mode-locked pulse lasers for the generation of a pulse stream [1] and optical clock recovery on the receiver side incorporating segments for optical amplification, wavelength selective reflection and wavelength tuning (DBR grating) and modulation.

High speed electroabsorption devices [2] for data modulation.

Integrated interferometers (consisting of semiconductor amplifier, passive waveguides, and combiners/splitters) for add/drop and MUX and DMUX applications [3,4].

For wavelength division multiplexing (WDM) systems, typical examples for monolithic integration are wavelength converter[5], space switches [6,7]. Figs. 1.1-1.3 show some examples of monolithically integrated devices. In the configuration of Fig. 1.1, the passive waveguide has a wider bandgap than that of the other sections. In Fig. 1.2-1.3, apart from the semiconductor optical amplifiers (SOA), the other parts of the configurations are passive, and therefore require a wider bandgap.

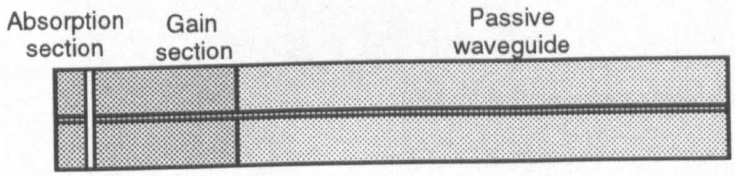

Fig. 1.1 Monolithic integration of a gain section and an absorption section with a passive waveguide section for short pulse generation.

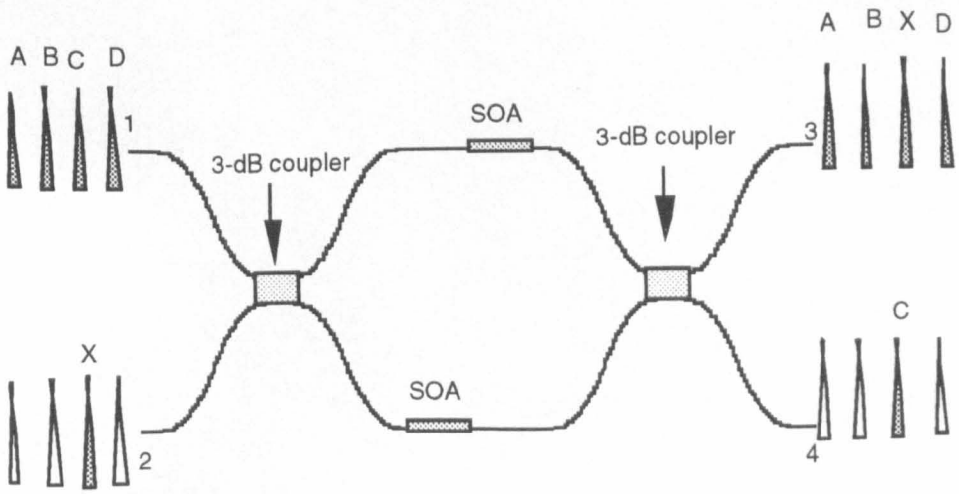

Fig. 1.2 Monolithically integrated asymmetric Mach-Zehnder interferometer as add/drop multiplexer, after [3].

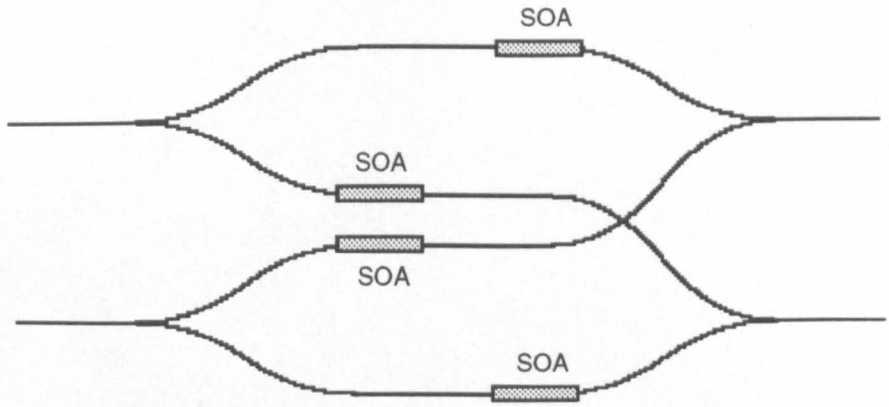

Fig. 1.3 Monolithically integrated 2x2 InGaAsP/InP Laser amplifier gate switch arrays, after [7].

1.2 Approaches to the Monolithic Integration

Integrating optoelectronic devices, however, presents many problems that do not exist in standard silicon based processing. The fundamental problem with optoelectronic integration is the requirement to produce areas with different electrical and optical properties, e.g. different emission wavelengths, on a single substrate. This is a far more complex problem than producing areas with only different electrical properties, which can easily be achieved by introducing the correct amount of electrically active dopants to selected area of the material. Many different processes have been developed towards this end, which include multiple growth steps, selective area growth, vertical mode coupling, and quantum well intermixing (QWI).

1.2.1 Multiple Growth Epitaxy [8]

This approach involves the multiple growth of distinct active layers for different components of a monolithically integrated device, e.g. an integration of a laser with a modulator. Generally, a laser active layer with bandgap E_{g1} is grown over a whole wafer, followed by selective etching and subsequent regrowth of the layer for passive

devices, with bandgap E_{g2}. Obviously, it is desirable that the losses in the passive region are low, and consequently, $E_{g1} < E_{g2}$ is required. Although this method allows independent design of the layers for active and passive devices, critical etching and regrowth are required, especially to achieve efficient optical coupling between the two waveguides. The disadvantages associated with this technique are low yields and the requirement of an expensive regrowth process.

1.2.2 Selective Area Growth [9, 10]

By growing on InP substrates patterned with dielectric masks, selective area growth has been successfully demonstrated using MOCVD [10] and metalorganic MBE (MOMBE) [11]. This technique is based on the fact that the dielectric mask inhibits epitaxial growth of material, which means that some of the material which would have grown in the masked regions will be deposited in gaps opened up in the mask, resulting in a local increase in the growth rate and therefore a longer emission wavelength than from unmasked regions due to the larger quantum well width. Epitaxial layer bandgap energies are hence mainly controlled by the geometry of the lithographically defined dielectric patterns.

1.2.3 Vertical Mode Coupling [11]

In this case two MQW active layers with different bandgap are grown in one growth step, the layer with a narrower bandgap being on top of the other, separated by a thin InP spacer layer. Selective wet chemical etching allows localised removal of the top layer in selected areas. This is followed by a regrowth of the cladding layer for the second waveguide in some regions. Again the drawback of this technique is that a regrowth stage is required.

1.2.4 Quantum Well Intermixing [12]

Quantum well intermixing is a simple and flexible technique for the implementation of photonic integrated circuits (PICs). In a quantum well (QW) system, a permanent change in the absorption edge can be accomplished by intermixing the wells and the barriers, which leads to a change of bulk bandgap of materials as well as changes of the well width and barrier height, the values of which determine the energy of the quantum-confined states relative to the bulk bandgap. In the limit of complete intermixing, a semiconductor alloy, with average composition of the wells and barriers, is formed, but less extreme intermixing produces structures of intermediate bandgap in which the 2-D properties of the QW layers are partially retained. However, intermixing is only of use if it can be localised to particular areas of the wafer, and if the electrical and optical qualities of the processed material are adequate for use in devices.

The first intermixing studies were performed on GaAs-AlGaAs structures [13], and since then various methods have been developed, including impurity induced disordering (IID) [14], impurity-free vacancy disordering (IFVD) [15, 16], laser processing induced disordering [17], and plasma processing induced disordering [18]. These methods have been applied to the InGaAs-InGaAsP system with varying degrees of success.

In IID processes, an impurity is introduced into an epitaxial wafer and the wafer is then annealed. During the annealing step the layers intermix and ion-implantation damage, if present, is to a large extent removed. Current understanding of the IID process suggests that the role of impurities is to induce disordering through the generation of free carriers which, in turn, increase the equilibrium number of vacancies at the annealing temperature.

Like IID, IFVD is also based on creating vacancies in the III-V semiconductor. However, this technique does not require impurities to be introduced by either ion implantation or diffusion, but relies on atoms diffusing out selectively from the material into dielectric caps

at high temperatures, causing vacancies to be generated at the surface which diffuse rapidly through the material and cause intermixing. Lee et al [15] have achieved differential blue shifts of up to 185 meV using SiO_2 and SiN_x dielectric layers, in InGaAs/InP material structures. Using phosphorus-doped silicon-dioxide (SiO_2:P) as a cap layer, Ramdane et al [15] have reported differential blue shifts of up to 80 nm in the capped region after annealing with rapid thermal annealer (RTA), compared to the uncapped regions. Using this technique, they have demonstrated the monolithic integration of an InGaAsP-InP DFB (distributed feedback) laser with a modulator.

Laser processing induced disordering, using either CW or pulsed laser irradiation [16], or a combination of the two [18], as well as plasma induced disordering [17] which are investigated in this project, will be described in detail in chapter 3.

1.3 Thesis Outline

This research is concerned with monolithic integration in the InGaAs/InGaAsP material system, using QWI. In chapter 2, the basic properties of InP and related compound alloys are briefly reviewed; some important parameters in a quantum well structure are also discussed. Chapter 3 is concerned with QWI, in which QWI using laser processing and plasma process are addressed. Chapter 4 is concerned with the design, fabrication and assessment of 3-dB MMI couplers. The devices were fabricated using both as-grown and bandgap shifted material. Chapter 5 is concerned with RIE dry etch damage, in which RIE dry etch damage was assessed using a specially designed multiple-quantum well (MQW) probe structure and low temperature (5 K) photoluminescence techniques. In chapter 6, fabrication of ridge waveguide lasers is presented, also the optical gain and confinement coefficient in the material structure are discussed. Chapter 7 documents the fabrication results of extended cavity ridge lasers, a demonstration of monolithic integration of lasers and passive waveguides using QWI developed in chapter 3. In Chapter 8 the conclusions of the work are discussed.

References

1. P.B. Hansen, G. Raybon, U.Koren, P.P. lannone, B.I. Miller, G.M. Young, M.A. Newkirk, and C.A. Burrus, "InGaAsP monolithic extended-cavity lasers with integrated satureable absorbers for active, passive, and hybrid mode locking at 8.6 GHz", Appl. Phys. Lett., **62**, pp. 1445-1447, 1993

2. A. Ramdane, F. Devaux, N. Souli, D. Delprat, and A. Ougazzaden, "Monolithic integration of multiple-quantum-well lasers and modulators for high-speed transmission", IEEE J. Selec. Topics in Quantum Electron., **2**, pp. 326-335, 1996

3. E. Jahn, N. Agrawal, H.-J., Ehrke, R. Ludwig, W. Pieper, and H.G. Weber, "Monolithically integrated asymmetric Mach-Zehnder interferometer as a 20 Gbit/s all-optical add/drop multiplexer for OTDM", Electron. Lett., **32**, pp. 216-217, 1996

4. E. Jahn, N. Agrawal, M. Arbert, H.-J., Ehrke, D. Franke, R. Ludwig, W. Pieper, H.G. Weber, and C.W. Weinert, "40 Gbit/s all-optical demultiplexing using a monolithically integrated Mach-Zehnder interferometer with semiconductor laser amplifiers", Electron. Lett., **31**, pp. 1857-1858, 1995

5. B. Mikkelsen, P.B. Hansen, K.E. Stubkjaer, K. Wunstel, K. Daub, E. Lach, G. Laube, W. Idler, M. Schilling, S. Bouchoule, "40Gbit/s all-optical wavelength converter and RZ-to-NRZ format adapter realised by monolithic integrated active Michelson interferometer", Electron. Lett., **33**, pp. 133-134, 1997

6. M. Renaud, M. Bachmann, M. Erman, "Semiconductor optical space switches", IEEE Journal of Selected Topics in Quantum Electronics, **2**, pp. 277-288, 1996

7. M. Janson, L. Lundgren, A.C. Morner, M. Rask, B. Stoltz, M. Gustavsson, And L. Thylen, "Monolithically integrated 2x2 InGaAsP/InP laser-amplifier gate switch arrays", Electron Lett., **28**, pp. 776-777, 1992

8. W. Passenberg, W. Schlaak, A. Umbach, "MBE regrowth on planar and patterned In(GaAs)P layers for monolithic integration", Institute of Physics Conference Series, No. **155**, pp. 235-238, 1997

9. L. Silvestre, A. Ougazzaden, D. Delprat, A. Ramdane, C. Daguet, and G. Patriarche, "Study of growth rate and composition variations in metalorganic vapour phase selective area epitaxy at atmospheric pressure and application to the growth of strained layer DBR lasers", Journal of Crystal Growth, **170**, pp. 639-644, 1997

10. H. Heinecke, "Selective-area growth of III/V materials in metalorganic molecular-beam epitaxy (chemical beam epitaxy)", Journal of Crystal Growth, **136**, pp. 18-28, 1994

11. L. Xu, M.R. Gokhale, P. Studenkov, J.C. Dries, C.P. Chao, D. Garbuzov, and S.R. Forrest, " Monolithic integration of an InGaAsP-InP MQW laser/waveguide using a twin-guide structure with a mode selection layer", IEEE Photonics Technol. Lett., **9**, pp. 569-571., 1997

12. J.H. Marsh, "Quantum well intermixing", Semiconductor Science and Technology, **8**, pp. 1136-1155, 1993

13. W.D. Laidi, N. Holonyak, M.D. Camras, K. Hess, J.J. Coleman, P.D. Dapkus, J. Bardeen, "Disorder of an AlAs-GaAs super-lattice by impurity diffusion", Appl. Phys. Lett., **38**, pp.776-778, 1981

14. S.A Schwarz, P. Mei, T. Venkatesan, R. Bhat, D.M. Hwang, C.L. Schwartz, M. Koza, L. Nazar, B.J. Skromme, "InGaAs/InP superlattice mixing induced by Zn or Si diffusion", Appl. Phys. Lett., **53**, pp.1051-1053, 1988

15. J.H. Lee, S.K. Si, Y.B. Moon, E.J. Yoon, and S.J. Kim, "Bandgap tuning of $In_{0.53}Ga_{0.47}As$ cap layer and SiO_2 dielectric capping", Electron Lett., **33**, pp. 1179-1180, 1997

16. A. Ramdane, P. Krauz, E.V.K. Rao, A. Hamoudi, A. Ougazzaden, D. Robein, A. Gloukhian, and M. Carré "Monolithic integration of InGaAsP-InP strained layer distributed feedback laser and external modulator by selective quantum-well intermixing", IEEE Photonics. Technol. Lett., **7**, pp. 1016-1018, 1995

17. A. McKee, C. J. McLean, G. Lullo, A. C. Bryce, R. M. De La Rue, and J. H. Marsh, "Monolithic integration in InGaAs-InGaAsP multiple-quantum-well structures using laser intermixing", IEEE J. of Quantum Electron. **33**, pp. 45-55, 1997

18. J.H.Marsh, O.P. Kowalski, S.D. McDougall, B.C. Qiu, A. McKee, C.J. Hamilton, R.M. De La Rue, A.C. Bryce, "Quantum well intermixing in material systems for 1.5 μm" , J. of Vacuum Science and Technol. (A), **16**, pp.810-816, 1998

2. InGaAs/InGaAsP MQW Laser Structures

2.1 Introduction

High speed and long haul optical fibre communication requires light sources which emit light in the wavelength range of 1.3-1.6 μm, due to the fact that the minimum loss of silica fibre is located at 1.55 μm. The InP-based InGaAsP quaternary material system is ideal for such devices, as the direct bandgap of the material system can be precisely tailored by controlling the relative proportion of each element. In this chapter, the properties of InP and related alloys are briefly reviewed. This is followed by a discussion of the energy levels and density of states in a one dimensional confined quantum well, the parameters of which are related to many important electrical and optical properties of the material. The optical absorption spectrum is then presented, and finally the effects of an electric field on the properties of quantum well are discussed.

2.2 The Bonding and Crystal Structure of Indium Phosphide and Related Materials

InP crystallises in the cubic zinc blende (sphalerite) structure, which consists of two interpenetrating fcc lattices, one shifted by $a/4$ [111] relative to the other fcc lattice (a being the length of the fcc cube edge). The two fcc lattices are occupied by two different atoms, for example, In and P. The cubic unit cell of a sphalerite structure is shown in Fig. 2.1.

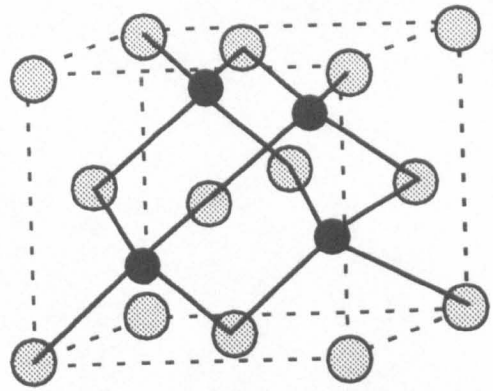

Fig. 2.1 Crystal structure of InP and related compounds

If the coordinates of the group III atoms are 000, 0 1/2 1/2, 1/2 0 1/2, 1/2 1/2 0, those of the group V atoms are 1/4 1/4 1/4, 1/4 3/4 3/4, 3/4 1/4 3/4, 3/4 3/4 1/4. Each group III atom has four nearest neighbour group V atoms, 12 next-nearest neighbour group III atoms and so on. The sphalerite structure does not have inversion symmetry because the arrangement of atoms along the body diagonal is in the the order AB..AB..AB (where dots represent vacant sites), and so is not invariant under inversion.

Since each fcc lattice has four atoms per unit cell, there are four molecules of the compound AB per unit cell in the sphalerite structure. In the unit cell, the atoms are arranged such that for each group III atom there are four equally distant group V atoms arranged at the corners of a regular tetrahedron, and vice versa. The tetrahedral arrangement is the result of the covalent bonding of the eight valence electrons per molecule in sp^3 hybridised orbital. The bonding is not, however, entirely covalent since there is some charge transfer between the two types of atoms, giving rise to a partial ionic character in the bonding. For InP, 42% of the bonding is estimated to be ionic [1].

2.3 Energy Band Structure

The calculated energy band structure of InP is shown in Fig. 2.2 [2].

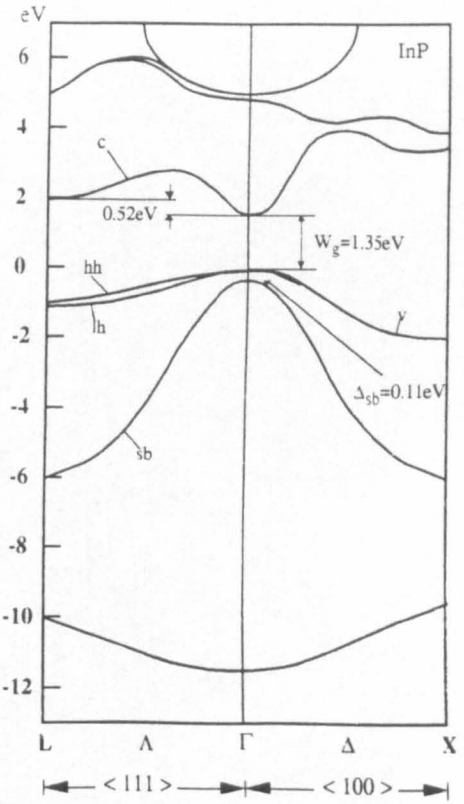

Fig.2.2 Band Structure of indium phosphide

It is customary to associate the most important (high symmetry) points with capital letters Γ, X, L etc. These points lie at the Brillouin zone centre and at the boundaries, along the high-symmetry lines that are normally referred to in terms of the Miller indices. For example, the Γ-X direction is the main cubic axis <001>, if X is the point in **k**-space whose x and y components are zero. The Γ-L direction lies along the line connecting the nearest neighbours in the lattice, i.e., along the <111> direction. Both the valence band maxima and the lowest conduction band minimum occur at k=0, the Γ point, i.e., InP is a direct bandgap semiconductor. Higher conduction band minima occur in the ‹100› (Δ) and ‹111› (Λ) directions, as can be seen in Fig. 2.2. The L and X minima are, respectively, 0.4 eV and 0.7 eV above the Γ_1 minimum[2]. In the valence band, there are subbands whose maxima occur at same k point, i.e., at Γ, and so are said to be degenerate. The band with smaller curvature is labelled the heavy hole (hh) band, while the other one

which has larger curvature is called the light hole (lh) band, as the effective mass is inversely proportional to the second derivative of E with respect to K. The split-off band (sb) lies at lower energy than the lh and hh bands with a separation of energy at Γ of 0.11 eV. If uniaxial strain is applied to the semiconductor, the shear component of the strain splits the degeneracy of the heavy and light hole bands[3]. This is particularly evident in heterostructures due to lattice-mismatch strain[4-7]. The band structure of InGaAsP compounds lattice matched to InP is similar to that shown in Fig. 2.2.

2.4 Material Parameters of $In_{1-x}Ga_xAs_yP_{1-y}$ Alloy Semiconductors

For $In_{1-x}Ga_xAs_yP_{1-y}$ to be lattice matched to an InP substrate, the following conditions [8,9] are required:

$$x \approx 0.47y \tag{2.1}$$

or more rigidly

$$x \approx \frac{0.1894y}{0.4184 - 0.013y} \tag{2.2}$$

2.4.1 Bandgap Energy

GaInAsP lattice matched to InP has a direct bandgap over the entire range of alloy compositions. The bandgap can be expressed as function of element composition as following [9]:

$$E_0(y) = 1.35 - 0.72y + 0.12y^2 \tag{2.3}$$

2.4.2 Effective Mass in Ternary and Quaternary Alloys

According to the k.p approximation[10], the effective mass of the carrier, m^*, is given by

$$\frac{1}{m^*} = \frac{1}{m} + \frac{2p^2}{3\hbar^2}\left(\frac{2}{E_g} + \frac{2}{E_g + \Delta}\right) \tag{2.4}$$

where p is the matrix element connecting the conduction band and the light hole and spin-orbit split valence bands, and E_g and Δ are the bandgap and valence band splitting energies of the material. It has been found for many ternary alloys that, if the effective mass is calculated under the assumption that p^2 varies linearly between the values for the binary compounds, the results do not agree well with experimental values. The origin of this discrepancy has been attributed to disorder-induced mixing of the reduced p^2. Much experimental work has been conducted on this issue. Although there are some discrepancies, the generally accepted effective mass for the electron is[9]

$$\frac{m^*}{m_0} = 0.08 - 0.039y \tag{2.5}$$

The hole effective masses are[11]

$$\frac{m^*_{hh}}{m_0} = 0.046 \tag{2.6}$$

$$\frac{m^*_{lh}}{m_0} = 0.120 - 0.099y + 0.030y^2 \tag{2.7}$$

for heavy and light holes, respectively. Here m_0 is the free electron mass.

2.4.3 Refractive Index

One of important factors in the design of heterostructure lasers and optoelectronic devices is refractive index, n. Often knowledge of n as function of photon energy near and below the bandgap is required. Several models have been proposed to obtain n as function of photon energy and composition in ternary and quaternary alloys. In many models the

starting point for calculating n in alloys is semiempirical. Afromowitz[12] proposed a modified single oscillator model to explain dispersion of n near the bandgap. In this model, n^2 is expressed as

$$n^2 - 1 = \frac{Ed}{E0} + \frac{Ed E^2}{E0^3} + \frac{\eta E^4}{\pi} \ln\left(\frac{2E0^2 - Eg^2 - E^2}{Eg^2 - E^2}\right) \qquad (2.8)$$

$$\eta = \frac{\pi E_d}{2E_0^3(E_0^2 - E_g^2)} \qquad (2.9)$$

$$E_0 = 0.595x^2(1-y) + 1.626xy - 1.891y + 0.524x + 3.391 \qquad (2.10)$$

$$E_d = (12.36x - 12.71)y + 7.54x + 28.91 \qquad (2.11)$$

$$E = \frac{1.24}{\lambda} \qquad (2.12)$$

where λ is wavelength in μm.

Using experimental results and an interpolation technique, Adachi [11] obtained the following relationship:

$$n^2 = 9.55 + 2.2y \qquad (2.13)$$

Reference [13] also gives a expression of refractive index for $In_{1-x}Ga_xAs_yP_{1-y}$:

$$n^2 = (1-y)[8.4x + 9.6(1-x)] + y[13.1x + 12.2(1-x)] \qquad (2.14)$$

2.5 Energy Levels in Quantum Well (QW) Structures

The schematic of a QW structure, along with the band diagram, are shown in Fig. 2.3, where L_w and L_b are well and barrier thicknesses, respectively. ΔE_c, and ΔE_v are conduction valence band offsets of InGaAs/InGaAsP heterostructure.

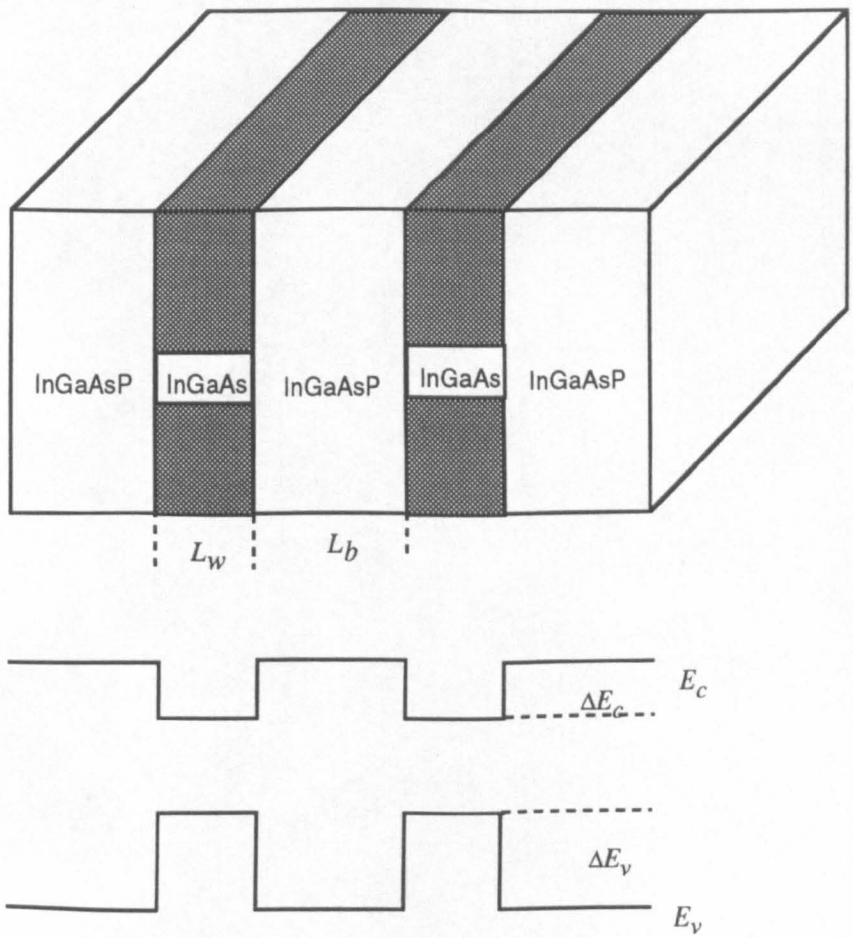

Fig. 2.3 Schematic representation of a QW formed by heterostructure

If the dimension L_w is comparable to the de Broglie wavelength, the kinetic energy corresponding to particle motion along the z direction is quantized. The energy can be obtained by separating the Hamiltonian into energies corresponding to x, y and z directions. For the x and y directions, the energy levels form a continuum of states given by

$$E = \frac{\hbar^2}{2m^*}(k_x^2 + k_y^2) \tag{2.15}$$

where m^* is the effective mass of the carrier, and k_x and k_y are the wave vectors along the x and y directions, respectively. Thus the electrons and holes may be viewed as forming a two-dimensional Fermi gas.

The energy levels in the z direction are obtained by solving Schrödinger's equation for a one dimensional potential well. It is given by

$$-\frac{\hbar^2}{2m}\frac{d\Psi^2}{dz^2} = E\Psi \qquad (0 \le z \le L_z) \tag{2.16}$$

$$-\frac{\hbar^2}{2m}\frac{d^2\Psi}{dz^2} + V\Psi = E\Psi \qquad (z \ge L_z;\ z \le 0) \tag{2.17}$$

where Ψ is the Schrödinger wavefunction, and V is the depth of the potential well. For the limiting case of an infinite well, the energy levels and the wavefunctions are

$$E_n = \frac{\hbar^2}{2m}\left(\frac{n\pi}{L_z}\right)^2 \tag{2.18}$$

and

$$\Psi_n = A\sin\frac{n\pi z}{L_z} \qquad (n=1,\ 2,\ 3,\ \ldots) \tag{2.19}$$

where A is a normalisation constant. Fig. 2.4 shows the first three wavefunctions in a square well of infinite depth. For very large L_z, Equation (2.18) yields a continuum of states, and the system no longer exhibits quantum effects.

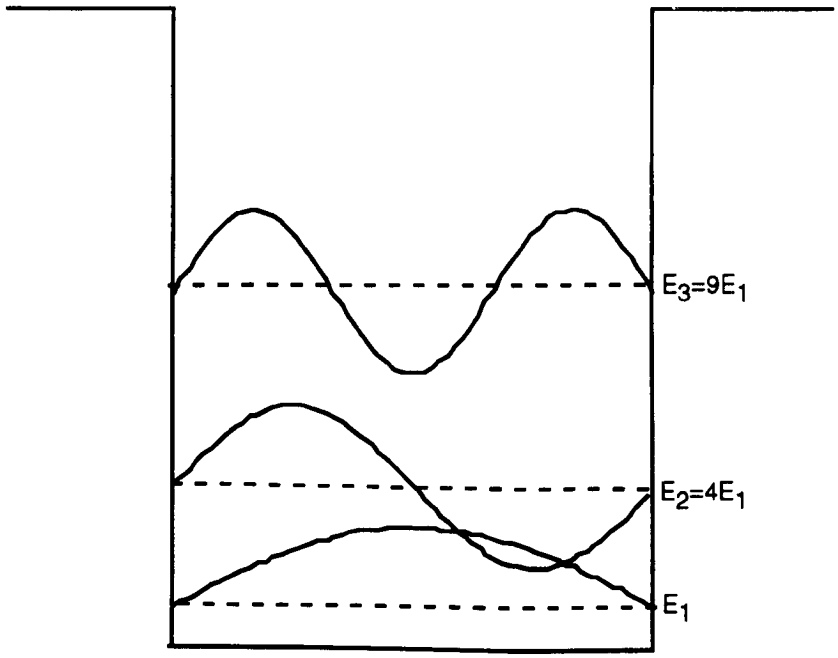

Fig. 2.4 Wavefunctions and eigenenergies in a square QW of infinite depth

However, most of the QW structures in which we are interested in practice do not follow the case of an infinite well. For example, the well shown in Fig. 2.5 is a typical $In_{0.53}Ga_{0.47}As$/InGaAsP quantum well structure which is used in lasers operating at 1.55 μm. Here it is assumed that the bandgap energy of the barriers correponds to a wavelength of $\lambda g=1.2$ μm.

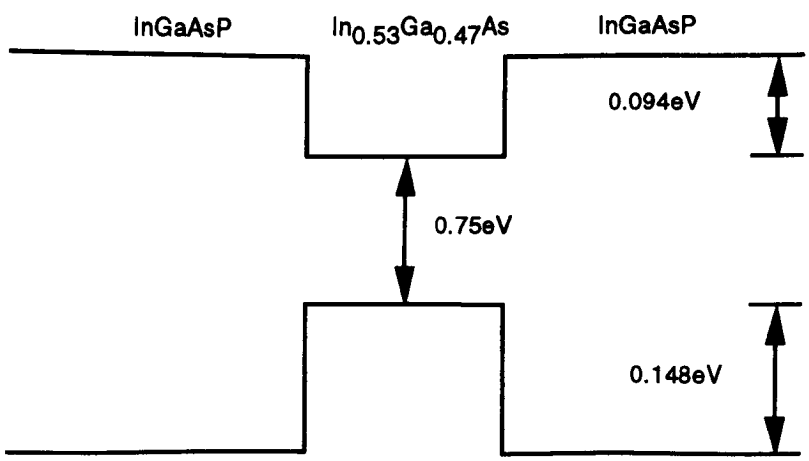

Fig. 2. 5 $In_{0.53}Ga_{0.47}As$/InGaAsP quantum well.

For a finite well, the wavefunction, which can be obtained from equations (2.16) and (2.17) using the boundary conditions that Ψ and $\frac{d\Psi}{dz}$ are continuous at the interfaces $z=0$ and $z=L_z$, is

$$\Psi = A\sin(\alpha z) + B\cos(\alpha z) \qquad (0 \le z \le L_z) \tag{2.20}$$

$$\Psi = C\exp(-\beta z) + D\exp(\beta z) \qquad (z \ge L_z;\ z \le 0) \tag{2.21}$$

The energy levels can be found by solving the following eigenvalue equation

$$(\alpha L_z)^2 + (\beta L_z)^2 = \frac{8m^* V L_z^{\,2}}{\hbar^2} \tag{2.22}$$

In the valence band, the wavefunction must be solved for both light and heavy holes, since they have different effective masses. Table 2.1 lists the calculated energy levels, measured from the bottom of the well, of both the electrons and heavy holes in the quantum well shown in Fig. 2.5 with different well widths, and the corresponding wavefunctions are plotted in Fig. 2.6.

Table 2.1 Energy levels in a typical laser QW with different well widths

Well width (Å)	E1c (meV)	E2c (meV)	E1hh (meV)	E2hh (meV)	E3hh (meV)
40	68.8		26.6	99.0	
60	53.3		14.5	56.5	119
80	41.5		9.1	35.8	78.7
100	32.8		6.2	24.6	54.7
120	26.5	87.4	4.5	17.9	40.0

It is should be pointed out that, during the calculation, the offsets of ΔE_c and ΔE_v are taken from reference [13]:

$$\frac{\Delta E_c}{\Delta E} = 0.39 \tag{2.23}$$

$$\frac{\Delta E_v}{\Delta E} = 0.61 \tag{2.24}$$

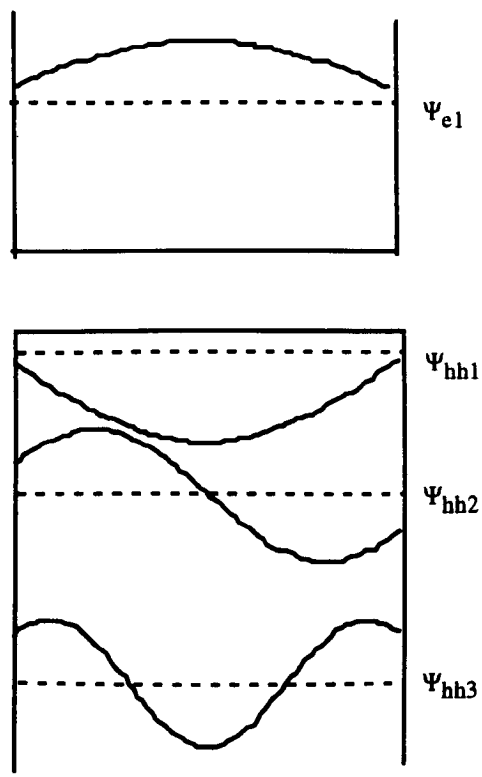

Fig. 2.6 Wavefunctions for a quantum well of finite depth

From the calculation above, it is obvious that the emission wavelength of the InGaAs/InGaAsP well structure is dependent on the well width due to quantum confinement effects. This is plotted in Fig. 2.7.

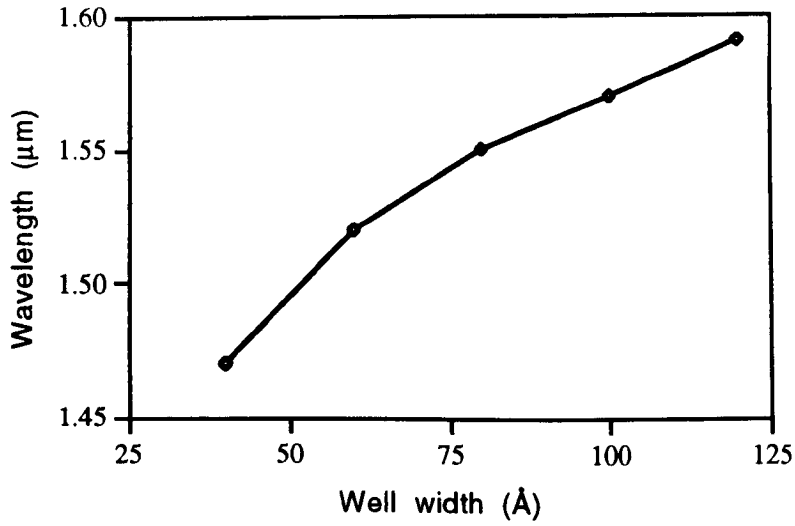

Fig. 2.7 Emission wavelength as a function of well width

2.6 Density of States

2.6.1 Density of States in Bulk Material

Another important aspect of semiconductor structure is the density of electronic states. To determine the density of states, the existing electronic states in the crystal must first be determined. Assuming a bulk crystal of dimensions L_x, L_y, L_z, it is certain that the electron wavefunction must go to zero at the edges of the crystal. Applying this boundary condition to the solution of Schrödinger's equation, it is found that the electron's $\mathbf{k}$ vector components, i.e., $\mathbf{k}_x$, $\mathbf{k}_y$, and $\mathbf{k}_z$ must be such that $\sin(\mathbf{k}_x.0) = \sin(\mathbf{k}_x.L_x) = 0$, and likewise for the components in other two directions. Thus we quickly conclude that the discrete set of $\mathbf{k}$ vector states an electron can have is given by

$$\mathbf{k} = n_x\mathbf{k}_x + n_y\mathbf{k}_y + n_z\mathbf{k}_z \tag{2.25}$$

where

$$|\mathbf{k}_i| = \frac{\pi}{L_i} \tag{2.26}$$

the n_i are quantum numbers of the system, which can take on both positive and negative nonzero integer values. It should be noted, however, that physically distinct states depend only on ($|n_x|$, $|n_y|$, $|n_z|$). The $\mathbf{k}_i$ represent vectors along the three orthogonal directions in $\mathbf{k}$ space, the magnitudes of which are inversely proportional to the length of the crystal in that direction. To derive the density of states function $D(\mathbf{k})$, we must first develop a method for counting the states. From the equations above, it can be seen that each state occupies a volume $\frac{\pi^3}{L_x L_y L_z}$ in $\mathbf{k}$ space, or

$$D(\mathbf{k}) = \frac{L_x L_y L_z}{\pi^3} \tag{2.27}$$

If we allow $\mathbf{k}$ to expand to $\mathbf{k} + d\mathbf{k}$, the number of states is given by the volume $\frac{1}{2}\pi k^2 dk$ times the density of points in $\mathbf{k}$ space,

$$N_k dk = \left(\frac{L_x L_y L_z}{\pi^3}\right)\left(\frac{1}{2}\pi k^2 dk\right) \tag{2.28}$$

Due to the fact that the an electron has two possible spin states, equation (2.28) must be multiplied by a factor of 2, and the density of states in $\mathbf{k}$ space per unit of volume becomes

$$\rho_k dk = \frac{2N_k dk}{L_x L_y L_z} \tag{2.29}$$

or

$$\rho_k = \frac{k^2}{\pi^2} \tag{2.30}$$

The density of states can also be expressed in terms of the energy of the carrier (electron or hole) beyond the band edge (i.e., above the conduction band or below the valence band edge). The energy and momentum in a band are related by

$$E = \frac{\hbar^2 k^2}{2m^*} = E' - E_c \qquad \text{for an electron}$$

or

$$E = \frac{\hbar^2 k^2}{2m^*} = E_v - E' \qquad \text{for a hole}$$

where E' is the total energy, and E is measured from the edge of a band.

Thus

$$k = (2m^* E / \hbar^2)^{1/2}$$

$$dk = \left(\frac{2m^*}{\hbar^2}\right)^{1/2} \frac{dE}{2E^{1/2}}$$

Substituting these relations into (2.29), we obtain the density of the states in either the conduction or valence band.

$$\rho_{c,v}(E) = \left(\frac{1}{2\pi^2}\right)\left(\frac{2m^*}{\hbar^2}\right)^{3/2} E^{1/2} dE \quad (\mathrm{m}^{-3}) \qquad (2.31)$$

Fig. 2.8 shows the density of states in a semiconductor with $m^*_{hh} = 0.46m_0$, $m^*_{lh} = 0.12m_0$ and $m^*_e = 0.079m_0$ corresponding to InP material.

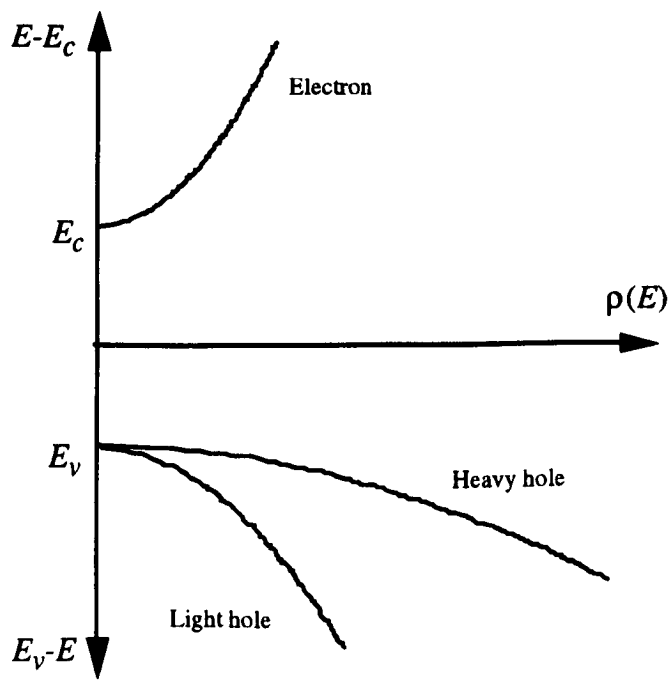

Fig. 2.8 Density of states in InP

2.6.2 Density of States for a Quantum Well Material

In a quantum well, the motion of carriers is confined in the direction perpendicular to the plane of well, hence the wave vector $\mathbf{k}_z$ is discrete, while, in the plane of well, the carriers are free to move. The energy of the electron is given as

$$E = E_n + \frac{\hbar^2}{2m_e^*}(k_x^2 + k_y^2) \tag{2.32}$$

where the wavevector $\mathbf{k} = (k_x, k_y, k_z)$ has a discrete z-component and continuous x and y components.

The component k_z can be found by first solving Schrödinger's equation to obtain the eigen energy levels and then using the following relation to obtain k_z

$$k_z = \frac{2m_e^*}{\hbar^2} E_n \qquad n=1,\ 2,\ 3... \tag{2.33}$$

For each sub-band, the density of states is

$$\rho(E) = \frac{m_e^*}{\pi\hbar^2 L_z} \tag{2.34}$$

i.e. for each sub-band the density of states is constant. Therefore the density of states in a single quantum well material can be described by a series of steps given by

$$g(E) = \sum_{n=1} \frac{m_e^*}{\pi\hbar^2 L_z} H[E - E_n] \tag{2.35}$$

where $H[E - E_n]$ is Heaviside function. Fig. 2.9 is a schematic representation of the density of states in a quantum well.

If we use a multiple quantum well (MQW) structure, instead of the single quantum well (SQW), the density of states is modified. When the barrier layers between wells are thick, each well is independent, and the density of the entire MQW structure is simply N times

the density of states for a SQW, where N is number of wells. However, if the barrier is thin or the barrier height is small, the energy levels in the adjacent wells are coupled, which splits each single well level into N different energy levels. In this case, the density of states is given by[13]

$$g(E) = \sum_{n=1}\sum_{k=1} \frac{m_e^*}{\pi\hbar^2 L_z} H[E - E_{nk}] \qquad (2.36)$$

where E_{nk} $(k=1,2,\ldots N)$ are the energy levels that split from the corresponding single well energy level E_n. The difference between the maximum and minimum values of E_{nk} indicates the broadening of each QW level due to coupling. For the step-like density of states to be preserved in a MQW structure, the broadening due to the coupling between the wells must be smaller than the broadening due to intraband relaxation [13].

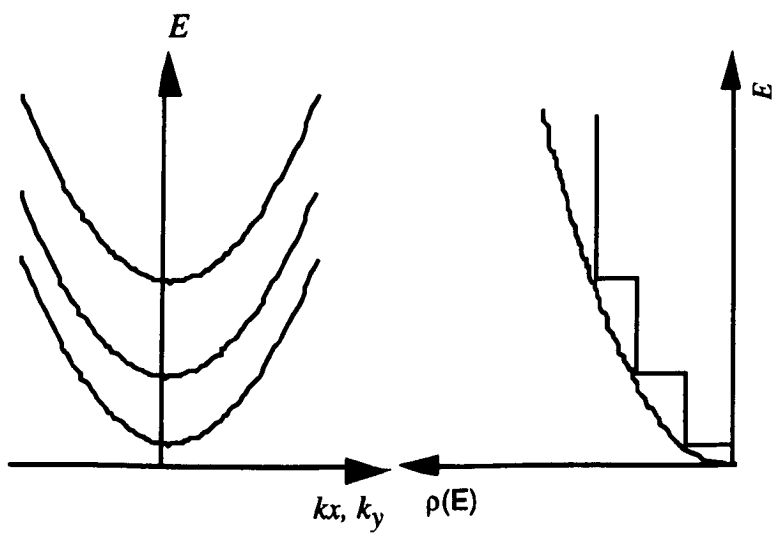

Fig. 2.9 Energy bands (left) and density of states (right) for a quantum well structure

2.7 Optical Absorption

2.7.1 Excitonic Effects in MQWs

Interband optical absorption always involves the creation of electron-hole pairs in which the electron and hole are attracted due to Coulombic forces. Since the electron and hole

interact, they cannot be regarded as single particle states and therefore the concept of the exciton must be introduced. An exciton is defined as an electron-hole pair which is bound together like a hydrogen atom but free to move through the lattice. In bulk semiconductors, peaks are observed in the absorption spectrum due to excitons but only at low temperatures since the weakly bound e-h pair is easily ionised by phonon interactions. The confinement of excitons in a QW modifies the spherically symmetric orbit by squashing it into the quantum well plane. The reduced average separation of the electron and hole increases the Coulombic force between them and leads to an increase in bonding energy. These increases mean that the thermal energy required to ionise them increases which, in turn, means that excitons can exist at room temperature in a MQW structure and thus they have an important effect on the absorption spectrum. There are excitonic states associated with each step in the optical absorption spectrum, with two peaks observed at each transition. The lower energy peak is associated with an exiton created from an electron and a heavy-hole, while the higher energy peak is associated with a light-hole exciton. In general, excitons are in the 1s hydrogenic ground state and lie at an energy just below the step in the density of states function.

The binding energy for an exciton in 3-dimensions is given by:

$$B_{3D} = -\frac{e^2 \mu_r}{2\varepsilon^2 h^2} \tag{2.37}$$

where

$$\mu_r = \frac{m_e^* + m_h^*}{m_e^* m_h^*} \tag{2.38}$$

is the reduced effective mass of the exciton, and ε is the dielectric constant of the material. Similar to the hydrogen atom, there is a series of energy levels for an exciton, with the energy for the n_{th} energy level being given by

$$E_n^{3D} = E_g + \frac{B_{3D}}{n^2} \quad n=1,2,... \tag{2.39}$$

where E_g is the bandgap energy of semiconductor.

In a purely 2-dimensional case. the binding energy is increased by a factor of 4 giving

$$B_{2D} = -\frac{2e^2\mu_r}{\varepsilon^2 h^2} \qquad (2.40)$$

In reality, both the finite width of the quantum well and penetration of the electron and hole wavefunctions into barriers result in a quasi 2D exciton with a binding energy lying somewhere between B_{2D} and B_{3D}. It is this increase in the binding energy that allows excitons to be observable at room temperature in MQW structures.

2.7.2 Polarisation Dependence of Absorption Spectra

The absorption spectrum of an MQW structure is polarisation dependent. It is found that for light with TE polarisation, which is polarised in the plane of the quantum well, there are two excitonic peaks. One is associated with the heavy-hole band |3/2,±3/2>, while the other is related to the light-hole band |3/2,±1/2>. The relative absorption strengths are 3:1 for heavy : light hole respectively. For light polarised perpendicular to the plane of the wells (TM), only one peak is observed, corresponding to light-hole excitation which gives relative absorption strengths of 0:1 for the heavy : light hole excitations.

2.8 Effects of an Electric Field on the properties of Quantum Wells

By applying an electric field, the properties of quantum well can be radically changed, giving effects which can be utilised in different optoelectronic components. The electric field can be applied either parallel to the plane of the wells or, more usefully, perpendicularly. Before analysing the effect an electric field has on an MQW structure, it is worth considering the effect on a bulk semiconductor.

2.8.1 The Franz-Keldysh Effect

When a large DC electric field ($\approx 10^5$ V/cm) is applied to a semiconductor, optical absorption can occur below the band edge, due to the fact that conduction and valence band wavefunctions have evanescent tails in the forbidden gap with some overlap. This effect is called the Franz-Keldysh Effect. The optical effects associated with the Franz-Keldysh mechanism in 3D are usually quite limited, however, because large electric fields lead to a smearing out of the absorption edge as the electron and hole wavefunctions have diminished spatial overlap with increased field.

2.8.2 Quantum Confined Stark Effect (QCSE)

The situation is quite different in quantum wells. As displayed in Fig. 2.10, a large energy shift occurs due to a major change in the potential well, with the energy shift ($E_a - E_b$) being proportional to the square of applied field. In addition, large electric fields can be applied, while retaining finite electron-hole overlap. This effect is the effect known as the Quantum Confined Stark Effect (QCSE) .

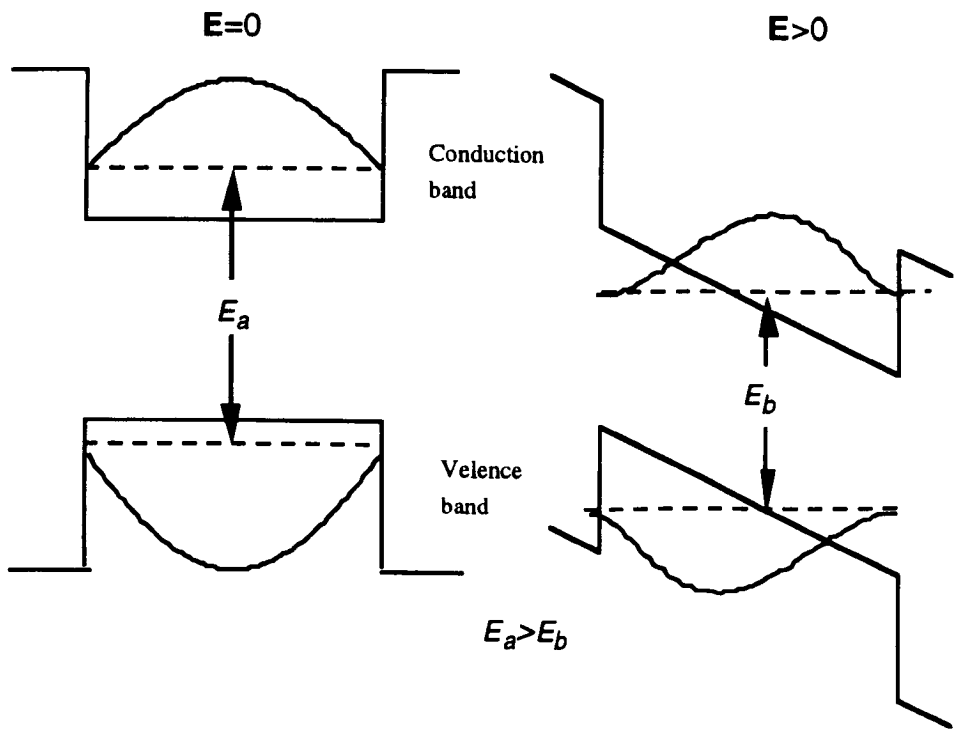

Fig. 2.10 Quantum confined Stark effect

The main features of the QCSE are that the exciton associated with the n=1 transition moves to lower energies[14] and that exciton resonance remains resolvable for electric field strengths of up to 50 times the classical exciton ionisation field[15].

2.9 Summary

In this chapter, the properties of InP and related compounds have been reviewed. The energy levels, density of states in one dimension confined quantum well, as well as optical absorption spectrum and the effects of an electric field on the properties of quantum well have been discussed.

References

1. J.C. Phillips, "Bonds and Bands in Semiconductors", New York: Academic Press, 1973

2. M.L. Cohen, and J.R. Chlikowsky, "Electronic Structure and Optical Properties of Semiconductors", Berlin: Springer-Verlag, 1988

3. G.L.Bir and G.E. Pikus, "Symmetry and Strain Induced Effects in Semiconductors", New York: John Wiley & Sons, 1974

4. H. Asai, and K. Oe, " Energy band-gap shift with elastic strain in $Ga_xIn_{1-x}P$ epitaxial layers on (001) GaAs substrates", J. Appl. Phys. **54**, pp. 2052-2056, 1983

5. C.P. Kuo, S.K. Vong, R.M. Cohen, and G.B. Stringfellow, "Effect of mismatch strain on band-gap in III-V semiconductors", J. Appl. Phys., **57**, pp. 5428-5432, 1985

6. A.T. Macrander and V.Swaminathan, "X-ray, photoluminescence, and SIMS characterization of InGaAs/InP grown by vapor-phase epitaxy", J. Electrochem. Soc., **134**, pp. 1274-1253, 1987

7. I.C. Bassignana_, C.J. Miner, N. Puetz, "Photoluminescence and double-crystal x-ray study of ingaas/inp -effect of mismatch strain on band-gap", J. Appli. Phys., **65**, pp.4299-4305, 1989

8. B. Broberg and S. Lindgren, "Refractive-index of $In_{1-x}Ga_xAs_yP_{1-y}$ layers and InP in the transparent wavelength region", J. Appl. Phys. **55**, pp. 3376-3381, 1984

9. S. Adachi, " Material parameters of $In_{1-x}Ga_xAs_yP_{1-y}$ and related binaries", J. Appl. Phys. **53**, pp. 8775-8792, 1982

10. E.O. Kane, Chapter 4A, in Handbook on Semiconductors, New York, pp. 2231, 1982

11. S. Adachi, "Physical Properties of III-V Semiconductor Compounds", pp. 92, John Wiley & Sons, New York, 1992

12. M.A. Afromowitz, "Refractive index of $Ga_{1-x}Al_xAs$", Solid state Commun. **15**, pp. 59, 1974

13. A. Katz ed., "Indium Phosphide and Related Materials: Processing, Technology, and Devices", Artech House, 1992

14. M. Whitehead, G. Parry, K. Woodbridge, P.J. Dobson, G. Duggan, "Experimental confirmation of a sum-rule for room-temperature electroabsorption in GaAs-AlGaAs multiple quantum well structures", Appl. Phys. Lett., **52**, pp. 345-347, 1988

15. D.A.B. Miller, D.S. Chemla, T.C. Damen, A.C. Gossard, W. Weigmann, T.H. Wood, C.A. Burrus, "Novel hybrid optically bistable switch - the quantum well self-electro-optic effect device", Appl. Phys. Lett., **45**, pp. 13-15, 1984

3. Quantum Well Intermixing Using Laser Process and Plasma Process

3.1 Introduction

In this chapter several techniques, namely, photo-absorption induced disordering (PAID), pulsed-PAID (P-PAID), a combination of PAID and P-PAID, as well as plasma process induced disordering, for quantum well intermixing of the InGaAs/InGaAsP material system are described. A simulation model to calculate the eigenenergies in an intermixed quantum well is also presented.

3.2 Photoluminescence Measurements

The photoluminescence (PL) measurement set-up is shown in Fig. 3.1. A Nd:YAG laser beam operating at 1.064 μm was coupled into a multimode fibre using a x10 microscope objective lens. By gluing the samples to the multimode fibre, the photoluminescence signal was collected by the fibre and coupled into a double spectrometer. PL, which can be measured at both room temperature and at 77K (by immersing the samples in liquid nitrogen), was automatically recorded using a computer.

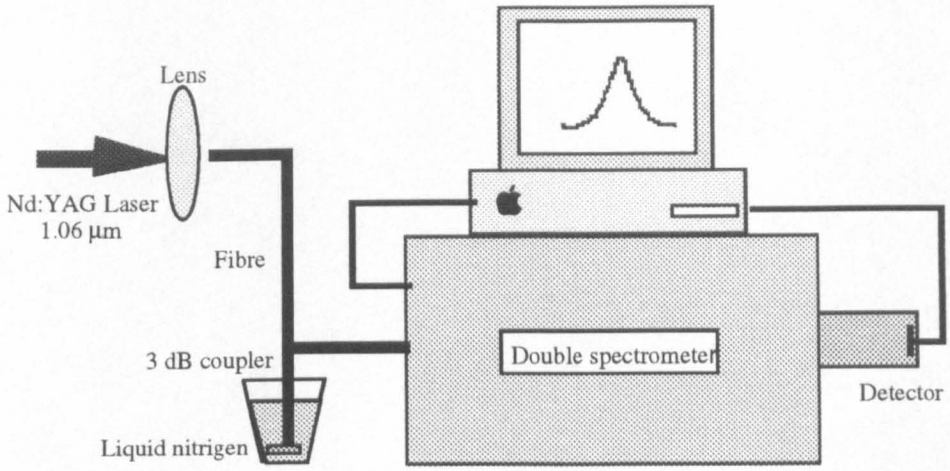

Fig. 3.1 PL measurement set-up

3.3 Photon Absorption Induced Disordering (PAID)

Several laser induced disordering techniques have been developed for the GaAs/AlGaAs system [1, 2]. These processes require high power densities to melt the material, but the quality of the recrystallised material may be poor [3], and if used in high energy pulsed mode can introduce thermal shock damage.

Photo-absorption induced disordering is an alternative laser disordering technique [4] which uses laser annealing and represents a promising process for the InGaAsP system. Essentially, PAID relies on band gap dependent absorption of incident laser irradiation within the active region of a multilayer structure. Heat is then generated by carrier cooling and non radiative recombination, causing interdiffusion of layers to take place. The resulting material is of high optical and electrical quality [5], [6]. However, the spatial resolution is limited by lateral heat flow to around several hundred μm [7].

This section briefly describes the principle of heat production due to absorption of light in the InGaAsP material system, and the processes involved in the technique .

3.3.1 Absorption of Light in a Semiconductor

The absorption of light by semiconductor material is substantially dependent on the bandgap diagram of the different epi-layers within the structure. This means that, for any appreciable absorption to take place, the bandgap diagram of the material must be less than the photon energy of the light. Fig. 3.2 shows the bandgap of different layers within a typical InGaAs(P) multiple quantum well laser structure. Also indicated is the photon energy of the incident laser irradiation from a Nd:YAG laser (λ=1.064 μm).

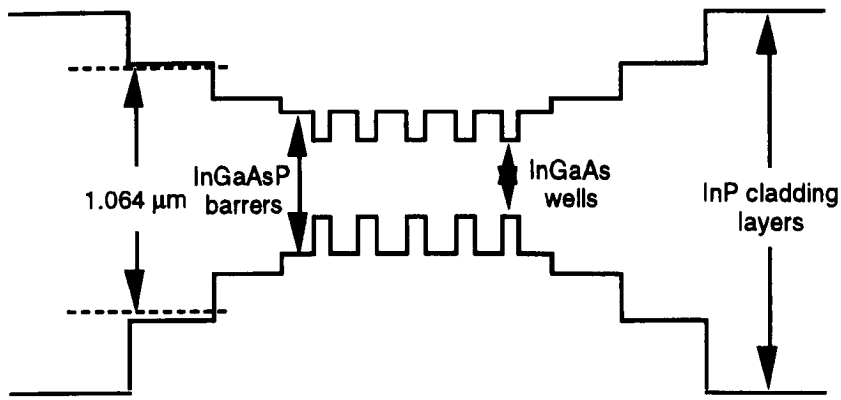

Fig. 3.2 Bandgap diagram of different layers within an InGaAs(P) MQW laser structure

From this diagram it is obvious that absorption should only take place within the active region of the epilayer, with the indium phosphide substrate and cladding layers being virtually transparent. Absorption in the active region will cause electrons to be promoted from the valence band to empty states in the conduction band.

3.3.2 Generation of Heat inside a Semiconductor

The electrons which are promoted to the conduction band by the laser irradiation will cool rapidly, giving up their energy to the crystal lattice through phonon emission[8]. Due to the large difference between electron and phonon energies, the energy exchange typically requires emission of several phonons and occurs on a time scale of the order of a few picoseconds.

After the electron has "cooled" and occupies a state at the bottom of the conduction band, it will recombine with a hole in the valence band and either emit a photon or not. The process in which an electron in the conduction band and a hole in the valence band recombine without emitting a photon is called nonradiative recombination. This can be due to imperfections in the material or different non-radiative processes such as Auger recombination. Since energy must be conserved, this recombination also contributes to heating the crystal lattice. Of course, the photons emitted by the e-h recombination may themselves be re-absorbed and contribute to lattice heating. This process is known as photon recycling and has been observed in InP [9]. Energy exchange between the electrons and the lattice causes the material to heat up.

3.3.3 Experiments

Fig. 3.3 shows the experimental set-up for Photon Absorption Induced Disordering (PAID). The laser used was a CW Nd:YAG laser operated at 1064 nm. The output power of the laser was adjusted by varying the current, which, in turn, changed the pumping power of the laser, as shown in Fig. 3.4. The laser beam was expanded using a lens, with a focal length of 20 mm, to avoid damaging samples by high intensity laser beam burning. In addition, the larger beam size is an advantage for uniform heating, and therefore intermixing, in large area samples.

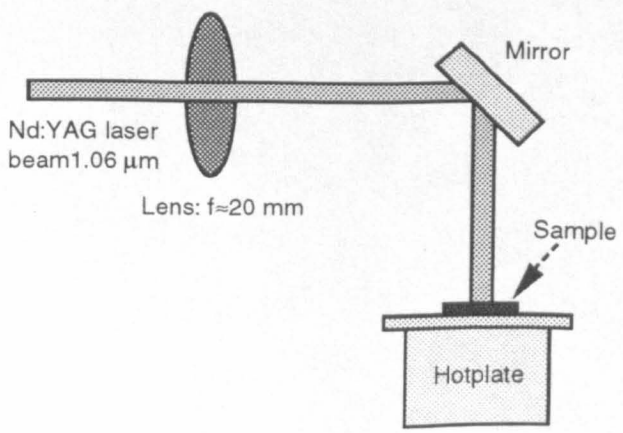

Fig. 3.3 Experimental set-up for PAID

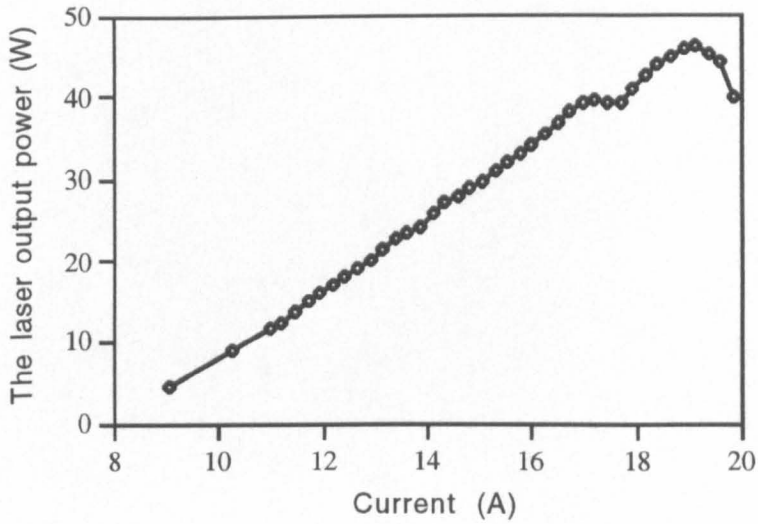

Fig. 3.4 The dependence of the output power of the laser on the pumping current

Samples were coated with a layer of 500 nm PECVD SiO_2, which acted both as an antireflection coating and as a protective layer against surface reactions with atmosphere during the subsequent high temperature process. During the PAID process, the samples were placed on a piece of polished ceramic and then raised to a background temperature of around 340°C, by using a hotplate. The increase in the background temperature reduced the incident laser power density required to heat the material up to the temperature at which intermixing would occur.

The samples were irradiated using the CW laser for, typically, 2-5 mins, depending on the power density of the laser. By comparing the blue shifts of the samples with those of samples annealed using RTA, the temperature of the samples was estimated to be around 620-680 °C . An attempt to measure the temperature of the sample was made using a thermocouple, however, the measured temperatures were much higher than that expected (up to 1000 °C), inaccuracy being due to the fact that the thermocouple was being heated directly by the laser irradiation while the measurements were carried out.

3.3.4 Results

The blue-shifts are dependent on laser power density and irradiation time. Fig. 3.5 shows this dependence for a given power density of about 2 W/mm^2. Fig. 3.6 shows a typical PL spectrum for an intermixed sample, the PL for an as-grown sample is also shown.

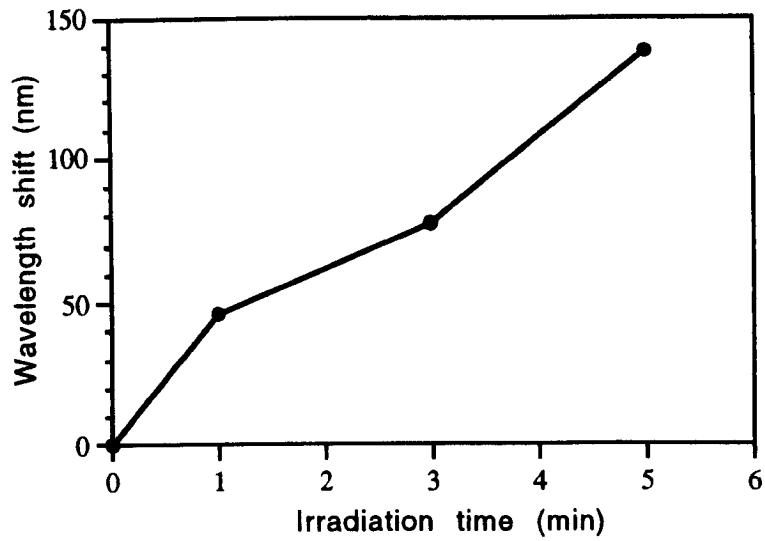

Fig. 3.5 Wavelength shift dependent on irradiation time of the laser (the laser power density is about 2 W/mm^2)

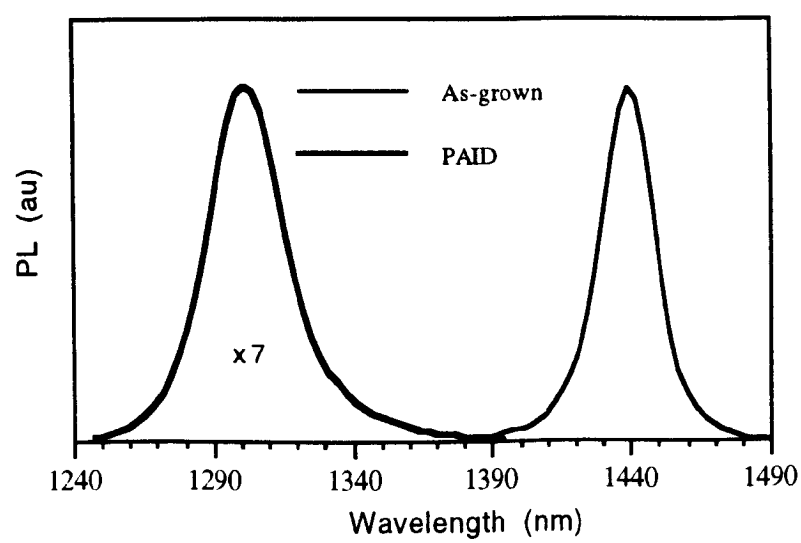

Fig. 3.6 77 K PL spectra for as-grown and PAID sample

As can be seen from Fig. 3.6-3.7, a blue-shift of 140 nm (91 meV) was obtained. The maximum blue-shift observed from this sample was 170 nm (115 meV). The PL spectra of intermixed samples exhibited a reduction in PL intensity by a factor of around 7, and a broadening of the PL peak. The FWHMs (full width at half maximum) were 23 meV and 14 meV for the intermixed sample and as-grown sample, respectively. However, it is believed that the degradation of the optical quality after intermixing, has little effect on passive devices fabricated using the intermixed material, although the active devices, e.g. lasers, may have lower efficiency and higher threshold current [5].

3.3.5 The Spatial Resolutions of PAID

To measure the spatial resolution of PAID process, a sample was coated with 500 nm of PECVD SiO_2, then patterned a layer of a NiCr-Au with thicknesses 10 nm and 200 nm respectively to form a control region. The samples were processed with different laser beam sizes, then the spatial resolution was measured using a set-up similar to that shown in Fig. 3.1, except that a micopositioner was used to move the samples. The ultimate resolution of the set-up, which is around 50 μm, is limited by the resolution of the multimode fiber used which has a diameter of 50 μm. 77 K PL was measured along a line perpendicular to the metal mask interface. Fig. 3.7 shows the measured 77 K PL shift across the sample. If the spatial resolution is defined as the transition region in which PL blue shift varies from 10%-90% of the maximum differential blue-shift, as is shown in Fig 3.7, the spatial resolution would be about 300 μm and 810 μm for laser beam sizes of 2 mm and 6 mm, respectively.

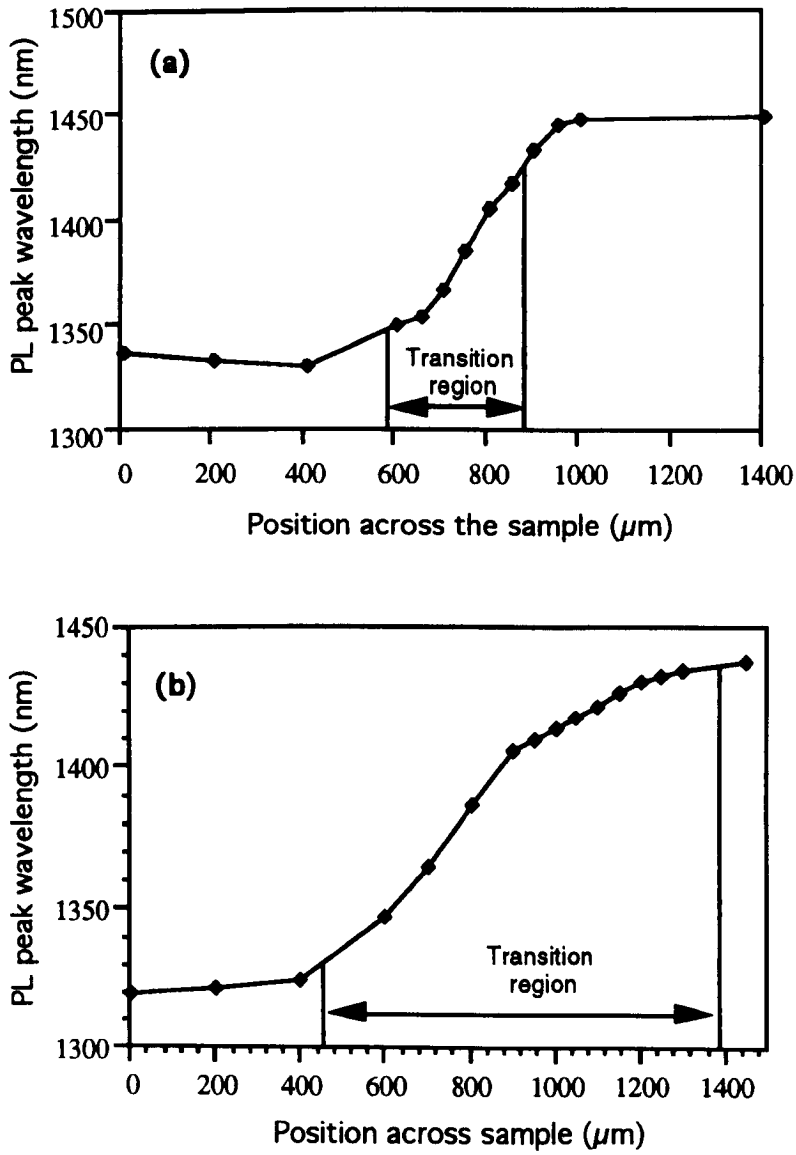

Fig. 3.7 Spatial resolution of PAID process. The laser beam size (FWHM) is about 2 mm (a) and 6 mm (b).

3.4 Pulsed Photon Absorption Induced Disordering (P-PAID)

The PAID technique is a reliable and reproducible process, however, due to heat diffusion, the spatial resolution is limited to several tens to several hundreds of μm. In contrast, the P-PAID process offers much better resolution, with experimental results indicating the resolution better than 20 μm [10, 11]. P-PAID process involves irradiating samples with high energy laser pulses from a Q-switched Nd:YAG laser to produce transient heating in

the crystal. Point defects are created by the associated rapid thermal expansion. These point defects subsequently diffuse during high temperature anneal, so enhancing the QWI rate.

3.4.1 The Thermal Stability of the Material

In the P-PAID process, the annealing conditions, i.e. annealing times and temperature, are very critical. For a given annealing time, the optimum annealing temperature should be such that the control sample has zero or minimal shift, while the intermixed sample has as large a shift as possible. Obviously, this temperature is the threshold temperature which is defined as the temperature at which thermal intermixing starts to occur. To find this temperature, the thermal stability of the material was measured.

The material structure (wafer No. MR743) used in the experiment is identical to that described in the chapter 6 (see section 6.8). It should be pointed out that the material was grown on a Sn-doped n^+ InP substrate which had an etch pit density (EPD) of around $5x10^4$ cm^{-2}, while normally used S-doped n^+ InP has an EPD of less than 500 cm^{-2}. Experiment [12] has shown that the QWs grown on Sn-doped substrate are more thermally stable than those grown on a S-doped substrate. It has also been found that the differential shift of the material after processing using P-PAID is very different for the InGaAs/InGaAsP grown on Sn- and S-doped substrates as shown in Fig. 3.8.

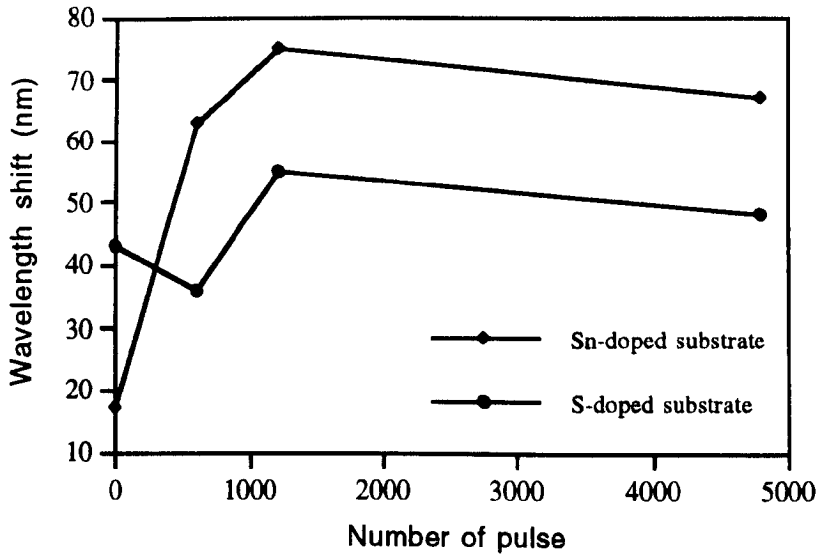

Fig. 3.8 Blue shifts for QW grown on Sn- and S-doped substrate. After [12]

A set of samples was annealed at different temperatures. Fig. 3.9 shows the thermal stability of the material. As can be seen, the threshold temperature is dependent on the RTA time. The thermal intermixing threshold temperatures are around 680 °C and 705°C for the RTA annealing times of 120 s and 60 s respectively.

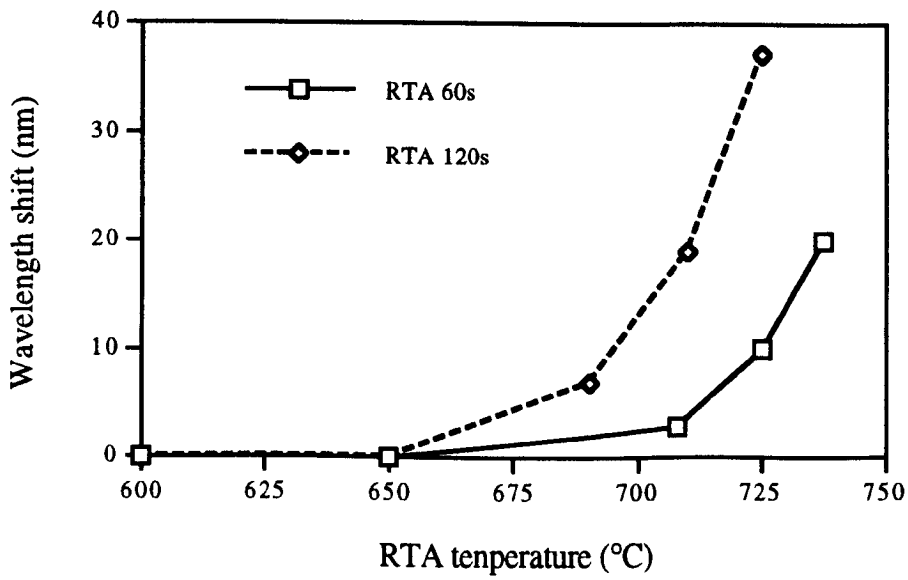

Fig. 3.9 Thermal stability of the material (MR743)

3.4.2 The P-PAID Experiment

The experimental set-up for the P-PAID process is shown in Fig. 3.10.

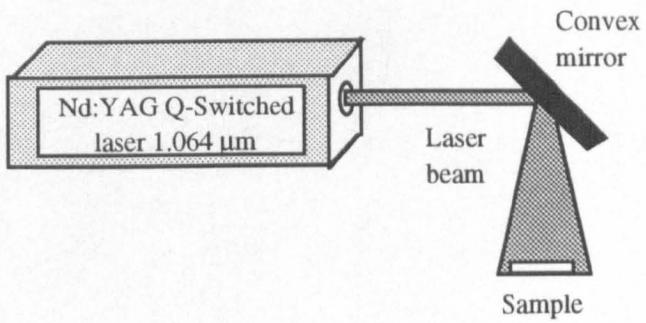

Fig. 3.10 P-PAID experimental set-up

The laser used was a Q-switched Nd:YAG laser, operating at a repetition frequency of 10 Hz and pulse length of ~ 7 ns at a wavelength of 1.064 μm. The laser beam was expanded using a convex mirror, and, by adjusting the distance between the sample and the mirror, the energy density of the laser pulse incident on the sample can be controlled to avoid possible damage to the sample by the high pulse energy density laser beam. The pulse energy density incident on the sample was calculated by measuring the power in the beam and using the following equation:

$$j = \frac{p}{Af} \tag{3.1}$$

where j is pulse energy density, p is the measured power, A is the area of the laser beam, and f is the repetition frequency.

Samples of area 2x2 mm^2, coated with 200 nm PECVD SiO_2, were irradiated at room temperature at normal incidence to the surface for times of 60 - 600 s with power energy densities of from 0.01 to 0.15 mJ/mm^2. The samples were subsequently thermally

annealed using the RTA, at temperatures from 700-725 °C for times of 60 - 180 s. PL was measured to check the bandgap shift of the samples.

3.4.3 Results and Discussions

Fig. 3.11 shows a typical PL spectrum of an intermixed sample measured at 77 K. Fig. 3.12 and 3.13 show the dependence of the bandgap blue-shift on irradiation conditions. As can be seen from Fig. 3.10, although the peak has blue shifted by 76 nm relative to the control, it has broadened from 16 to 39 meV (FWHM) and its peak intensity has dropped by a factor of 12. The control sample also shifted by around 20 nm relative to as-grown material. From Figures 3.11 and 3.12, it can be seen that the blue shift increases with the number and energy density of the laser pulses, however this increase tends to saturate after some point. This may be attributed to the formation of extended defects which are believed to trap mobile point defects, thereby decreasing the rate of intermixing [13].

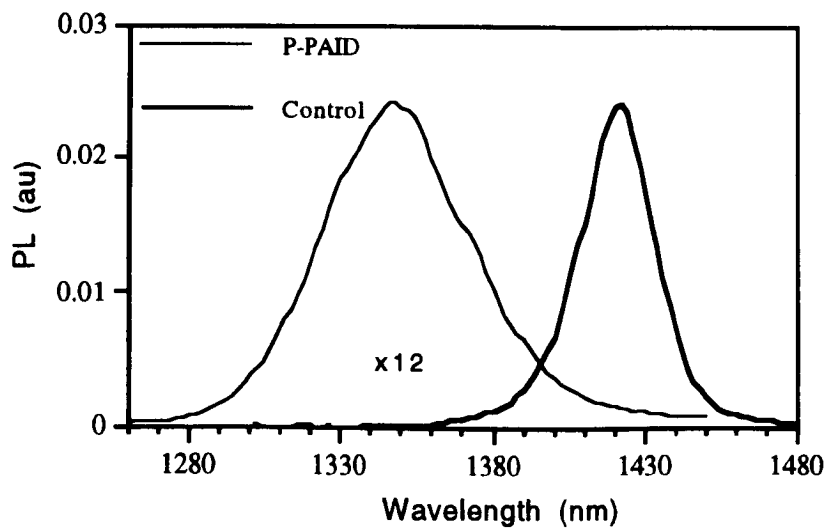

Fig. 3.11 77 K PL spectra for control sample and P-PAID sample which was irradiated for 3 mins. The pulse energy density was 0.2 mJ mm^{-2}, and both the control and the P-PAID samples were annealed for 120 s at 720 °C

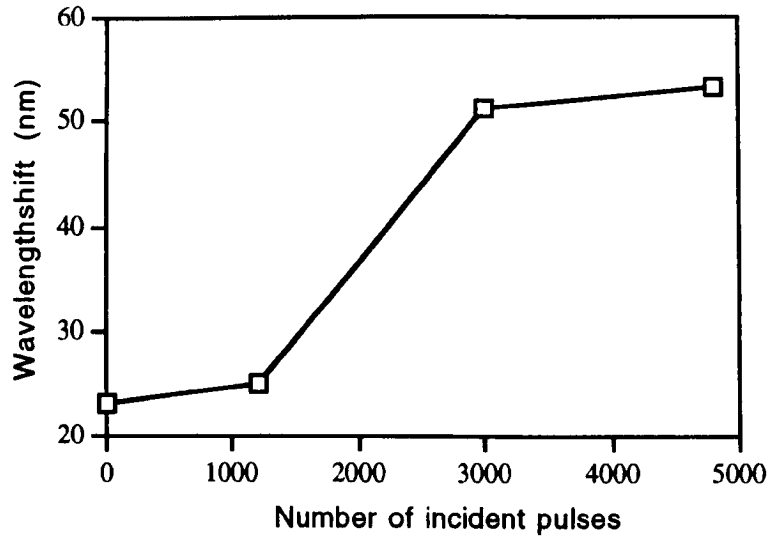

Fig. 3.12 Wavelength shift vs. the number of incident pulses. The pulse energy density was 0.08 mJ mm^{-2}, samples were annealed for 30 s at 750 °C.

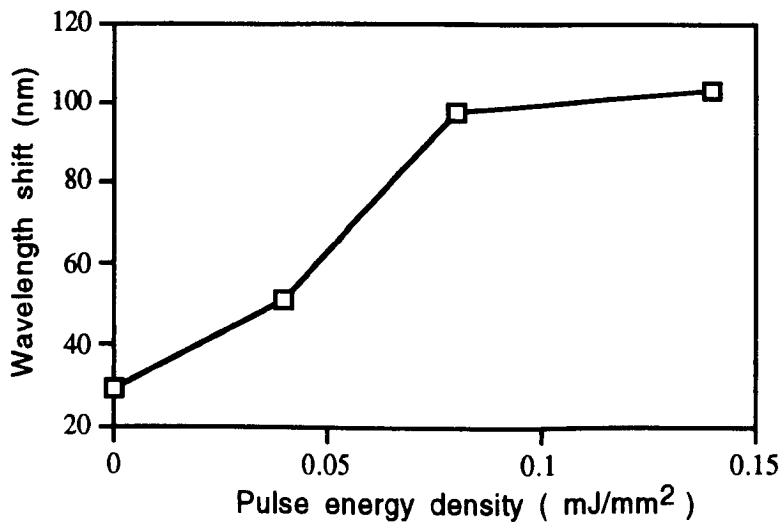

Fig. 3.13 Wavelength shift vs. pulse energy density. Samples were irradiated for 10 mins and annealed for 120 s at 720 °C

3.4.4 The Spatial Resolution of P-PAID

Due to the fact that the pulse width of the laser used is very short, around 7 ns, the generation of point defects is very localised, giving the technique a potentially high spatial resolution. Measurement of the spatial resolution was performed using room-temperature time-resolved photoluminescence (TRPL). Sample was prepared with a metal mask suspended a few hundred μm above the surface during irradiation. TRPL measurements were made using a 20-μm-diameter excitation spot, moving the sample by increments of 20 μm between measurements-the precision being limited by the mechanical precision of the translation stage used. The results which are shown in Fig. 3.14, indicate that the interface is clearly defined with a precision of better than 20 μm as the recombination time reduced from 35±5 ns in the masked region to <1 ns in the pulsed laser exposed region.

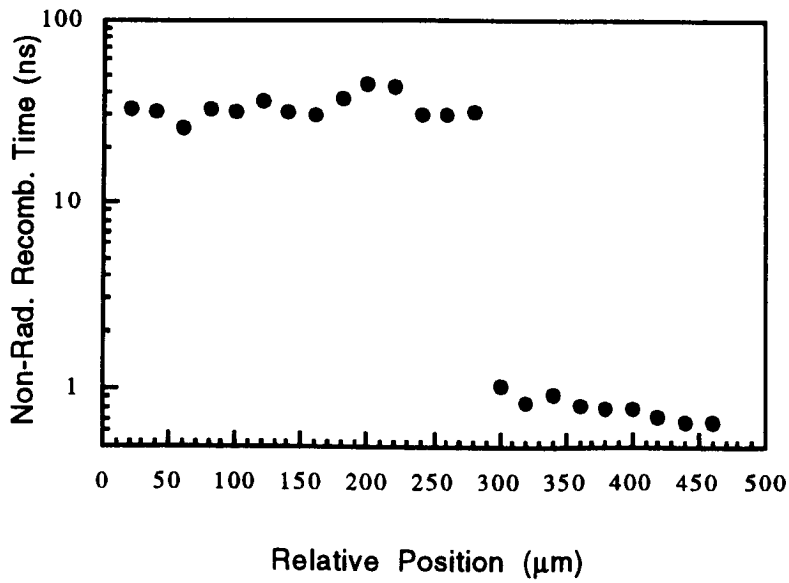

Fig. 3.14 Spatial resolution of P-PAID process, after [11].

3.5 Quantum Well Intermixing by Combining both Q-Switched and CW Lasers

3.5.1 Experiment

One of the potential problems encountered with P-PAID is the possible formation of extended defects. If a high density of point defects is created these may coalesce to form extended defects which are believed to trap mobile defects, thereby decreasing the rate of intermixing [13]. In order to overcome this problem, a combination of the PAID and P-PAID processes was used, in which a sample is irradiated by a pulsed laser, while simultaneously being annealed with a CW laser. In this case, it is believed that the thermal energy supplied by the CW laser should assist the rapid diffusion of point defects, thereby reducing the probability for extended point defect formation. This should enable larger bandgap shifts to be obtained and concurrently lead to an overall improvement in the quality of processed material.

Intermixing was carried out by simultaneously exposing the material to both a CW Nd:YAG laser with a power density of 2 W/mm^2 and a Q-switched Nd:YAG laser, with a pulse length of 7 ns, and a repetition frequency of 10 Hz, as is shown in Fig. 3.15.

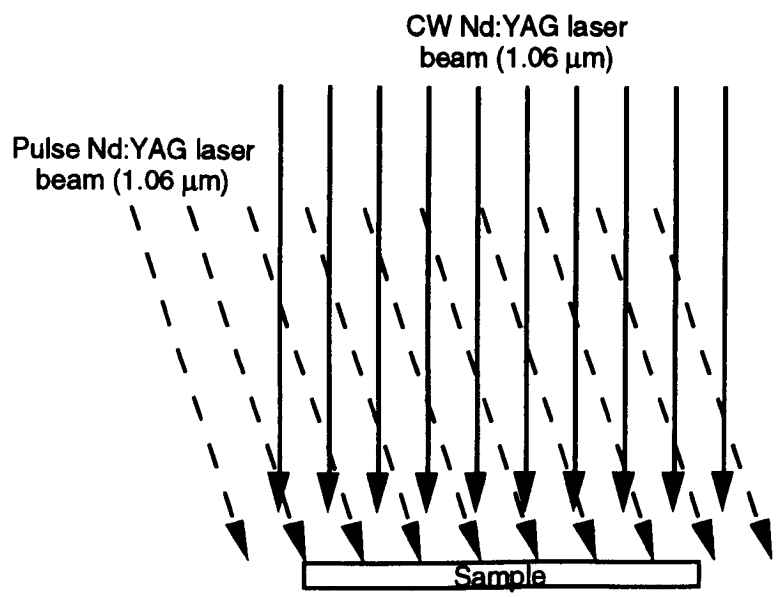

Fig. 3.15 A schematic representation of P-PAID+PAID process

3.5.2 Results

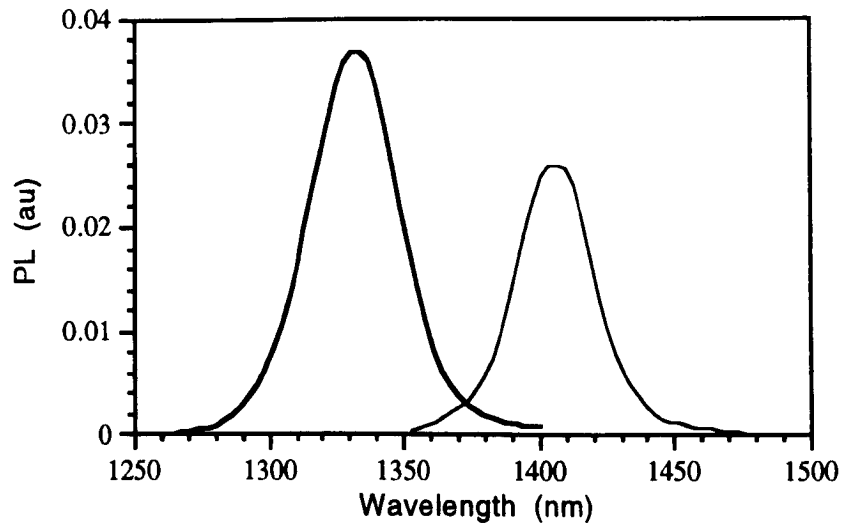

Fig. 3.16 77 K PL spectra for sample irradiated by the CW laser (thin line) and sample irradiated by both the CW and pulsed Laser (thick line)

Fig. 3.16 shows a 77K PL spectrum obtained for a sample exposed to both the CW and pulsed laser. Also shown is the spectrum of a control sample exposed to the CW laser only. This undergoes a blue shift of 30 nm compared to the as-grown material, however the shift of the material simultaneously exposed to the pulsed beam is significantly larger, leading to an overall differential shift of 70 nm. Compared to the P-PAID process, it is noticeable that the PL spectrum remains of high quality after QWI, with the PL intensity apparently increasing after processing (though this may be due to atmospheric absorption in the 1.4 to 1.5 μm spectral region), and the PL peak remaining narrow, with a width of 26 meV FWHM compared to 20 meV for the control (CW exposed only).

3.6 Plasma Processing

Intermixing by plasma processing [14] involves the deposition of a sputtered SiO_2 film and subsequent annealing, either using CW laser or using RTA. During the deposition. Point defects are created close to the semiconductor surface due to exposure of the sample

to the plasma which, during the annealing stage, diffuse into the active region, leading to a significant enhancement in the intermixing rate.

3.6.1 Experiments

Samples were patterned so that only areas to be intermixed were exposed to the sputtering plasma. First a sample coated with PECVD SiO_2 of 200 nm was patterned using photolithography and the SiO_2 was etched in buffered HF. The photoresist and SiO_2 over the regions not to be disordered were left on the sample after HF-etching so as to protect to the surface of the sample during the subsequent sputtering process. 200 nm of sputtered SiO_2 was deposited in a Nordiko sputtering machine, using an $Ar:O_2$ gas mixture and RF power of 100 W, DC bias of 1 kV and a gas pressure of $5x10^{-3}$ mbar. The sample was then cleaned in acetone to remove the photoresist, and annealed using either an RTA for times from 120 s to 210 s at a temperature of 625 °C, or a CW Nd:YAG laser emitting at 1.064 μm for 3-5 minutes with a power density of 1.5 W/mm^2, which is significantly lower than that required for the PAID process.

3.6.2 Results and Discussions

Fig. 3.17 shows the dependence of the peak wavelength of the spectra for the plasma exposed samples (sputtered SiO_2 coated), on the RTA time. Fig. 3.18 shows the PL spectra of the control regions, plasma exposed regions before and after annealing using the CW laser, measured at 77 K, and of as-grown material. Fig. 3.19 shows 77 K PL spectra for the plasma processed sample, alone with the control sample which was annealed using RTA annealing at 625 °C for 210 s.

As can be seen from Fig. 3.17, the plasma exposed samples have an increasing blue-shift, with a maximum blue-shift of around 110 nm, while the peak wavelength of the spectra for samples coated with PECVD SiO_2 (which had not exposed to plasma) remain

unchanged for RTA times from 150 s to 210 s. This is due to the fact that the samples with sputtered SiO_2 caps start to exhibit initial bandgap shift at a temperature of ~550 °C [14], which is significantly lower than required for thermally induced intermixing, being about 650 °C for the InGaAsP material system for the annealing times used here. Therefore the energy blue-shift in the control region is almost completely suppressed, while blue-shift of up to 110 nm in the disordered regions can be obtained. Also, it is noticeable that there has a small blue-shift (~10 nm) for plasma exposed samples even before annealing. Comparing Fig. 3.18 with Fig. 3.19, we can conclude that both annealing techniques have similar effects in terms of amount of intermixing and, PL quality.

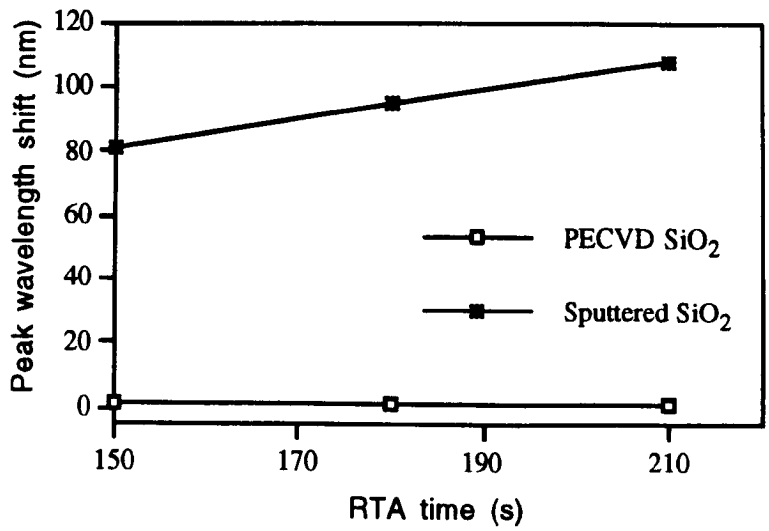

Fig. 3.17 Wavelength shift dependent on RTA time for the sample exposed to plasma (sputtered SiO_2) and control sample (PECVD SiO_2). Annealing temperature is 625 °C.

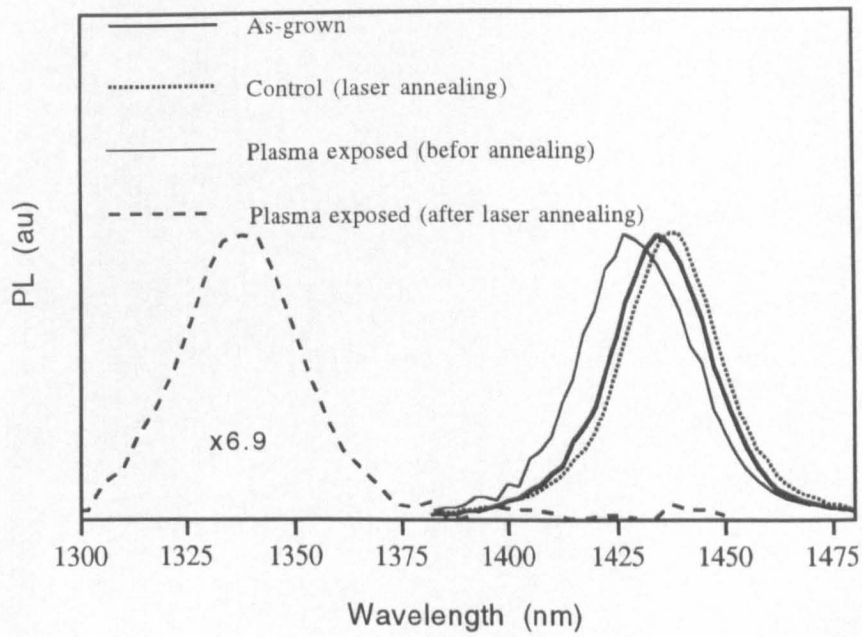

Fig. 3.18 77 K PL spectra for as-grown, control, plasma exposed samples before and after laser annealing

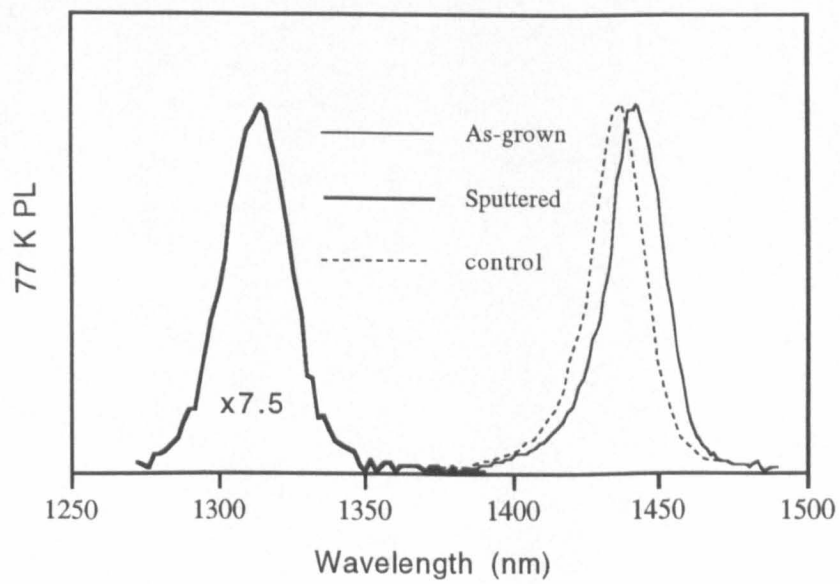

Fig 3.19 77 K PL spectra for as-grown, control and plasma exposed samples, annealed at 625 °C for 210 s in RTA.

3.6.3 Spatial Selectivity of the Plasma Process

Fig. 3.20 shows the variation of 77 K PL peak wavelength across a patterned sample, half of which was coated with sputtered SiO_2. The sample was annealed using the CW laser. As can be seen, the transition region is around 50 μm. However, due to the fact that the resolution of the experimental set-up is around 50 μm, limited by the multimode fibre used which has a diameter of 50 μm, the resolution of the plasma process could be much better than this value.

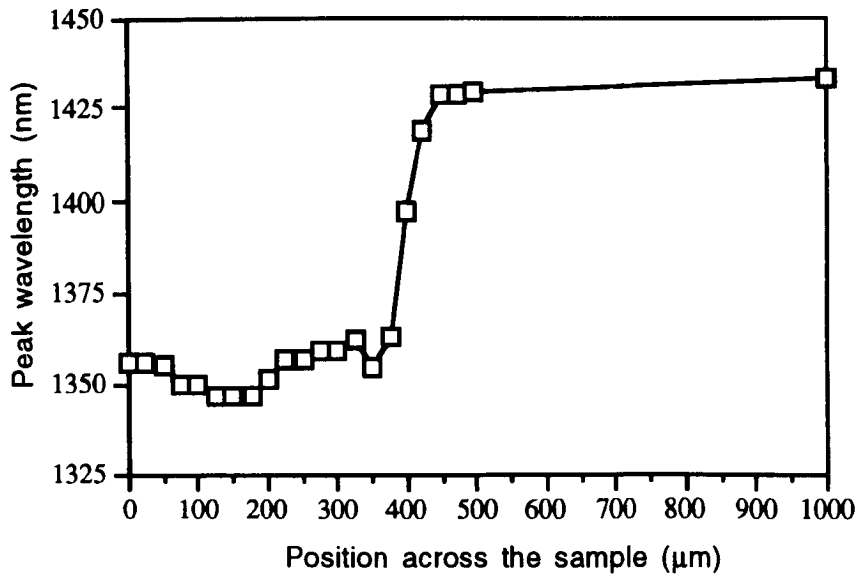

Fig. 3.20 Spatial selectivity of plasma process (laser annealing)

3.7 Simulation of Quantum Well Intermixing

3.7.1 Calculation of Profile of Intermixed Quantum Well

During the process of quantum well intermixing, the exchange of group V species, i.e. P and As, and group III species i.e. Ga and In, between wells and barriers causes the intermixing of wells. The calculation of the profile of intermixed quantum wells can be based on Fick's law [15] of interdiffusion.

3.7.1.1 Fick's Law

Diffusion is the process by which matter is transported from one part of a system to another as a result of random molecular motions. The mathematical theory of diffusion is based on the hypothesis that the rate of transfer of diffusion of a substance through a unit area of a section is proportional to the concentration gradient measured normal to the section, i.e.

$$F=-D\frac{\partial C(z,t)}{\partial z} \tag{3.2}$$

where F is the rate of diffusion per unit area of section, in units of $m^{-2}s^{-1}$,

D is the diffusion coefficient in units of m^2s^{-1},

$C(z,t)$ is the matter concentration in unit of m^{-3}.

The negative sign in Eq. (3.2) arises because diffusion occurs in the opposite direction to that of increasing concentration.

3.7.1.2 Differential Equation of Diffusion

By considering diffusion through an element of volume in the form of cylinder with unit cross section area, the diffusion equation can be written as:

$$\frac{\partial C}{\partial t}=D\frac{\partial^2 C}{\partial z^2} \tag{3.3}$$

In the one dimensional case, a solution to the Eq. (3.3) is

$$C(z,t)=\frac{A}{\sqrt{t}}\exp(-\frac{z^2}{4Dt}) \tag{3.4}$$

where A is a constant. Eq.(3.4) represents the diffusion from an infinite concentration at z=0 and t=0, with diffusion profile being symmetric about z. The total diffusion per unit area is given by

$$M=\int_{-\infty}^{+\infty}C(z,t)dz=2A\sqrt{\pi D} \tag{3.5}$$

Substituting Eq. (3.5) into Eq. (3.4), then gives

$$C(z,t)=\frac{M}{2\sqrt{\pi Dt}}\exp(-\frac{z^2}{4Dt}) \tag{3.6}$$

3.7.1.3 Extended Initial Distribution

So far we have considered only cases in which all of the diffusing species substance is concentrated initially in a plane. More frequently, in practice, such as a quantum well source, the initial distribution has a finite width. The solution for such an initial distribution can be obtained by integrating Eq. (3.6)

$$C(z,t)=\int_{z}^{+\infty}\frac{C_0}{2\sqrt{\pi Dt}}\exp(-\frac{\xi^2}{4Dt})d\xi \tag{3.7}$$

The resultant integration can be expressed in terms of the complementary error function $erfc(x)$:

$$C(z,t)=\frac{C_0}{2}erfc(\frac{z}{2\sqrt{Dt}}) \tag{3.8}$$

where

$$erfc(z)=1-\frac{2}{\sqrt{\pi}}\int_{0}^{z}\exp(-\xi^2)d\xi \tag{3.9}$$

3.7.1.4 Modelling of Quantum Well Interdiffusion

Measurement of the X-ray rocking curve of a InGaAs/InGaAsP MQW material structure lattice matched to InP shows that no strain occurs after intermixing, hence it can be assumed that the material remains lattice matched to InP during the intermixing process. Under this assumption, we can use the concentration of P in the well and the barrier as an indication of the degree of intermixing.

At the initial time, t=0, the barrier concentration is C_1, the well concentration is C_2. The solution in the QW case is the sum of the solutions of the left and right barrier diffusion. For the left diffusion, we have

$$C_L = \frac{1}{2}(C_1 - C_2)erf(\frac{z + w/2}{2\sqrt{Dt}}) \tag{3.10}$$

For the right diffusion, we have

$$C_R = (C_1 - C_2)[1 - \frac{1}{2}erf(\frac{z - w/2}{2\sqrt{Dt}})] \tag{3.11}$$

where w is the width of the well. Combining the two equations above, the diffusion solution for a quantum well is

$$C(x,t) = (C_1 - C_2)[1 - \frac{1}{2}erf(\frac{z - w/2}{2\sqrt{Dt}}) + \frac{1}{2}erf(\frac{z + w/2}{2\sqrt{Dt}})] \tag{3.12}$$

Fig. 3.20 shows the calculated profile with a parameter of diffusion length $L_D = \sqrt{Dt}$. for an InGaAs/InGaAsP well with well width of 80 Å. As can be seen, the concentration at the well-barrier interfaces is always equal to the average value of the concentrations in the well and barriers for a diffused well, regardless of the diffusion length. For the well shown in Fig. 3.20, with the diffusion length is in the range of 0-20 Å, the profile of the well in the bottom of the well narrows with increase of the diffusion length. This change in

the well profile would have the effect of raising confined electron and hole energy levels, while the bulk bandgap energy, which is associated with the concentration at the bottom of the well is little changed. When the diffusion length is larger than 20 Å, a change of the concentration at the bottom of the well starts to occur, and the electrons in the conduction band and holes in the valence band will see less spatial confinement than before.

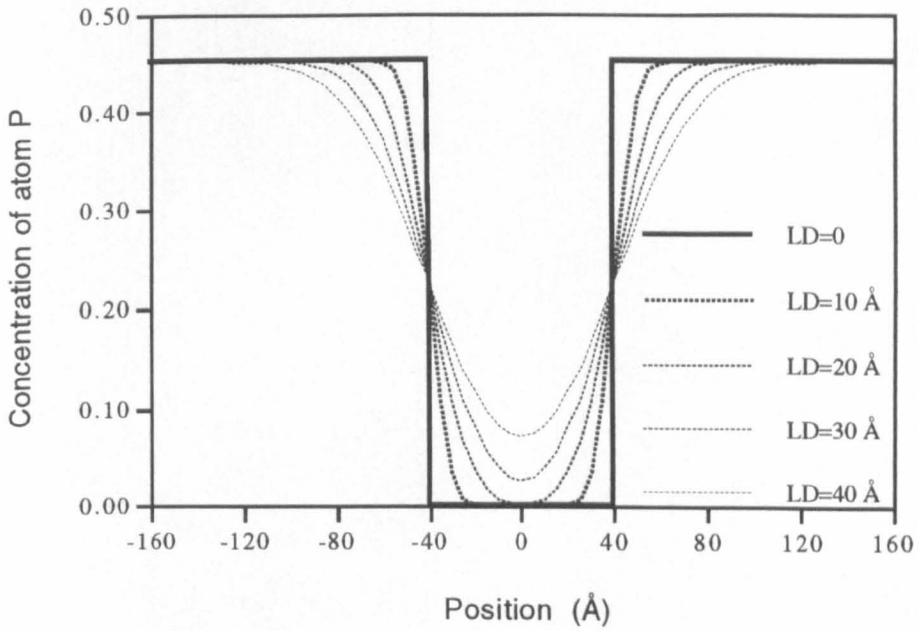

Fig. 3.20 Profile of the concentration of atomic P in a InGaAs/InGaAsP quantum well

3.7.2 Calculation of Energy levels in an Intermixed Quantum Well

3.7.2.1 The Schrödinger Equation in an Arbitrary Quantum Well

The 1-D Schrödinger equation in an arbitrary quantum well potential profile (see Fig. 3.21) can be written as[13]:

$$-\frac{\hbar^2}{2}\frac{d}{dz}\left(\frac{1}{m^*(z)}\frac{du(z)}{dz}\right)+V(z)u(z)=Eu(z) \qquad (3.13)$$

where $m^*(z)$ is the effective mass of electrons in the wells and is assumed to be independent of energy, $u(z)$ is the envelope wave function of Schrödinger Equation, $V(z)$ is potential profile of the well, E is the eigenenergy. Bounded light hole and heavy hole energies and envelope functions are determined from Eq. (3.13), using the valence band potential profile and appropriate light hole and heavy hole effective masses. At any point z, $u(z)$ should meet the following conditions:

$$u(z^-) = u(z^+) \tag{3.14}$$

$$\frac{1}{m^*(z^-)} u'(z^-) = \frac{1}{m^*(z^+)} u'(z^+) \tag{3.15}$$

The envelope wave function exponentially decays to 0 in both the left and the right barriers, so the envelope wave function can be written in the form

$$u(z) = \begin{cases} u_{bL}(z) = \dfrac{A}{\alpha} e^{\alpha z} & z \le 0 \\ u_w(z) & 0 \le z \le W \\ u_{bR}(z) = \dfrac{B}{\beta} e^{-\beta(z-W)} & z \ge W \end{cases} \tag{3.16}$$

where

$$\alpha = \sqrt{\frac{2m^*_{BL}(V_{BL} - E)}{\hbar^2}} \tag{3.17}$$

and

$$\beta = \sqrt{\frac{2m^*_{BR}(V_{BR} - E)}{\hbar^2}} \tag{3.18}$$

and $u_w(z)$ is the envelope function in the well regions $0 \le z \le W$, which we wish to evaluate by solving Schrödinger's equation.

where V_{BL} and V_{BR} are barrier heights at the left and right of the well-barrier interfaces, respectively, as shown in Fig. 3.21, while m^*_{BL} and m^*_{BR} are the effective masses of the electron at the left and right barriers.

3.7.2.2 Shooting Method

The Schrödinger's equation in arbitrary potential profile of quantum well cannot be solved analytically. Many numeric methods have been developed to solve the problem[16-19]. Here, we describe the shooting method, which is simple but very accurate. The method can be described as follows:

1. Assume an energy level E_0 in Schrödinger's equation;
2. calculate the envelope wave function using the boundary conditions at the left boundary as the initial conditions;
3. The envelope wave function can be evaluated using a Taylor series expansion;
4. Check if the envelope wave function satisfies the boundary conditions at the right side of the well, if it does, this means the assumed E_0 is one of eigenenergies, if not, modify the E_0 and start the process again .

A new variable, Z , which is defined as:

$$Z=az \tag{3.19}$$

is introduced, where

$$a=\frac{\sqrt{2m_0E_0}}{\hbar}z_0=0.5117\ \text{Å}^{-1} \tag{3.20}$$

where m_0 is the mass of free electron, E_0=1 eV, e is electron charge, and z_0=1 Å. Through this variable substitution, the Schrödinger's equation Eq. (3.13) can be transformed to a dimensionless equation:

$$\frac{d}{dZ}\left(\frac{m_0}{m^*(Z)}\frac{du(Z)}{dZ}\right)=f(Z)u(Z) \tag{3.21}$$

where

$$f(Z)=V(Z)-E \tag{3.22}$$

Defining

$$t(Z) = \frac{m_0}{m^*(Z)} \frac{d}{dZ} u(Z) \tag{3.23}$$

the second order differential equation is converted into a system of two first order equations:

$$\frac{d}{dZ} u(Z) = \frac{m^*(Z)}{m_0} t(Z) \tag{3.24}$$

$$\frac{d}{dZ} t(Z) = f(Z) u(Z) \tag{3.25}$$

To solve the equations numerically, the well is divided into n segments as is shown in Fig. 3.21.

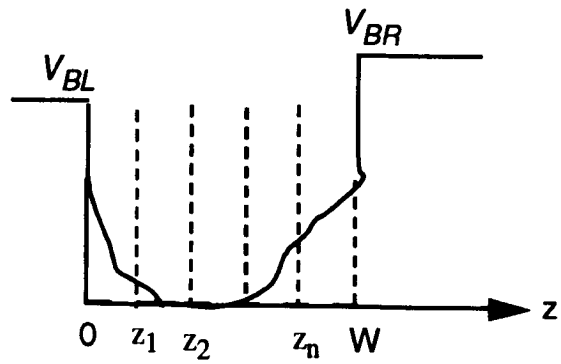

Fig. 3.21 An illustration of arbitrary potential well and discretisation method

Equations (3.25) and (3.26) can be computed using a Taylor series expansion which are, neglecting third order and higher terms

$$u(Z_0 + \Delta Z) = u(Z_0) + \frac{du}{dZ}|_{Z_0} . \Delta Z + \frac{1}{2} \frac{d^2u}{dZ^2}|_{Z_0} . \Delta Z^2 \tag{3.26}$$

$$t(Z_0 + \Delta Z) = t(Z_0) + \frac{dt}{dZ}|_{Z_0} . \Delta Z \tag{3.27}$$

Substituting Eq. (3.24) and (3.25) into Eq. (3.26) and (3.27), and writing them in the form of iteration, gives:

$$u(n+1) = u(n) + \frac{m^*(n)}{m_0} t(n).h + \frac{1}{2}\frac{m^*(n)}{m_0} u(n) f(n) h^2 \qquad (3.28)$$

$$t(n+1) = t(n) + u(n) f(n) h \qquad (6.29)$$

where h is iteration step.

Before starting the iteration, the starting values, i.e., the initial conditions $u(0)$ and $t(0)$ should be determined. The conditions, found by considering equations (3.14), (3.15) and (3.16), are:

$$u(0) = \frac{A}{\alpha} \qquad (3.30a)$$

$$t(0) = \frac{m_0}{m^*(0)} A \qquad (3.30b)$$

where $m^*(0)$ is the effective mass of carriers at left boundary, and A is arbitrary constant. For an assumed value of E, the corresponding envelope wave functions in the region [0, W] can be integrated using equations. However, the envelop wave function calculated above generally do not satisfy the boundary conditions at the right boundary of the well, which means a new trial value of E should be used until the following boundary condition is satisfied (see Fig. 3.22):

$$t(0) = \frac{m_0}{m^*(W)} A \qquad (3.31)$$

where, $m^*(W)$ is the effective mass of carriers at right boundary.

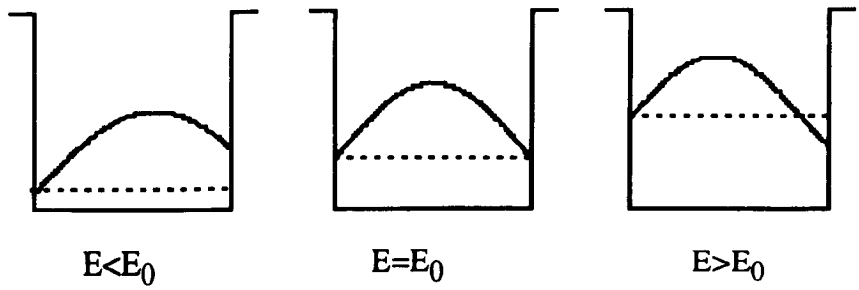

Fig. 3.22 Calculated envelope function under different assumed energy level E for a symmetric quantum well. E_0 is the true eigenenergy level.

3.7.3 Calculated Results

Fig. 3.23 plots the changes of carrier energy level in intermixed quantum wells. Fig. 3.24 shows the change of bulk bandgap energy with diffusion length, and Fig. 3.25 shows the dependence of peak wavelength of room temperature PL on diffusion length.

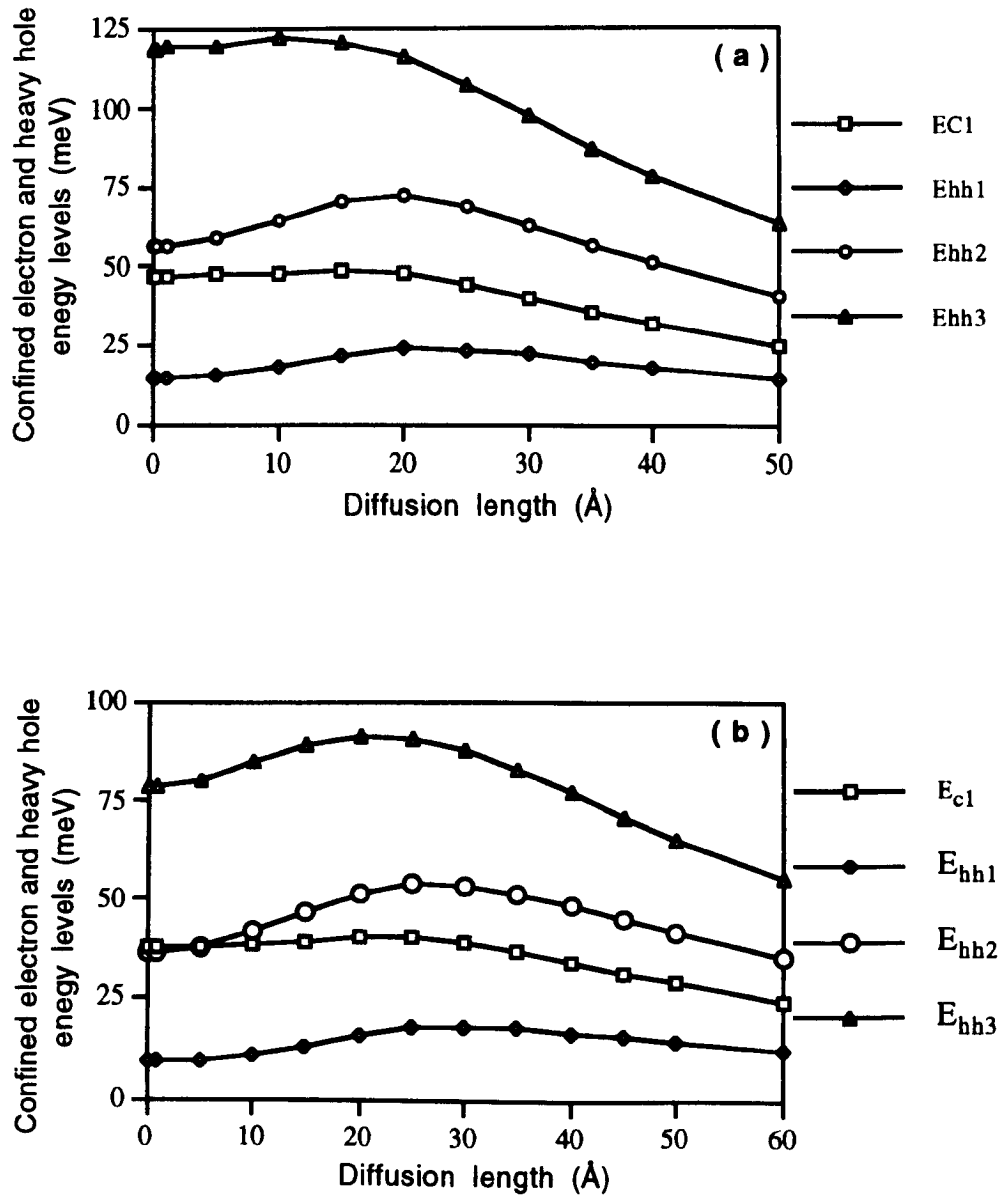

Fig. 3.23 Energy levels for electrons (E_{c1}) and heavy holes (E_{hh1}, E_{hh2}, E_{hh3}) in a diffused InGaAs/InGaAsP quantum well for the Well width of 60 Å (a) and 80 Å (b).

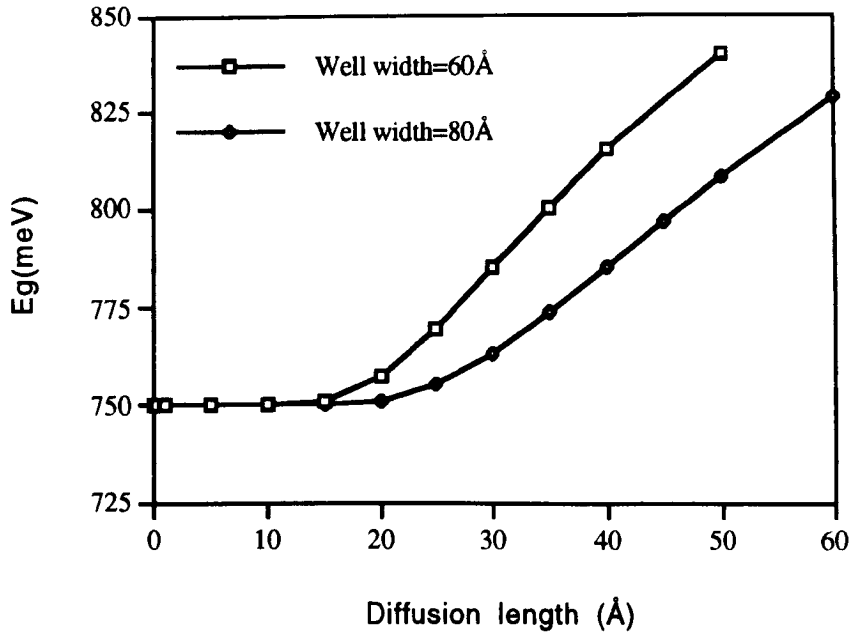

Fig. 3.24 Change of Bulk bandgap energy with respect to the diffusion length.

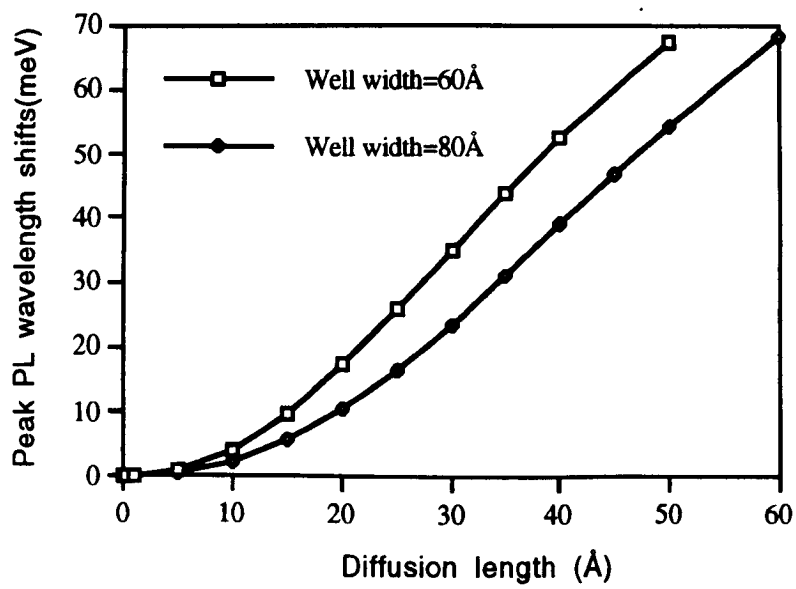

Fig. 3.25 Peak wavelength shift as function of diffusion length

From the figures, it can be concluded the blue-shift of PL peak wavelength which is found from

$$E_0 = E_g + E_{c1} + E_{hh1} \tag{3.32}$$

is primarily due to the change of the bulk bandgap energy at the centre of an interfused well, while the change of both electron and hole energy levels in an intermixed quantum well change relatively much less than the change of bulk bandgap energy. The energy levels have an insignificant blue-shift with increasing diffusion length, but after some point, they reach maximum values and then decrease to produce a red-shift. Also we can see that a narrow well has a larger blue-shift compared to a wider well for a given diffusion length. Using this property, the size spreading in a quantum dot array can be considerably reduced by post-growth intermixing, and the width of photoluminescence of material is reduced accordingly [20].

3.8 Summary

In this chapter, quantum well intermixing in InGaAs/InGaAsP material system has been demonstrated using laser processes and a plasma process. PAID is a reliable and reproducible process, and blue-shifts of up to 140 nm can be obtained, however, unfortunately the spatial selectivity is limited to around several hundreds of μm. In contrast, the P-PAID process offers much better spatial resolution, being better than 20 μm, however the intermixed material suffers from poor optical quality as is indicated by the reduced PL intensity and broader PL linewidth. In addition this process is less reproducible and more sensitive to the quality of the substrate of wafers. An alternative approach is to use a combination of P-PAID and PAID. This process offers a similar yield to that of PAID, and further work needs to be carried out in order to take advantage of the high spatial selectivity of the P-PAID process. The plasma process has proven to be highly successful, in the sense of larger differential blue-shifts (up to 120 nm), almost complete suppression of bandgap shifts in control regions, as well as potentially high spatial resolution. Modelling of the intermixing of quantum wells was also performed and the results indicate that the changes of the bulk bandgap energy in the well is the principal reason for the blue-shift of the PL.

References

1. A. Rys. Y. Shieh, A Compaan, H. Yao, A. Bhat, "Pulsed laser annealing of GaAs implanted with Se and Si", Optical. Eng., **29**, pp. 329-338, 1990

2. J. Ralston, A.L. Moretti, R.K. Jain, F.A. Chambers, "Intermixing of $Al_xGa_{1-x}As$/GaAs superlattices by pulsed laser irradiation", Appl. Phys. Lett., **50**, pp. 1817-1819, 1987

3. J.E. Epler, F.A. Ponce, F.K.J. Endicott, and T.L. Paoli, "Layer disordering of GaAs/AlGaAs superlattices by diffusion of laser incorporated Si", J. Appl. Phys. 64, pp. 3439-3444,1988

4. C.J. Mclean, J.H. Marsh, R.M. De La Rue, A.C. Bryce, B. Garrett, R.W. Glew, "Layer selective disordering by photoabsorption-induced thermal-diffusion in InGaAs/InP based multiquantum well structures" Electron. Lett., **28**, pp. 1117-1119, 1992

5 A. McKee, C. J. McLean, A. C. Bryce, R. M. De La Rue, and J. H. Marsh, "High-quality wavelength tuned multiquantum-well GaInAs/GaInAsP lasers fabricated using photoabsorption induced disordering", Appl. Phys. Lett. **28**, pp. 2263-2265, 1994

6 G. Lullo, A. McKee, C. J. McLean, A. C. Bryce, C. Button, and J. H. Marsh, "Fabrication of electroabsorption optical modulators using laserdisordered GaInAs/GaInAsP multiquantum-well structures", Electron. Lett., **30**, pp. 1623-1625, 1994

7. A. McKee, C. J. McLean, G. Lullo, A. C. Bryce, R. M. De La Rue, and J. H. Marsh, "Monolithic integration in InGaAs-InGaAsP multiple-quantum-well structures using laser intermixing", IEEE J. of Quantum Electron. **33**, pp. 45-55, 1997

8. M.G. Holland, "Semiconductors and Semimetals", Acdemic, New York, 2, 1967

9. W.P. Dumke, "Spontaneous radiative recombination", Physical Review, **105**, pp. 139-144, 1957

10. C. J. McLean, A. McKee, G. Lullo, A. C. Bryce, R. M. De La Rue, and J. H. Marsh, " Quantum well intermixing with high spatial selectivity using a pulsed laser technique", Electron. Lett., **31**, pp. 1285-1286, 1995

11. S. J. Fancey, G. S. Buller, J. S. Massa, A. C. Walker, C. J. Mclean, A. McKee, A. C. Bryce, J. H. Marsh and R. M. De La Rue, "Time-resolved photoluminescence microscopy of GaInAs/GaInAsP quantum wells intermixed using pulsed laser technique," *J. Appl. Phys.*, Vol. 79, pp. 9390-9392, 1996

12. B.S. Ooi, B.Qiu, A.C. Bryce, R.M. De La Rue, J.H. Marsh, and C. Button, "The influence of Sn- and S-doped substrates on thermal stability and the quantum well intermixing of GaInAs/GaInAsP structure", To be published.

13. B.S. Ooi, A.C. Bryce, J.H. Marsh, and J. Martin, "Transmission electron-microscopy study of fluorine and boron-implanted and annealed GaAs/AlGaAs", Apply. Phys. Lett., **65**, pp. 85-87, 1994

14. J.H.Marsh, O.P. Kowalski, S.D. McDougall, B.C. Qiu, A. McKee, C.J. Hamilton, R.M. De La Rue, A.C. Bryce, "Quantum well intermixing in material systems for 1.5 microns" , Accepted by J. of Vacuum Science and Technol. (A).

15. J. Crank, "The Mathematics of Diffusion", Second Edition, Clarendon Press, Oxford, 1975

16. D.P. Davé, " Numerical technique to calculate eigenenergies of quantum-wells with arbitrary potential profile", Electron.. Lett., **27**, pp. 1735-1736, 1991

17. K.Nakamura, A.Shimizu, M. Koshiba, and K. Hayata, "Finite-element analysis of quantum well of arbitrary semiconductors with arbitrary potential profiles", J. Quantum Electron. **25**, pp. 889-895, 1989

18. W.W. Lui, M.Fukuma, "Exact solution of the Schrödinger Equation across an arbitrary one-dimensional piecewise-linear potential barrier", J. Appl. Phys., **60**, pp. 1555-1559, 1986

19. Y. Ando, and T. Itoh, "Calculation of transmission tunnelling current across arbitrary potential barriers", J. Appl. Phys. **61**, pp. 1497-1502, 1987

20 R. Leon, Y. Kim, C. agadish, M.Gal, J. Zou, D.J.H. Cockayne, "Effects of interdiffusion on the luminescence of InGaAs/GaAs quantum dots", Appli. Phys. Lett., **69**, pp.1888-1890, 1996

4. Multimode Interference Coupler Design, Fabrication and Characterisation

4.1 Introduction

Optical couplers are key components in photonic integrated circuits both for signal routing and signal processing, being used in power dividers, modulators and switches, wavelength multiplexers and demultiplexers and polarisation splitter. There are several types of coupler being used, such as directional couplers, zero gap two-mode interference couplers (TMI) and multimode interference (MMI) couplers. The major drawback of directional couplers is their large size, typically, several mm or more, due to their big coupling length. TMI couplers consist of a two moded central waveguide (TMI section) connected to a pair of single-moded access waveguides. Compared to directional couplers, TMI couplers are shorter, less sensitive to fabrication variations and less polarisation dependent. However, the requirements of high power coupling efficiency and proper mode excitation from the single-moded access waveguides to the TMI section limit the branching angle of access waveguides to very small values (typically <2°) [1]. Due to the finite resolution of the lithographic process, part of the area between the access waveguides cannot be well defined. This introduces considerable uncertainty in the actual length of TMI section, causing a spread in coupler performance. Moreover, due to the proximity of the access waveguides, extra modal coupling occurs [2], adding to the performance spread.

Replacing the TMI section with a (wider) MMI section will allow a good separation between the access waveguides, eliminating the performance spread due to both the limitation of the lithographic process resolution and the extra coupling in the access waveguides. Furthermore, due to the high number of modes supported by the MMI section, power coupling efficiencies are high and consequently device excess losses are lower compared to those of TMI couplers.

In this chapter, the basic waveguide theory and design are reviewed, and the design, fabrication and assessment of MMI couplers, using InGaAs/InGaAsP multi-quantum wells material are documented. Important MMI coupler performance parameters such as the split ratio, which is the ratio of optical power from one of the output waveguide to that from the other, are presented.

4.2 Guided Waves in a Slab Dielectric Waveguide

4.2.1 Maxwell's Equations

The waveguide is the basic component of optoelectronic devices which interconnects the various components of an optical integrated circuit. The behaviour of light in a waveguide can be exactly described by Maxwell's Equations, in terms of the electromagnetic field , as follows:

$$\nabla . \boldsymbol{D} = \rho \tag{4.1}$$

$$\nabla . \boldsymbol{B} = 0 \tag{4.2}$$

$$\nabla \mathrm{x} \boldsymbol{E} = -\frac{\partial \boldsymbol{B}}{\partial t} \tag{4.3}$$

$$\nabla \mathrm{x} \boldsymbol{H} = \frac{\partial \boldsymbol{D}}{\partial t} + \boldsymbol{J} \tag{4.4}$$

where $\boldsymbol{D}$ is electric displacement density, $\boldsymbol{E}$ is electric field strength, $\boldsymbol{B}$ is magnetic induction density, $\boldsymbol{H}$ is magnetic field strength and ρ is electric charge density. In addition

to these equations, there is a set of relationships known as the material equations, which link the field strength $\boldsymbol{E}$ and $\boldsymbol{H}$ with the flux densities $\boldsymbol{D}$ and $\boldsymbol{B}$ respectively, through a set of material coefficients which are representative of the bulk properties of matter. There are three of them, written as

$$\boldsymbol{J} = \sigma \boldsymbol{E} \tag{4.5}$$

$$\boldsymbol{D} = \varepsilon \boldsymbol{E} \tag{4.6}$$

$$\boldsymbol{B} = \mu \boldsymbol{H} \tag{4.7}$$

Here $\boldsymbol{J}$ is electric current density, σ is conductivity, ε is dielectric constant, and μ is magnetic permeability. From the equations above, the wave equation can be derived as

$$\nabla^2 \boldsymbol{E} = \mu\varepsilon \frac{\partial^2 \boldsymbol{E}}{\partial t^2} = \frac{n^2}{c^2} \frac{\partial^2 \boldsymbol{E}}{\partial t^2} \tag{4.8}$$

$$\nabla^2 \boldsymbol{H} = \mu\varepsilon \frac{\partial^2 \boldsymbol{H}}{\partial t^2} = \frac{n^2}{c^2} \frac{\partial^2 \boldsymbol{H}}{\partial t^2} \tag{4.9}$$

Here, $n = \sqrt{\varepsilon_r}$ is the refractive index of material, ε_r is relative dielectric constant, $c = \sqrt{\mu\varepsilon_0}$ is light velocity in vacuum, and ε_0 is dielectric constant of vacuum. It should be noted that assumptions of $\rho = 0$ and $\boldsymbol{J} = 0$ were made when the wave equations were derived.

The field vector $\boldsymbol{E}$ ($\boldsymbol{H}$) is generally a function of space position (x, y, z) and time t. However, it is often the case that all fields involved will be harmonically varying at single angular frequency ω. This will occur in many situations involving monochromatic light. It is then convenient to eliminate any time-dependency by assuming a consinusoidally-varying solution to the wave equations (4.8) and (4.9),

$$\boldsymbol{E}(x, y, z, t) = \boldsymbol{E}(x, y, z) e^{j\omega t} \tag{4.10}$$

where the function $\boldsymbol{E}(x, y, z)$ accounts for the spatial dependence of the field, while the exponential $e^{j\omega t}$ describes the time-variation. The use of such complex notation is standard in electromagnetic theory. With this assumption, the wave equation can be reduced to

$$\nabla^2 \boldsymbol{E} = n^2 \frac{\omega^2}{c^2} \boldsymbol{E} = K_0^2 \boldsymbol{E} \tag{4.11}$$

where $K_0 = \frac{n\omega}{c} = n\frac{2\pi}{\lambda_0}$ is the propagation constant, and λ_0 is the wavelength of light considered in free space.

4.2.2 Guided Waves in a Slab Dielectric Waveguide

4.2.2.1 Transverse Field Distribution

The boundary conditions for electromagnetic waves propagating in a waveguide at the interfaces of the waveguide lead to the waves travelling in distinct modes. A mode, in this sense, is a spatial distribution of optical energy in one or more dimensions. A slab waveguide is a type of the simplest waveguides in which optical waves are guided in one dimension. Fig. 4.1 is a schematic representation of a three layer waveguide, or slab waveguide.

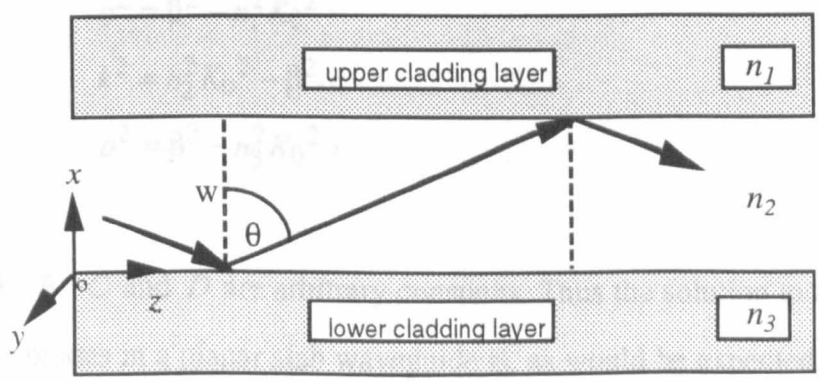

Fig. 4.1 Schematic diagram of a three layer waveguide

In a three layer slab waveguide, the composition of the layers is chosen such that $n_1 < n_2 > n_3$ as shown in Fig. 4.1. The effect of sandwiching high refractive index material between two lower index layers is that the light is confined or "guided" due to the principle of total internal reflection, when the light travels down along the waveguide. For simplicity, only waves of TE polarisation will be considered in the first instance. In this case, the components of electrical field $\boldsymbol{E}$ in x and z direction are 0. The $\boldsymbol{E}$ field of a wave travelling in the z direction, with propagation constant β can be written as:

$$E = E_x = E(x)e^{j(-\beta z)} \tag{4.12}$$

Substituting this equation into equation (4.11), the wave equation is reduced to

$$\frac{d^2E}{dx^2} - (\beta^2 - n_i^2 K_0^2)E = 0 \tag{4.13}$$

where n_i (i=1, 2, 3) are the indices of the three different layers. The solutions of the differential Eq. (4.13) are

$$E = A\exp[-q(x-w)] \qquad w<x \tag{4.14a}$$

$$E = B\cos(kx - \Phi) \qquad 0<x<w \tag{4.14b}$$

$$E = C\exp(px) \qquad x<0 \tag{4.14c}$$

where

$$q^2 = \beta^2 - n_1^2 K_0^2 \,, \tag{4.15a}$$

$$k^2 = n_2^2 K_0^2 - \beta^2 \,, \tag{4.15b}$$

$$p^2 = \beta^2 - n_3^2 K_0^2 \,, \tag{4.15c}$$

and the A, B, C and D are arbitrary constants. Thus the solution to the wave equation for guided modes in a planar slab waveguide is, as would be expected, oscillatory in the guiding region and exponentially decaying outside of that region.

4.2.2.2 Resonant Conditions

The boundary conditions require that $E(x)$ and its gradient $\frac{dE(x)}{dx}$ are continuous at each interface $x=0$ and $x=w$. Application of the boundary conditions to the equations (4.14) yields the following dispersion relation which is also known as the eigenvalue equation:

$$2kw - 2\Phi_1 - 2\Phi_2 = 2m\pi \tag{4.16}$$

where

$$\tan\Phi_1 = \frac{q}{k}, \tag{4.17}$$

$$\tan\Phi_2 = \frac{p}{k}, \tag{4.18}$$

and m=0, 1, 2... is the order of mode, and Φ_1, Φ_2 are the Goos-Hänchen shifts [1] Eq.(4.16) indicates that the total phase change of a point on a wavefront which travels up and down in the x-direction for a round trip must be a multiple of 2π, in order to have constructive interference. The dispersion equation (4.16) can also be written as:

$$\tan(kw) = \frac{k(p+q)}{k^2 - pq} \tag{4.19}$$

It can be shown that only certain values of β can satisfy Eq. (4.19), which means the waveguide will only support a discrete set of guided modes. In the case of a symmetric waveguide, the eigenvalue equation can be reduced to

$$\tan\left(\frac{kw}{2}\right) = \frac{p}{k} \qquad \text{Even modes} \tag{4.20}$$

$$\tan\left(\frac{kw}{2}\right) = -\frac{k}{p} \qquad \text{Odd modes} \tag{4.21}$$

It is convenient to define the normalised thickness as:

$$V = K_0 w (n_2^2 - n_1^2)^{1/2} \tag{4.22}$$

then the eigenvalue equation can be further reduced to

$$\tan(u) = \frac{\frac{V^2}{4} - u^2}{u} \qquad \text{Even modes} \tag{4.23}$$

$$\tan(u) = -\frac{u}{\frac{V^2}{4} - u^2} \qquad \text{Odd modes} \tag{4.24}$$

where $u = \frac{kw}{2}$

For light with TM polarisation, by analogy with equation (4.19) the dispersion equation can be obtained as

$$\tan(kw) = \frac{k\left(p\frac{n_2^2}{n_3^2} + q\frac{n_2^2}{n_1^2}\right)}{k^2 - p\frac{n_2^2}{n_3^2}q\frac{n_2^2}{n_1^2}} \tag{4.25}$$

The eigenvalue equation is a transcendental equation, so it can only be solved numerically or graphically. Fig. 4.2 shows a typical graphic representation of eigenvalue equations (4.20) and (4.21), for different normalised thickness V_1 and V_2, and indicates that the waveguide can support 2 and 4 TE modes for V_1 and V_2 respectively.

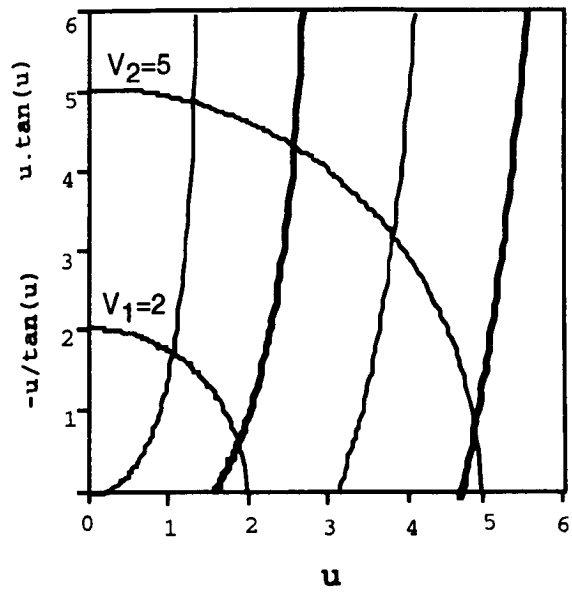

Fig. 4.2 Graphic solution of the eigenequations. The solutions for the even and odd modes are represented by the cross points of the V-curve with the thin and thick lines, respectively

The graphic method is a simple and straightforward way, but of limited accuracy. Alternatively, the eigenvalue equations can be easily solved by numerical methods, which can offer very high precision. The table 4.1 shows the results of numerical solution.

table 4.1 Numerical results for different normalised thickness

V value	u0(1st mode)	u1(2nd mode)	u3(3rd mode)	u4(4th mode)
2	1.02988	1.8955		
5	1.30644	2.5958	3.8375	4.9063

4.2.2.3 Cut-off conditions

In order for the slab waveguide to guide light, the propagation constant must lie in the range $n_{1,3}K_0<\beta<n_2K_0$. If $\beta = n_1K_0$ for a particular wavelength, light will no longer be confined by the waveguide, but will refract into the cladding layers. If this occurs, the waveguide cannot propagate light at this frequency. This is known as the cut off

condition. For the case of a symmetric waveguide ($n_1 = n_2$), it can be found from equations (4.16)-(4.18) that the cut-off condition for TE polarised light is given by:

$$V = K_0 w (n_2^2 - n_1^2)^{1/2} = m\pi \tag{4.26}$$

or

$$\Delta n = (n2 - n1) > \frac{m^2 \lambda_0^2}{4w^2(n_1 + n_2)} \qquad (m=0,\ 1,\ 2,...) \tag{4.27}$$

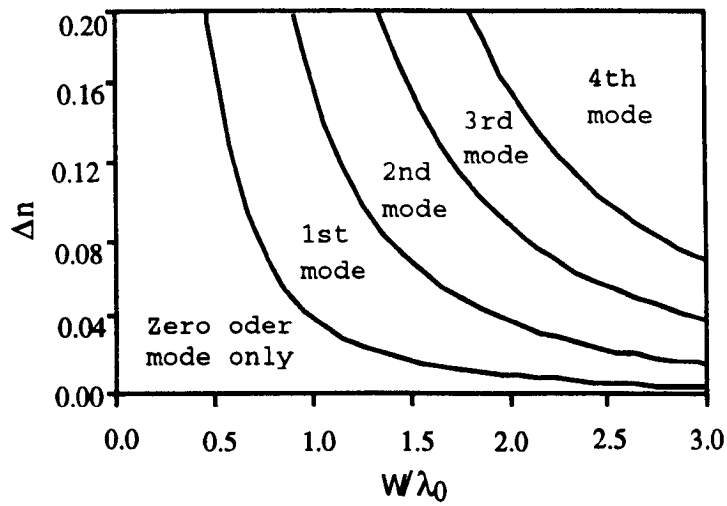

Fig. 4.3 Mode cut-off conditions for a symmetrical three layer waveguide

Fig. 4.3 shows the mode cut-off conditions for a symmetric three layer waveguide. As can be seen, larger refractive index differences, and larger waveguide widths will support more modes. The lowest mode (zero order mode) does not exhibit a cut-off as all the others do, which implies that light at any wavelength is guided in this mode no matter how small the refractive change, or guided layer thickness is.

4.3 Channel waveguides

The slab waveguides discussed in the preceding sections only provide one-dimensional optical confinement. Two-dimensional optical confinement is required in many device

configurations such as a variety of lasers, switches, and others based on ridge and buried waveguide configurations. The additional confinement can help to bring about desirable device characteristics such as low threshold current, possible single mode operation, or savings in drive power. The following section will discuss the solutions for guiding in rib or stripe guides. Examples of these types of guide, in which the light is confined laterally as well as vertically, are shown in Fig. 4.4.

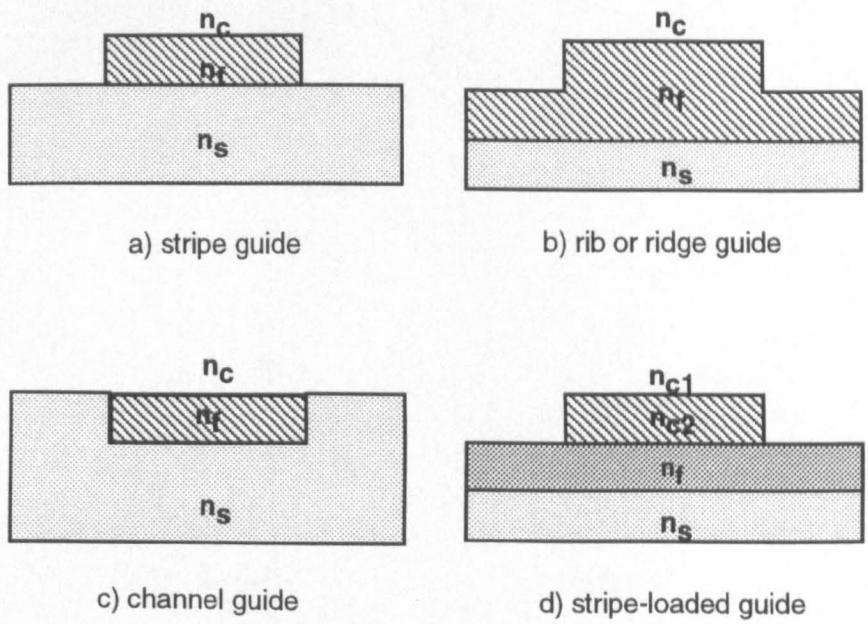

Fig. 4.4 Examples of different geometries used to confine light both vertically and laterally.

4.3.1 Numerical Methods

For simplicity, Figure (4.4) shows abrupt transitions of refractive index. However, it should be noted that fabrication techniques such as diffusion may produce guide cross sections with graded-index profiles. In all examples, the light is essentially confined to the film material with index n_f. In a channel guide the refractive index $n = n(x, y)$ is a function of both transverse coordinates. As a result, the analysis of waveguide modes becomes a more complex task than for slab guides. A variety of methods has been reported, suitable for numerical analysis of channel waveguides such as the beam

propagation method (BPM) [4, 5], finite element method (FEM) [6-8] and finite difference method (FDM) [9-11].

The BPM based on constructing a relation called the BPM equation, that connects the electromagnetic fields in two axially separated parallel planes. The field distribution in one plane is calculated numerically from the distribution in the preceding plane using a BPM equation. Beam propagation methods repeat this procedure recursively, thus they complete the simulation of wave propagation step by step with an arbitrary excitation. BPM equations inherently take guided wave as well as radiation fields into account. They also allow axial index variations. Due to these two important features, beam propagation methods serve as most versatile numerical tools to study various types of optoelectronic devices.

FDMs are directly based on the discretization of Maxwell's equation for the guide with appropriate boundary conditions. The modal field solution is transformed in this case into a matrix eigenvalue problem, which is solved by a standard numerical iterative procedure. It should be pointed out that a program called FWAVE [11], written by Michael Taylor of this department is available within the department.. The program is based on a finite difference method and can solve field distributions in waveguides, couplers and arbitrary defined structures. Fig. 4.5 shows a FWAVE solution for a typical waveguide structure. The contours represents the electric field at 10% increments, with the outmost contour representing the electric field at 1% of its peak value.

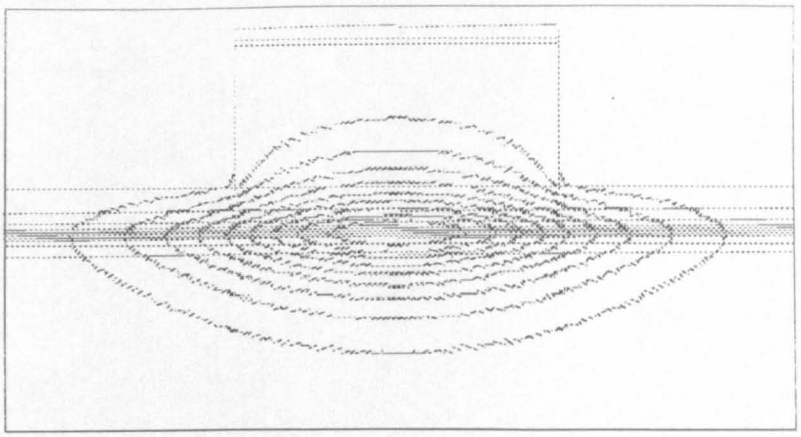

Fig. 4.5 An FWAVE solution for a ridge waveguide with ridge width and height of 2.5 μm and 1.55 μm respectively.

4.3.2 Effective Index Method [12-14]

The effective index method (EIM) is a relatively straightforward means of analysing a strip waveguide structure, although it is less accurate than the most other numerical methods. Because of its immediate intuitive appeal, this approach has been used since the beginnings of integrated optics.

Fig. 4.6 (top) shows a ridge waveguide structure, which can be divided into 3 regions as labelled. Due to the fact that the waveguide in the central region is thicker than the regions 1 and the 3, the effective index in the central region is larger than in the other regions. By applying the slab waveguide theory to the 3 regions individually, and solving the characteristic multi-layer eigenvalue equations, we can obtain the effective indices n_{eff1}, n_{eff2}, n_{eff3}, corresponding to the regions 1, 2 and 3, respectively. The original 2-D problem can now be simplified into a 1-D problem, as is also shown in Fig. 4.6 (the lower figure), and this 1-D problem can be solved using equations (4.23) and (4.24). But it should be noted that, instead of solving for TE polarised light, the light is now TM polarised.

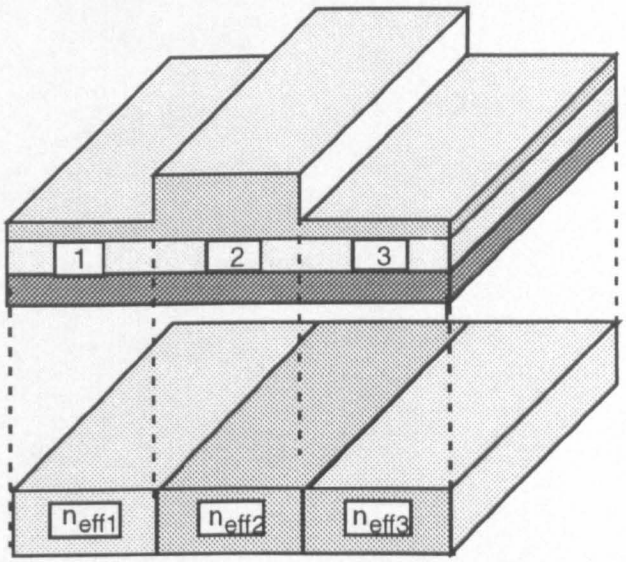

Fig. 4.6 Converting a 2-D ridge waveguide structure into a 1-D slab problem by using the EIM.

4.4 Basic Theory of MMI Couplers

Essentially, an MMI device consists of three parts: a wide MMI section, a single or set of input waveguides and a single or set of output waveguides, as shown in Fig. 4.7. The operation of the MMI coupler is based on the selfimaging property of a multimode waveguide, as suggested by Brygdahl [15] and described in more detail by Ulrich [16]. There are three types of MMI phenomena: general self-imaging, restricted self-imaging, and symmetric power splitting, depending on the excitation conditions of the MMI section by the input waveguides. From the slab waveguide theory, we have the following relations:

$$k_x^2 + \beta_m^2 = (K_0 n)^2 \tag{4.28}$$

where, β_m is propagation constant in the waveguide, and n is the refractive index of the waveguides. When the propagation constant β_m is very close to $K_0 n$, it can be deduced from equations (4.23) and (4.24) that

$$k_x \equiv \frac{(m+1)\pi}{W} \qquad m=0,1,2... \tag{4.29}$$

where W is the width of the waveguide. Combining Eq.(4.28) and (4.29), we have

$$\beta_m = \sqrt{K_0^2 n^2 - \frac{\pi^2}{W^2}(m+1)^2} \equiv K_0 n - \frac{\pi^2 (m+1)^2}{2K_0 n W^2} \tag{4.30}$$

Defining the beat length

$$L_\pi \equiv \frac{\pi}{\beta_0 - \beta_1} = \frac{4nW^2}{3\lambda_0} \tag{4.31}$$

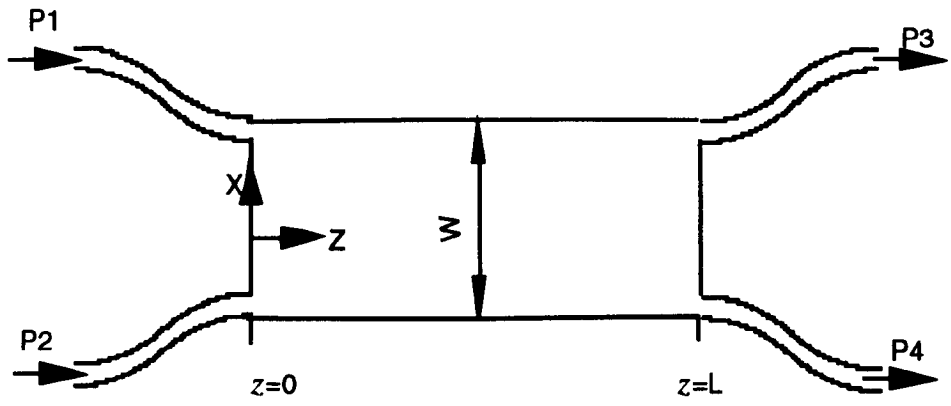

Fig. 4.7 Schematic structure of a multimode interference coupler

then the propagation constants β_m of the modes in the MMI section become

$$\beta_m = K_0 n - \frac{\pi(m+1)^2}{3L_\pi} \tag{4.32}$$

In the MMI section, the total lateral field $h_y(x,z)$ at any position z can be written as a linear combination of the field $h_{y,m}(x)$ of the M guided modes:

$$h_y(x,z) = \sum_{m=0}^{M-1} c_m h_{y,m}(x) \exp(-j\beta_m z) \tag{4.33}$$

where the coefficients c_m determine the relative contribution of each mode. In particular, the total lateral field profile at the entrance (z=0) of the MMI section is

$$h_y(x,0) = \sum_{m=0}^{M-1} c_m h_{y,m}(x) \tag{4.34}$$

which reflects the decomposition of the input field profile into all possible guided modes. The coefficients of this decomposition can be found from the overlap integral formed between the input field profile $h_y(x,0)$ and each guided mode $h_{y,m}(x)$:

$$c_m = \frac{\int h(x,0) h_m(x) dx}{\int |h_m(x)|^2 dx} \tag{4.35}$$

Inspection of the phase factor leads to the following equations:

$$h(x, L_{MMI}) = h(x,0) \qquad \text{for } z = L_{MMI} = (2q)(3L_\pi) \tag{4.36}$$

$$h(x, L_{MMI}) = -h(x,0) \qquad \text{for } z = L_{MMI} = (2q+1)(3L_\pi) \tag{4.37}$$

$$h(x, L_{MMI}) = \frac{j(-1)^q + 1}{2} h(x,0) + \frac{j(-1)^q - 1}{2} h(-x,0)$$

$$\text{for} \qquad z = L_{MMI} = (q + \frac{1}{2})(3L_\pi) \tag{4.38}$$

where q=0, 1, 2,..., and L_{MMI} is the length of MMI section. From equations (4.36)-(4.38), it can be concluded that:

a. When $L_{MMI} = (2q)(3L_\pi)$, the field at the entrance is reproduced at the end of MMI section and the coupler is in the bar state.

b. When $L_{MMI} = (2q+1)(3L_\pi)$, the field at the end of MMI section is an yz-plane image of the field at the entrance and the coupler is in the cross state.

c. When $L_{MMI} = (q+\frac{1}{2})(3L_\pi)$, the field at the end of MMI section is a linear combination of the original field at the entrance plane and the coupler is in the 3 dB state.

To see this let

$$\text{q=0},\ h_x(y,0) = P_1 = E_1\ ,\ h_x(-y,0) = P_2 = E_2\ ,$$

then

$$P_3 = E_3 = h_x(y, L_{MMI}) = \frac{j+1}{2}E_1 + \frac{j-1}{2}E_2 \qquad (4.39a)$$

$$P_4 = E_4 = h_x(-y, L_{MMI}) = \frac{j+1}{2}E_2 + \frac{j-1}{2}E_1 \qquad (4.39b)$$

Eq.(4.39) shows that the input optical power ($\propto |E_1|^2$) is split into exactly two equal parts ($\propto |E_3|^2$ and $\propto |E_4|^2$).

4.5 3-dB MMI Coupler Design

4.5.1 Material Structure

The material structure (Fig. 4.8) used in the design of MMI the coupler was grown by metal organic vapour phase epitaxy (MOVPE) on an (100)-oriented n-type InP substrate and consisted of five 37 Å InGaAs wells with 120 Å InGaAsP (λ_g=1.26 μm, where λ_g is the wavelength corresponding to the bandgap) barriers. The active region was bounded by a stepped graded index (GRIN) waveguide core consisting of InGaAsP confining layers. The thicknesses and compositions of these layers (from the QWs outward) were 500 Å of InGaAsP with λ_g=1.18 μm and 800 Å of λ_g=1.05 μm. The structure, which

was lattice matched to InP throughout, was completed by an InP cladding layer, an InGaAs contact layer and InP cap layer. The upper cladding layer of 1.4 μm was doped with Zn to a concentration of $7x10^{17}$ cm^{-3}. The lower cladding layer was Si doped to a concentration of $2X10^{18}$ cm^{-3}. The waveguide core was undoped, thus forming a *pin* structure with the intrinsic region restricted to the QWs and GRIN layers. The emitting wavelength of the material was 1.48 μm.

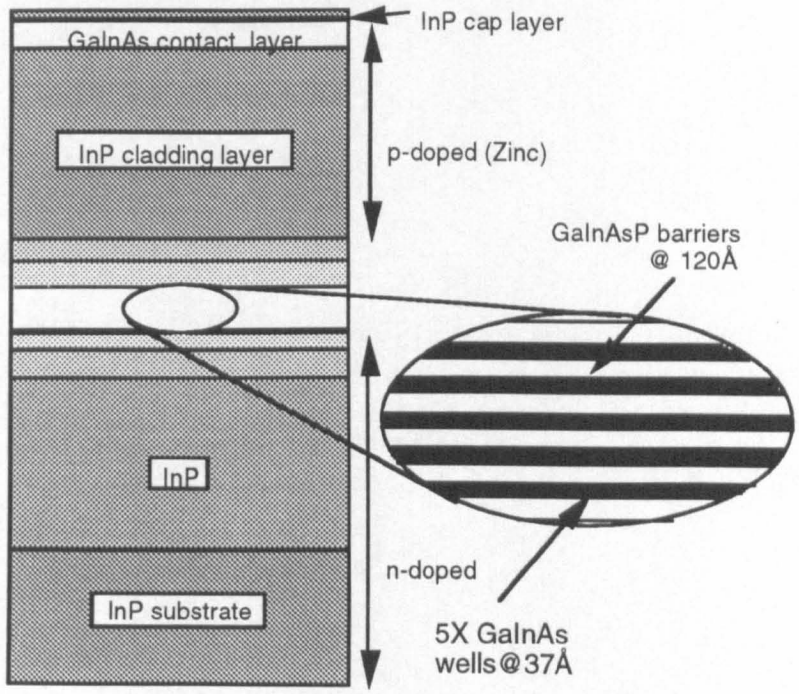

Fig. 4.8 Structure of the material used to fabricate MMI couplers

4.5.2 Refractive Indices of the Material

In order to design a waveguide device, it is necessary to obtain accurate values of refractive indices of the different layers involved. There are many reports in literature concerning the modelling and experimental measurements for InP and related compounds (see chapter 2), but, there is some disagreement between the data quoted. Here we use the following equation [17] to calculate the refractive index of quaternary material $In_{1-x}Ga_xAs_yP_{1-y}$ for working wavelength of 1.55 μm:

$$n = \{(1-y)[8.4x + 9.6(1-x)] + y[13.1x + 12.2(1-x)]\}^{1/2} \qquad (4.40)$$

Table 4.2 shows refractive indices for the layers involved in the structure (Fig. 4.8). Although the refractive index of InP can be calculated in same way, a very accurate measurement datum of 3.1688 [18], was used.

Table 4.2 Refractive index of $In_{1-x}Ga_xAs_yP_{1-y}$

y	wavelength corresponding to bandgap(μm)	Refractive index
0.25	1.05	3.1855
0.45	1.18	3.2701
0.55	1.25	3.3145
1	1.65	3.5525

4.5.3 Modelling of MMI Couplers

Ridge-type waveguides were analysed using the EIM. The effective index of the multi-layer slab structure was calculated using the program FWAVE. For the typical laser structure with an upper InP cladding thickness of 1.4 μm shown in Fig 4.8, the effective index is 3.194 and 3.189 for the TE and TM polarisations, respectively.

The difference of index between the region 2 and regions 1 and 3 (refer to Fig. 4.6) for a given ridge step (or upper cladding thickness) can be decided from the dependence of the effective index of a multi-layer slab structure on the thickness of upper cladding layer (Fig. 4.9). It should be pointed out that a contact layer with thickness of 0.15 μm is included in the figure.

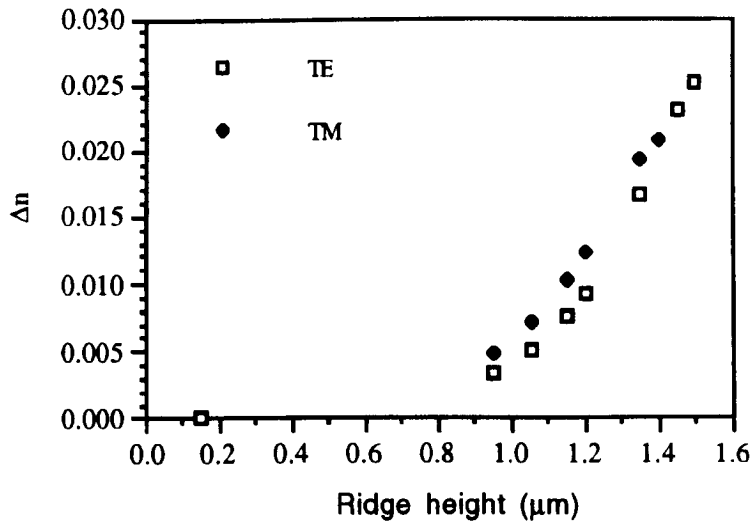

Fig. 4.9 Calculated refractive index difference between the region 2 and regions 1 and 3.

With the index and index difference calculated above, the lateral field profile at any position in the MMI section can be obtained. By solving Eq.(4.33), an overlap integral between the field at the end of the MMI section and the field at the output waveguides allows the optical power in each output branch to be predicted. With the procedure just described, sensitivity analysis can be performed of the behaviour of the couplers on fabrication parameters (e.g., the MMI section width, length, etc.). For the 3-dB couplers, the two most important parameters, namely, the excess loss and splitting ratio, (refer to Fig. 4.7) are defined as follows:

$$\text{Insertion loss} = 10\log\left(\frac{p_3 + p_4}{p_1}\right) \tag{4.41}$$

$$\text{splitting ratio} = 10\log\left(\frac{p_3}{p_4}\right) \tag{4.42}$$

Fig. 4.10 and Fig. 4.11 show the simulated results for 3-dB couplers with an MMI section width of 9.4 μm, and the length being varied from 430-460 μm. Apparently, the optimum MMI section length should be around 450 μm from the point of view of the

lowest insertion loss, although the split ratio between the two outputs of the 3-dB MMI coupler does not change very much for MMI section lengths in the range 430-460 μm.

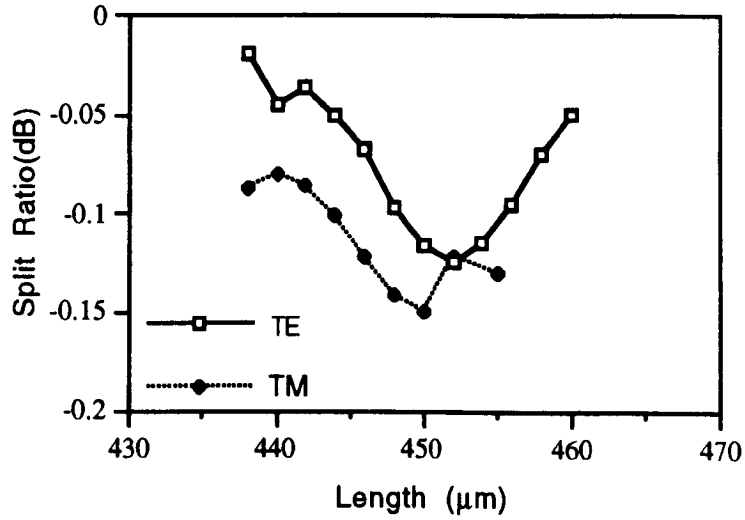

Fig. 4.10 Split ratio Vs MMI section length for TE and TM polarisation

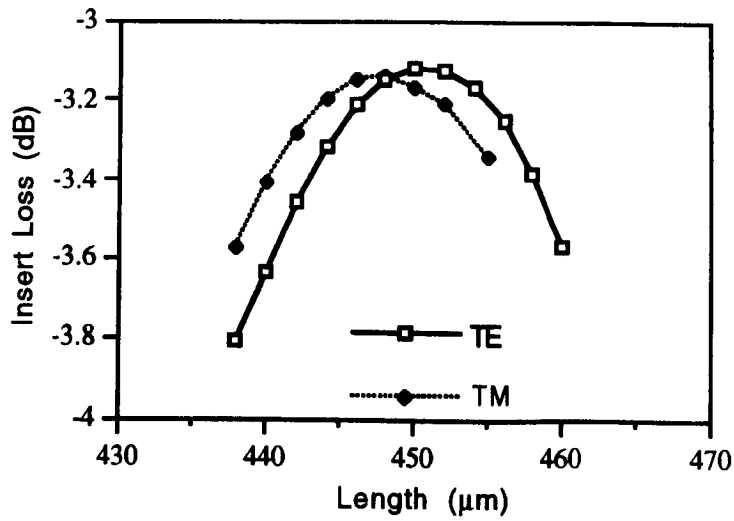

Fig. 4.11 Insertion loss Vs length of MMI section for TE and TM polarisation

4.6 Fabrication of 3-dB MMI Couplers

As fabrication errors are almost inevitable and inaccuracy of the refractive index of the material could occur, for example, it is found that the dry etched waveguide likely has a smaller waveguide width compared to that of the design, hence the designed couplers had

an MMI section width of 10 μm, and whose length was varied from 400 μm-550 μm in steps of 10 μm to hit the optimum value. Curved access waveguides are required to increase the separation between the waveguides to avoid any possible coupling and interference between the access waveguides. Furthermore, larger separation between the access waveguides is an advantage from the point of view of coupling light into one of the waveguides. Although the simulation [19] suggested that curvature radius of R=200 μm for a circular waveguide suffices for low loss, we conservatively employed a circular bend of 400 μm for the access waveguides whose widths were 2.5 μm.

The devices were fabricated with the material structure shown in Fig. 4.8 The cleaned samples were coated with PECVD SiO_2 of thickness 200 nm, and then patterns were defined using photolithography. Dry-etching of the SiO_2 by RIE using gas C_2F_6 was used to transfer the patterns to the sample. Using the SiO_2 as dry etch mask, the sample was etched using gases $CH_4/H_2/O_2$ until a ridge step of 1.55 μm was achieved. The sample was finally thinned to around 200 μm to improve cleaving and then cleaved into a group of devices with same MMI section length. Fig. 4.12 is a SEM micrograph of a 3-dB MMI device.

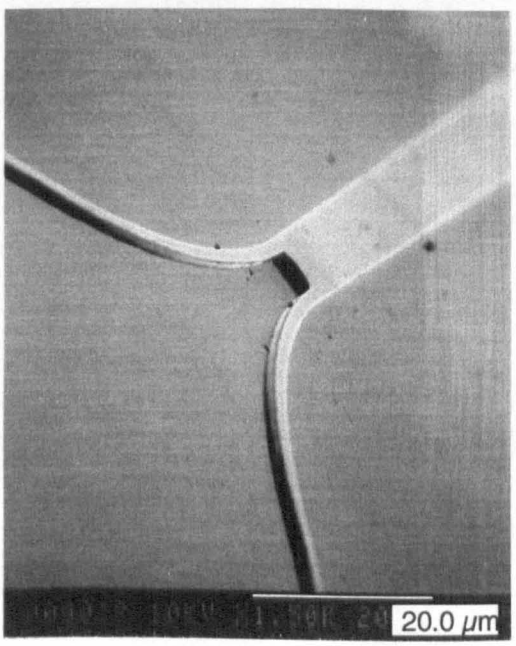

Fig. 4.12 SEM micrograph of an MMI coupler.

4.7 Assessment of 3-dB MMI Couplers

The experimental set-up is shown in Fig. 4.13. A laser beam from a 1.55 μm tuneable semiconductor laser was aligned to the one of input waveguides, the output light was collected by a Ge detector or camera, then the signals were amplified by a lock-in amplifier. To filter the background light and the light from the other output waveguide, an iris was adjusted so that only the light from the output waveguide being measured was detected. Fig. 4.14 and Fig. 4.15 show the measured split ratio.

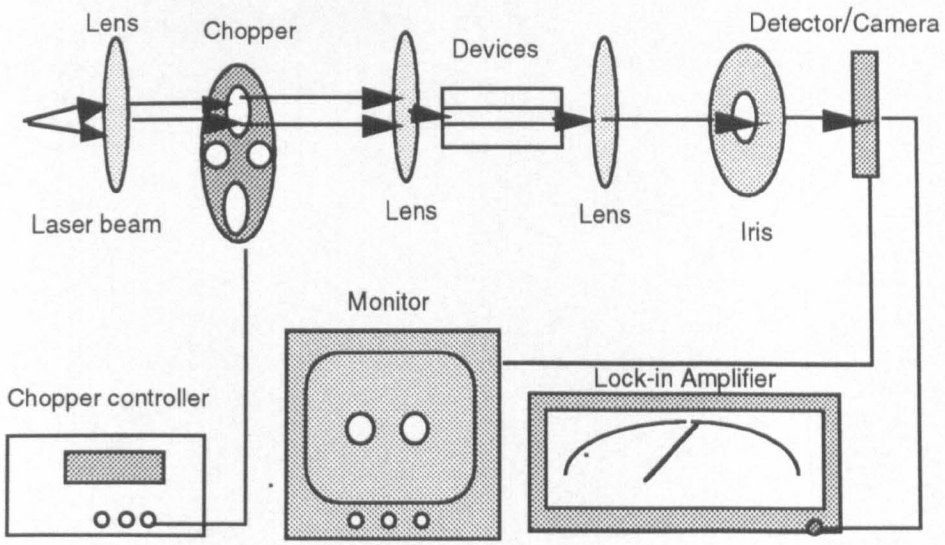

Fig. 4.13 Experimental set-up.

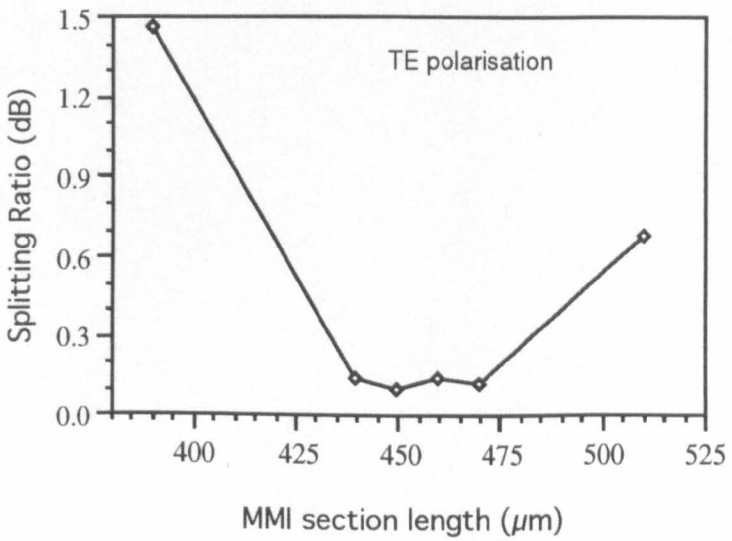

Fig. 4.14 Measured split ratio of the MMI coupler against MMI section length at λ=1.55 μm.

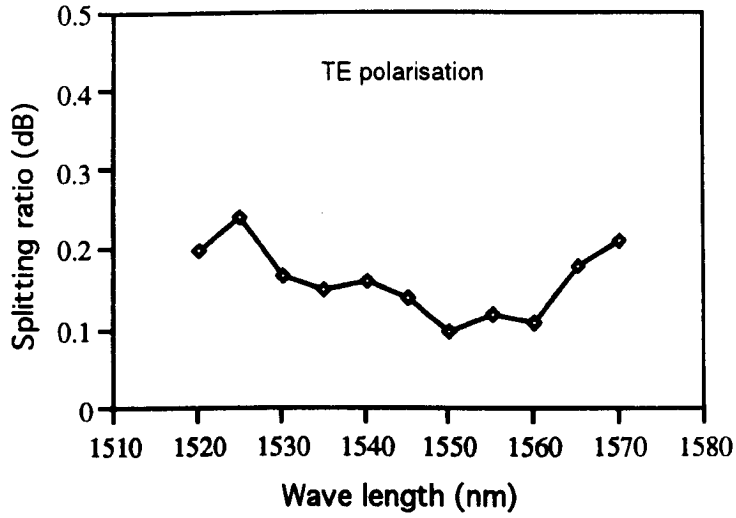

Fig. 4.15 Split ratio dependence of wavelength at λ=1.55 μm.

From Fig. 4.14 and Fig. 4.15, it can be seen that the optimum MMI section length lay in the range 440-460 μm, which is consistent with the design for an operation wavelength of around 1550 nm.

4.8 3-dB MMI Coupler Fabrication and Measurement with Bandgap-Shifted Material

Integration of MMI couplers with other active devices such as amplifiers and modulators, has wide applications in optical fibre communication. To demonstrate the possibility of this integration, 3-dB MMI couplers were fabricated with bandgap-shifted material. The material structure is identical to that shown in Fig. 4.8, except that the width of the wells was 65 Å, instead of 37 Å. The emitting wavelength of the as-grown material was accordingly, 1.55 μm. QWI was carried out for the material using PAID process. A blue-shift of around 110 nm was achieved across the sample. 3-dB MMI couplers were fabricated using same process as described previously. Measurement was performed using a set-up similar to that shown in Fig. 4.13, except that a DFB semiconductor laser working at 1.556 μm was used. Fig. 4.16 is the photo picture of the light from two output waveguides of the devices with different length of the MMI section.

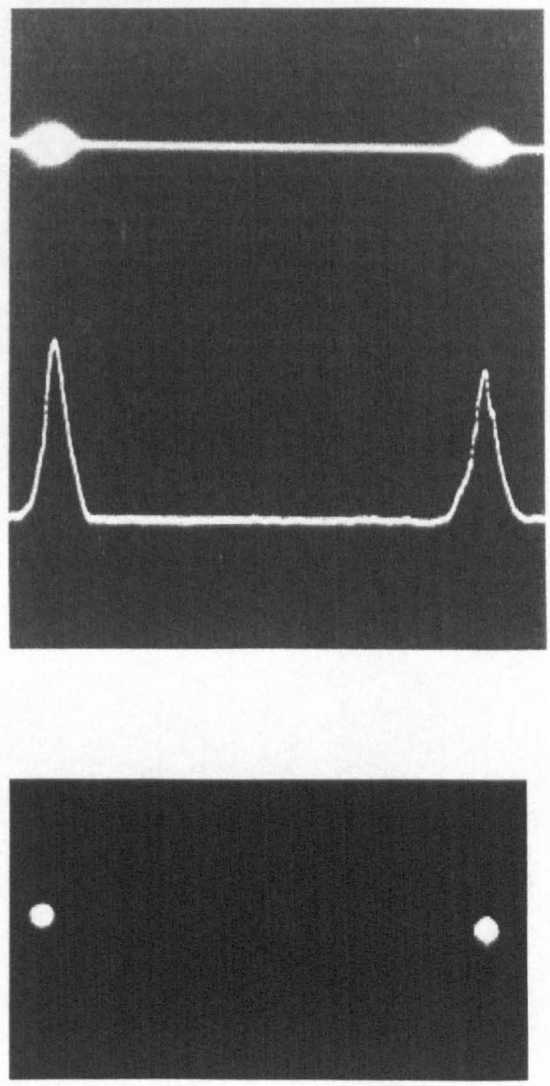

Fig. 4.16 Output from the two output waveguides of the MMI coupler. The length of MMI section is 440 μm (upper) and 470 μm (Lower)

From Fig. 4.16, it can be estimated that the splitting ratios are 0.78 dB (or 54:46) and 0.12 dB (or 51:49) for the upper and lower figure, respectively. Comparing these values to those shown in Fig. 4.15, it appears that the splitting power between the two output waveguides for the MMI section length of 440 μm becomes less equal than for a device with same length of MMI section fabricated using the as-grown material (see Fig. 4.15), this is most likely attributed to fabrication errors.

4.9 Summary

Basic waveguide theory and design are reviewed. The design, fabrication and characterisation of 3-dB MMI couplers has been carried out. The measured results show good agreement with the design, with a splitting ratio of around 0.12 dB for an MMI section length of 470 μm.

Reference

1. D.L. Lee, "Electromagnetic principles of integrated optics", Wiley, New York, 1986

2. C. Caldera et al. "3-dB couplers integrated in InGaAlAs/InP for coherent applications," in Proc. ECOC' 90 (Amsterdam), 1990, PP. 357-360

3. S. Gervorgyan and A. Hovsepyan, "Coupling among waveguides of small spacing", Electron Lett., Vol. **24**, No. 1, PP. 814-815,1988

4. M.D. Feit, J.A. Fleck, "Light propagation in graded-index optical fibres", Applied Optics, **17**, pp. 3990-3997, 1978

5. R. Baets, P.E. Lagasse, "Calculation of radiation loss in integrated-optic tapers and y-junctions", Applied Optics, **21**, pp. 1972-1978, 1982

6. C.W. Yeh, "Optical waveguide theory", IEEE Trans. Circuit Syst. **CAS-26**, pp. 1011-1019, 1979

7. B.M.A. Rahman, F.A. Fernandez, and J.B. Davies, "Review of finite-element methods for microwave and optical wave-guides", Proc. IEEE, **79**, pp. 1442-1448, 1991

8. T. Yamamoto, M. Koshiba, "Numerical-analysis of curvature loss in optical wave-guides by the finite-element method", J. Lightwave Technol, **11**, pp. 1579-1583, 1993

9. P. Lüsse, P. Stuwe, J. Schüle, and H.-G. Unger, "Analysis of vectorial mode fields in optical wave-guides by a new finite-difference method", J. Lightwave Technol, **12**, pp. 487-493, 1994

10. M.S. Stern, "Semivectorial polarised finite-difference method for optical wave-guides with arbitrary index profiles", IEE Proc.-J, **135**, pp. 56-63, 1988

11. M.R.S. Taylor, "FWAVE—A vector E-M solver", Univ. of Glasgow, Glasgow, Scotland, 1993

12. L.M. Walpita, "Calculation of approximate propagation characteristics for any given two-dimensional optical wave-guide", Electron. Lett., **21**, pp. 1075-1076, 1985

13. K.S. Chiang, "Dual effective-index method for the analysis of rectangular dielectric waveguides", Applied Optics, **25**, pp. 2169-2174, 1986

14. E.A.J. Marcatili, A.A.Hardy, "The azimuthal effective-index method", IEEE J. of Quantum Electron., **QE-24**, pp. 766-774, 1988

15. O. Bryngdahl, "Imaging formation using self-imaging technique", J. Opt. Soc. Amer., **63**, pp. 416-418, 1973.

16. R. Ulrich and T. Kamiya, "Resolution of self-imaging in planar optical waveguide", J. Opt. Soc. Amer., **68**, pp. 583-592, 1978

17. The data have been supplied by Dr. M. Fisher, B.T. Labs.

18. G.D. Petti, W.J. Turner, "Refractive index of InP", J Appl. Phys. **36**, pp. 2081 1965

19. Toshio Yamamoto and Masanori Koshiba, "Numerical analysis of curvature loss in optical waveguides by the finite-element method", J. Lightwave Technol. **11**, pp. 1579-1583, 1993

5. Reduced Damage Reactive Ion Etching Process for the Fabrication of InGaAsP/InGaAs Multiple Quantum Well Ridge Waveguide Lasers

5.1 Introduction

InP and related compound semiconductors are increasingly important for applications in optoelectronics and microelectronics due to their unique electrical and optical properties. Ridge waveguides in optoelectronic devices can be fabricated either by wet chemical etching or by dry etching. Wet chemical etching is believed to be a simple, useful and low damage process, but an important problem with wet etching is that the etch rate is isotropic (the same in all directions) or crystallographic (depends on lattice orientation), so adequate dimensional and profile control can be difficult to achieve. Furthermore, if the waveguide involved is curved or circular, as in e.g., ring lasers [1], semiconductor amplifiers with angled facets and demultiplexers for OTDM systems [2-3], the crystallographic orientation dependence may rule out the use of wet etching to form the waveguide.

On the other hand, dry chemical etching has been shown to be an effective technique due to its highly anisotropic nature. Dry etching is a low pressure process that is used to remove material from a surface. Most dry etching processes are based on sputtering by energetic ions or particle bombardment, evaporation of volatile compounds created through reaction with a reactive gas species or, most frequently, a combination of the two. Dry etching processes which involve particle bombardment usually yield vertical or

angled sidewalls regardless of crystallographic orientation. However, the damage which is almost inevitably imparted to the material being etched leads to degradation of the optical and electrical properties of the material [4-7]. It is therefore of great importance to understand and assess the damage, and investigate possible low damage processes for fabrication of optoelectronic devices.

Currently, reactive ion etching based on CH_4/H_2 is the most widely used technique for dry etching In containing semiconductors, because it can give better anisotropy [8, 9] than RIE using Cl and Br containing compounds [10]. Much work has been published on CH_4/H_2 etching. However, there are many different RIE machines used in research establishments, and the etching conditions (gas flow rates, chamber pressure, DC bias etc.) are generally different from machine to machine. Furthermore, the standard process developed in the Department uses DC biases as high as 850 V, which are likely to introduce considerable damage during the etching process. This damage can have detrimental effects on the performance of optoelectronics devices such as ridge lasers to the extent that, in some cases, the devices do not work. It is also known that electrical damage due to hydrogen passivation of acceptors occurs during the RIE CH_4/H_2 process, although such damage can be removed by annealing the etched samples [5, 6] at a temperature of 350°C or greater. Therefore it is of great significance to develop a low damage process for fabrication of optoelctronics devices.

In this chapter RIE damage and its assessment is discussed. The damage was assessed by measuring the damage depth profile using a specially designed multiquantum well (MQW) probe structure and low temperature (5 K) photoluminescence (PL). Post-dry etching annealing was also carried out to investigate its impact on the removal of dry etch damage. Ultimately, 5 μm wide ridge waveguide InGaAs/InGaAsP MQW lasers were fabricated using the RIE dry etching and post-annealing procedure developed and were compared to lasers fabricated by wet chemical etching.

5.2 Reactive Ion Etching

5.2.1 Plasma

Plasma is responsible for the dry etching during the RIE process, therefore an introduction to the properties of plasma is necessary to understand the etching mechanism of RIE. Plasma can be considered as the fourth state of matter, together with solid, liquid and gas, and is defined as: "**A plasma is a quasi-neutral gas of charged and neutral particles which exhibits collective behaviour**" by Chen [11]. Consider a neutral gas which is sealed in a tube to which a DC voltage is applied across two conducting electrodes. The released electrons are accelerated towards the anode and undergo a series of elastic and inelastic collision with the gas molecules and result in the ionisation of the molecules. Thus the plasma is formed. There are several process in plasma which can be described as follows:

Ionisation: In the ionisation process, a primary electron with high kinetic energy impacts with an atom resulting in ionisation of the atom by the release of a secondary electron. e.g.

$$Ar + e \rightarrow Ar^{+} + 2e$$

These two electrons can accelerate and interact with the atoms resulting in further ionisation.

Recombination: Recombination is an inverse process of ionisation, i.e. an electron coalesces with a positive charge and forms a neutral atom;

Excitation: This is a process in which the excitation of a ground-state atom to an excited-state occurs by collision with an electron. This can be expressed as

$$Ar + e \rightarrow Ar^* + e$$

This is the most straightforward example of an elastic collision process. Kinetic energy from the colliding electron is used simply to raise an electron in the atom from a low energy state to one with a higher potential energy.

Relaxation: The excited state may decay by emitting a photon $\hbar\omega$,

$$Ar^* \rightarrow Ar + h\omega$$

Dissociation: If a molecule is electronically excited to a level in a repulsive state, or a level in an attractive state above the binding energy, the molecule will dissociate. The resultant fragments can be atoms, molecules, and ions in either the ground state or some excited state. For example,

$$e + C_2F_6 \rightarrow e + 2CF_3$$
$$e + C_2F_6 \rightarrow 2e + 2CF_3^+$$

Electron attachment: This occurs when an electron collides with an atom to form a negative ion. Taking $SiCl_4$ as an example,

$$e + SiCl_4 \rightarrow SiCl_3^- + Cl$$

5.2.2 RIE Mechanisms

Unlike wet chemical etching, where the substrate is immersed in the etching reagent, RIE proceeds with the substrate being subjected to bombardment by ions, atoms, molecules and radicals (a radical is a fragment of a molecule with an odd number of unshared electrons). The surface of an area exposed to the plasma is removed by either physical

bombardment (sputtering) or a chemical process whereby a volatile etch product is formed or, perhaps, a combination of these two processes, with ion bombardment aiding chemical etching by locally heating the substrate and loosening the chemical bonds. Fig. 5.1 shows a diagram of two of these processes, sputtering and chemical etching [12].

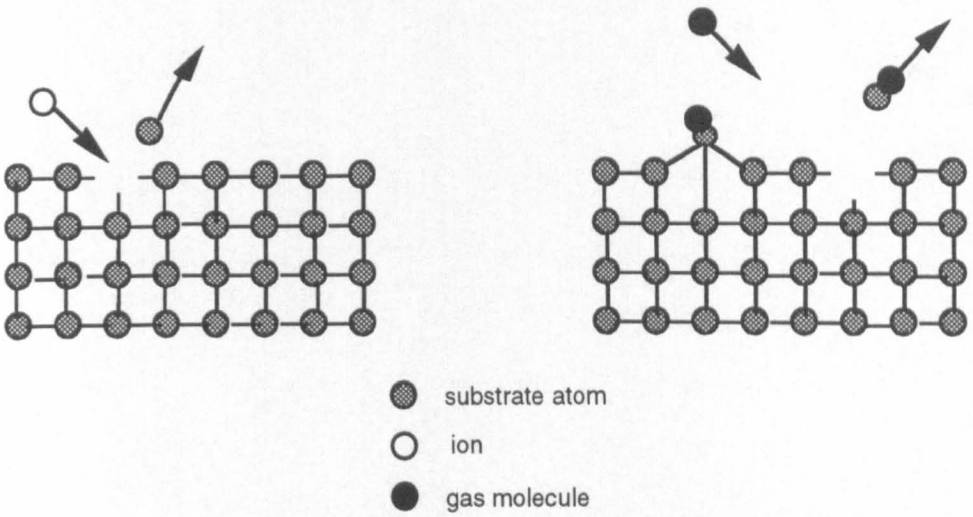

Fig. 5.1 Sputtering of substrate with ions, and chemical etching with reactive species

The basic processes involved in RIE are: generation of reactive species, transport of the reactive species to the surface of the substrate being etched, reaction with the substrate forming a volatile product and/or sputtering, transport of the product species away from the substrate and removal of the species from the chamber via the pumping process [13].

5.2.3 RIE Machine

A typical reactive ion etching machine has a vacuum chamber containing two parallel electrodes, one of which is grounded and the other of which is connected through a blocking capacitor to a radio frequency generator, as shown in Fig. 5.2.

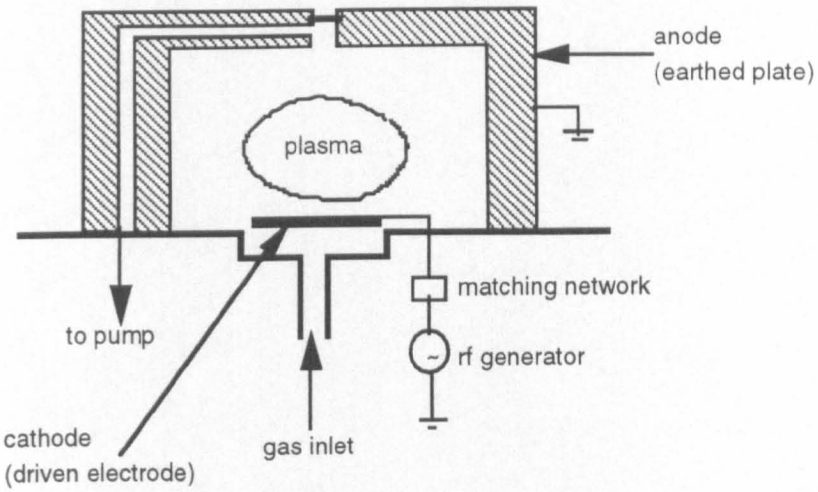

Fig. 5.2 Schematic representation of an RIE machine

Using a rf signal generator instead of using a DC power supply has two advantages: one is that the cathode can be an insulator which makes it possible for dry etching of insulators, e.g. SiO_2 and semiconductors, to be carried out; the other is that plasma can be sustained under lower chamber pressure than that required for DC plasma formation, which is desired for improving the directionality of RIE dry etching. For same reason as that of DC plasma excitation, the released electrons, due to hot cathode emission or/and ionisation by cosmic rays, are accelerated towards the anode and collide with molecules, resulting in ionisation of molecules, and thus plasma is formed. The function of the capacitor is to prevent the electrode from discharging through the power supply. Etching gases are fed into the chamber, which is maintained as a pumped evacuated environment. The response of the plasma to the positive and negative cycles is different. When the electrode is positive, many highly mobile electrons are accelerated towards the electrode causing a significant accumulation of negative charge. When the electrode is negative, heavy, immobile ions are accelerated towards it. However, only a relatively small number of ions strikes the electrode, compared to the number of electrons on the positive part of the cycle. Therefore, a high electric field region is formed around the electrode. This region is known as the plasma sheath, or the dark space, where ion acceleration occurs before bombardment of the electrode. The plasma potential is determined by the expression [14].

$$\frac{V_p - V_c}{V_p - V_a} = \left(\frac{A_a}{A_c}\right)^4 \qquad (5.1)$$

where V_a, V_c are the potentials for the electrode (cathode) and ground electrode (anode), respectively, V_p is the plasma potential, and $\frac{A_a}{A_c}$ is the ratio of the respective electrode areas which is much larger than 1. The accelerating field for the ions near the sample is, therefore, greatly enhanced since the cathode is smaller in area than the anode. If no collision occurs in the sheath regions, the average kinetic energy of singly ionised positive ions striking the cathode is $(V_p - V_c)$ eV.

The typical etch pressure used in an RIE system is relatively low (5-100 mTorr), hence the mean free path of the ions is long so they are not randomised in direction. The features such as the sample being placed on the driven electrode at the bottom, electrode asymmetry and low pressure operation all lead to an enhancement in the energy and directionality of the ion bombarding the surface being etched, thus increasing the degree of anisotropy.

5.2.4 Etching with a Methane/Hydrogen Gas Mixture

Several theories for the etching mechanism have been proposed and substantiated by some experimental evidence. The etch process is generally thought to be the reverse of the MOVPE growth process. It has been shown that the phosphine (PH_3) is the primary phosphorus-containing volatile product [9] and it is postulated that trimethyl indium is the primary indium containing volatile product. It is not easy to verify this because the methyl radical species (CH_3) is so reactive that it is difficult to detect by mass spectrometry, which tends to detect the products of reactions rather than the reactants themselves. Equations (5.2)-(5.3) show possible dissociation processes involving the etch gases and equation (5.4) shows how these gases are thought to react with the InP.

$$CH_4 \xrightarrow{e} CH_3 + H \quad (5.2)$$

$$H_2 \xrightarrow{e} 2H \quad (5.3)$$

$$3CH_3 + 3H + InP \xrightarrow{e} (CH_3)_3In + PH_3 \quad (5.4)$$

It is observed that, after CH_4/H_2 etching, there is a polymer coating on the etching mask. This polymer is thought to be an organic substance originating from the methane, as the polymer thickness increases with methane content. From the equations above, it appears that the methane is responsible for removing the indium, and the hydrogen atoms, from both the hydrogen and methane gases, for removing the phosphorus. It has been observed that, as the amount of hydrogen in the gas mixture increases, the sample surfaces become more and more depleted of phosphorus.

5.3 ET340 CH_4/H_2 Processes

5.3.1 The ET340 RIE Machine

The dry etch machine used in this research was an Electrotech SRS Plasmafab 340 RIE machine which has a 3.3 to 1 ratio of anode area to cathode area. Both electrodes are made of aluminium. The sample to be etched is placed on a titanium oxide coated cathode which has a diameter of 17 cm. The cathode (driven electrode) temperature was regulated by circulating cooling fluid which was maintained at a constant temperature of 30°C during etching.

5.3.2 ET340 CH_4/H_2 Processes

The ET340 permits control of the gas flow rate, plasma power, chamber pressure and the gas ratio. With so many parameters which can be altered, it is difficult to obtain meaningful results if more than one of the parameters are changed. Certainly, to find out

the optimum running conditions, all the parameters should be changed over a wide range in a systematic way in a great number of runs, but, in a particular run, only one parameter can be altered. Clearly, this would take an extremely long time, so, for simplicity, it was decided to start with the "standard process" which was used in the Department previously, then gradually reduce the power to as low a level as possible. The parameters of the RIE processes are summarised in table 5.1, along with the measured etch rates.

Table 5.1 The ET340 processes

Process	Gas flow rate (Sccm)		Power (W)	DC Bias (-V)	Pressure (mTorr)	Etch rate (nm/min)
	CH4	H2				
a	3.6	26	20	400	14	18
b	3.6	26	50	630	14	36
* c	3.6	26	100	850	14	50
d	7.2	52	20	430	14	28
e	7.2	52	50	556	14	72
f	7.2	52	100	760	14	96

* Process c is the " standard process " used in the Department previously.

5.4 The Etch Rates and Surface Morphology

To measure dry etch rates and examine surface morphology, 200 nm of SiO_2 was deposited on samples, whose structure similar to that shown in Fig. 4. 8. The samples were then patterned using photolithography and dry etched. The samples were etched for periods from 15 mins to 30 mins at different plasma power levels then the etch depths were measured using a depth profile meter. Fig. 5.3 shows the scanning electron micrographs of samples etched with different processes, and Fig. 5.4 shows the etching rate as a function of the plasma power. Obviously, as the forward power decrease, the surfaces become increasingly smooth, and the etch rate decreases with reduced power.

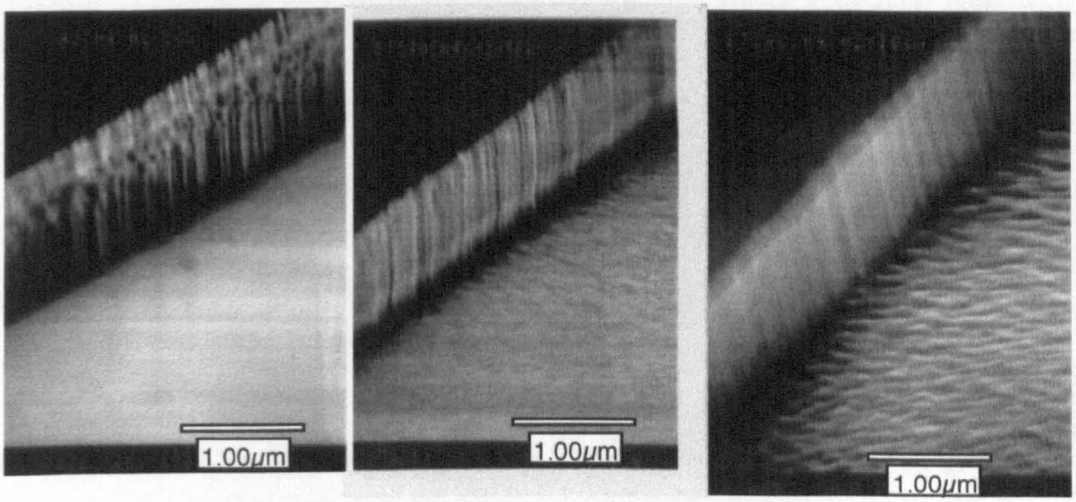

Fig. 5.3 SEM micrograph for dry etching with process (d) (left), (e) (middle) and (f) (right) in Table 5.1

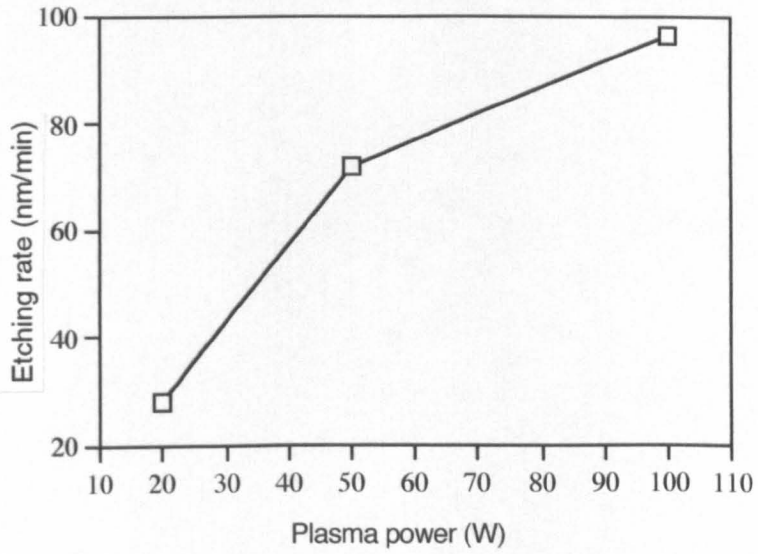

Fig. 5.4 Plot of the etch rate dependence on the plasma power

5.5 RIE Damage and Measurement Techniques

RIE damage and the quality of a semiconductor can be evaluated by studying the electrical characteristics of Schottky diodes or electrical characteristics derived from ohmic contacts

pattered and analysed using the Transmission Line Model (TLM) [15] and from Van der Pauw measurements [16]. These electrical measurement techniques are commonly used to measure surface damage. In the TLM method, a line of ohmic contacts with an increasing separation is needed. After measurement, the resistance between adjacent contacts is plotted against the separation distance. The slope and the intercept at the vertical axis of a linearly fitted line give the sheet resistance of the semiconductor layer and the ohmic contact resistance respectively. The Hall mobility and carrier concentration can be measured by Van der Pauw measurement and also by capacitance-voltage measurement. Damage to a sample will degrade the mobility of carriers due to scattering and reduce carrier concentrations. Therefore information about the quality of a semiconductor can be obtained from the carrier mobility and concentration change of the sample. $I-V$ characteristics can be measured from Schottky diodes. The Schottky contact, usually TiPtAu, is defined and the ideality factor, the Schottky barrier height, and the diode characteristics (reverse breakdown voltage and reverse leakage current) can be determined from $I-V$ measurements. The damage induced by RIE can be deduced from the decrease of barrier height and increase of the ideality factor. The main drawback of electrical measurements, however, is that they do not provide information about the damage profile and the nature or the physical extent of damage.

The main optical measurement techniques used in characterising semiconductors are Raman scattering, photoluminescence (PL) and cathodeluminescence (CL). However, only the PL measurement technique was used in this work due to the fact that PL measurement does not require any particular sample preparation, and is non-destructive.

5.5.1 The Material Probe

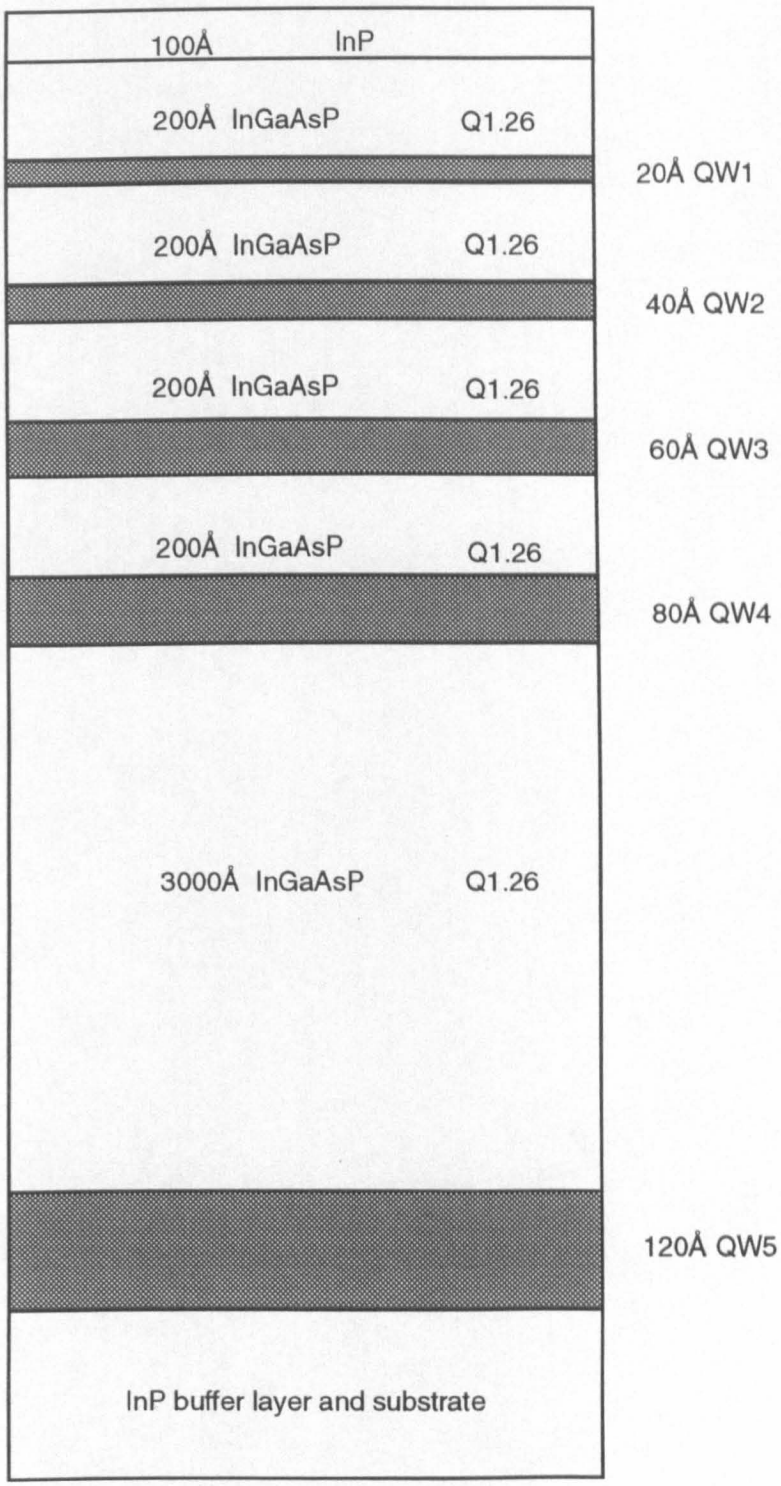

Fig. 5.5 The structure of quantum well probe material for assessment of dry etch damage

The RIE damage was probed using a specially designed structure (Fig. 5.5). The material was grown by metallorganic vapour phase epitaxy (MOVPE) on an n^+ InP substrate. Firstly a 100 nm InP buffer layer was grown, followed by 5 InGaAs quantum wells with InGaAsP barriers with a bandgap corresponding to a wavelength of λ_g=1.26 μm. The widths of the quantum wells from top to bottom were 2 nm, 4 nm, 6 nm, 8 nm, and 12 nm respectively. The top 4 wells were separated by 20 nm InGaAsP barriers, while the well of 12 nm well was placed 410 nm below the surface to provide a reference signal, this depth being well below any damage induced by the dry etching. Above the top well, 20 nm InGaAsP and a 10 nm InP cap layer were grown.

5.5.2 The Photoluminescence (PL) Experimental Set-up

The experimental PL set-up is shown in Fig. 5.6. Low temperature measurements require the sample to be placed in a cryostat and cooled with liquid-He_2. An Ar ion laser was used to photocreate electron-hole pairs which recombined radiatively by the transition of the electrons to the holes in the valence band and producing the emission of photons. The emitted radiation was dispersed by a monochromator and detected by a Ge detector. The computer was used to record and process the signals from the detector.

5.5.3 Results

Dry etching was carried out for 12 s for each of the processes shown in the table 5.1. PL was measured at 5 K. Fig. 5.7 shows the low temperature PL corresponding to different dry etch processes. The PL for an as-grown sample is also shown for comparison. It should be noted that all the PL signals have been normalised with respect to the luminescence from the deepest quantum well (QW5), this normalisation eliminates the requirement for identical sample alignment.

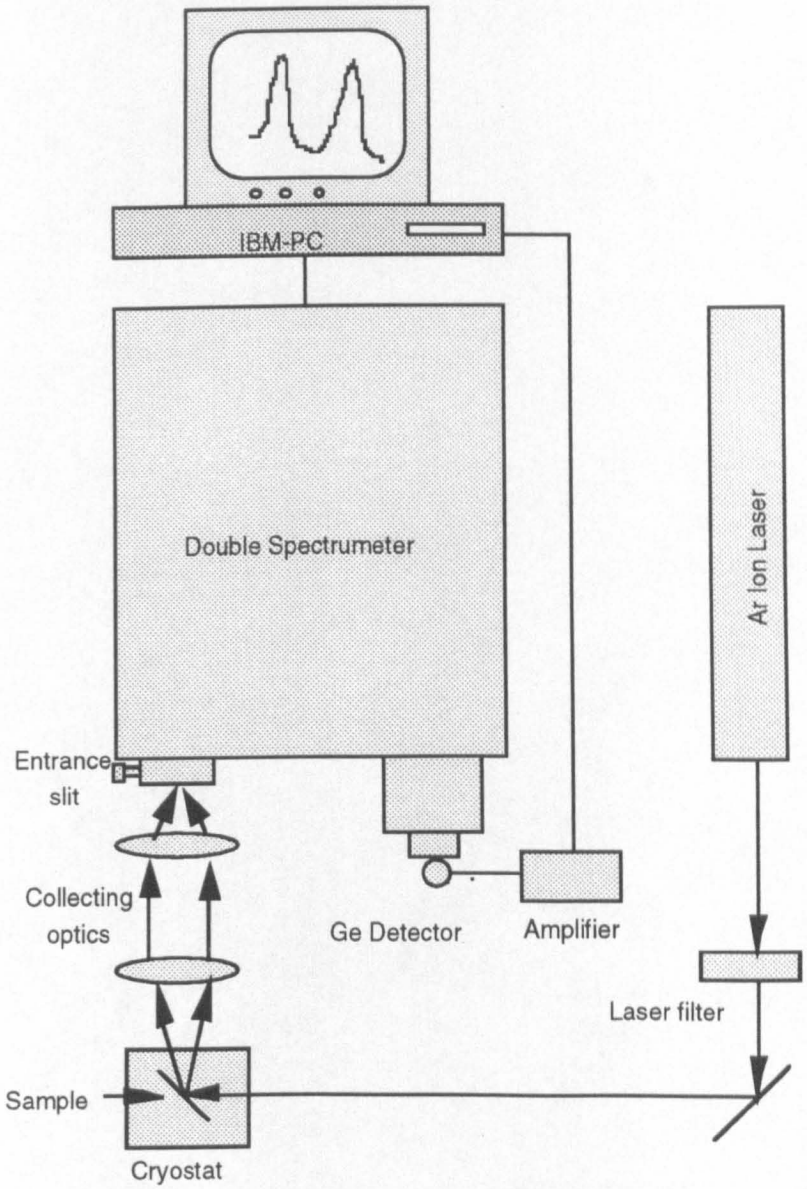

Fig. 5.6 Schematic of the PL measurement set-up

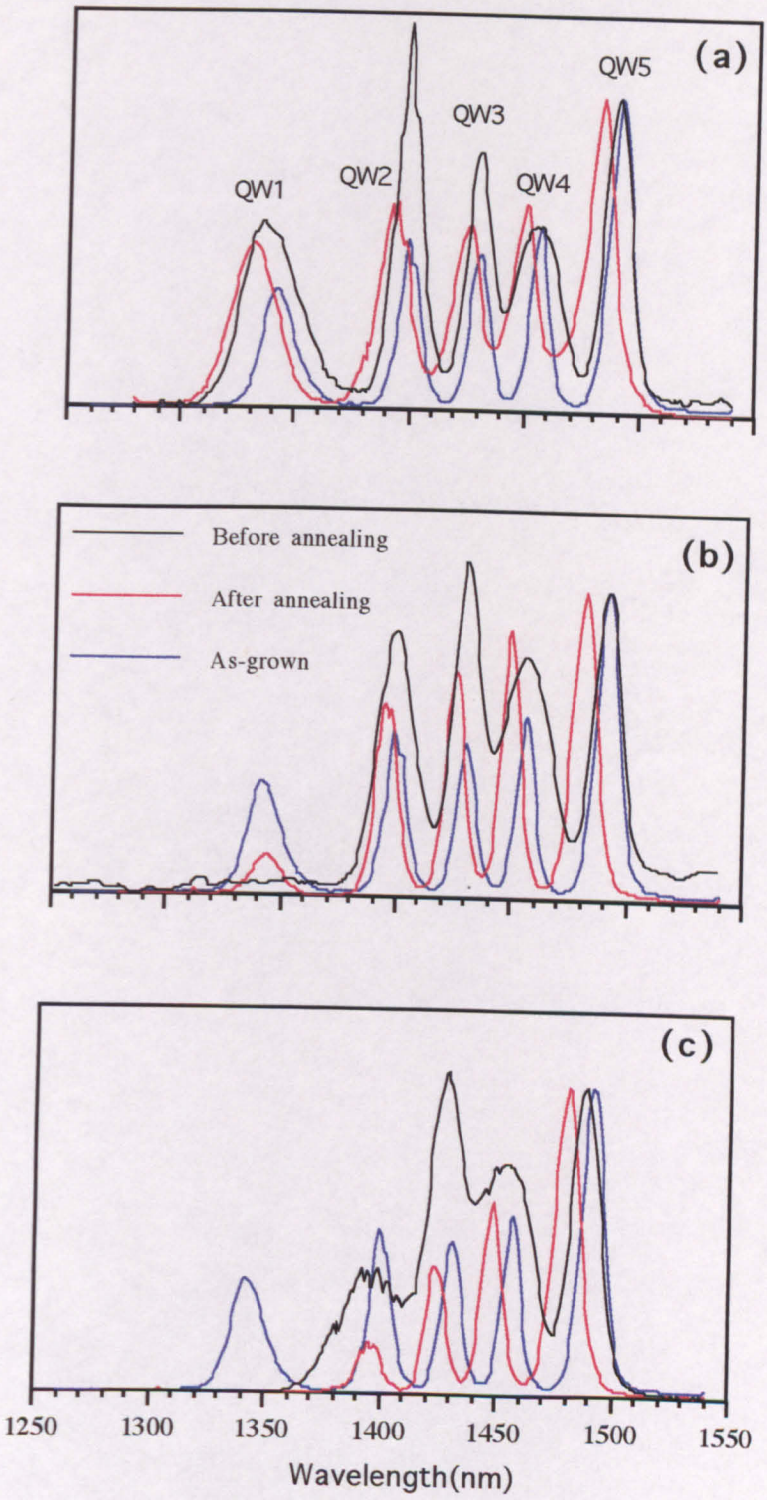
(a)
QW1
QW2
QW3
QW4
QW5
(b)
Before annealing
After annealing
As-grown
(c)
1250
1300
1350
1400
1450
1500
1550
Wavelength(nm)

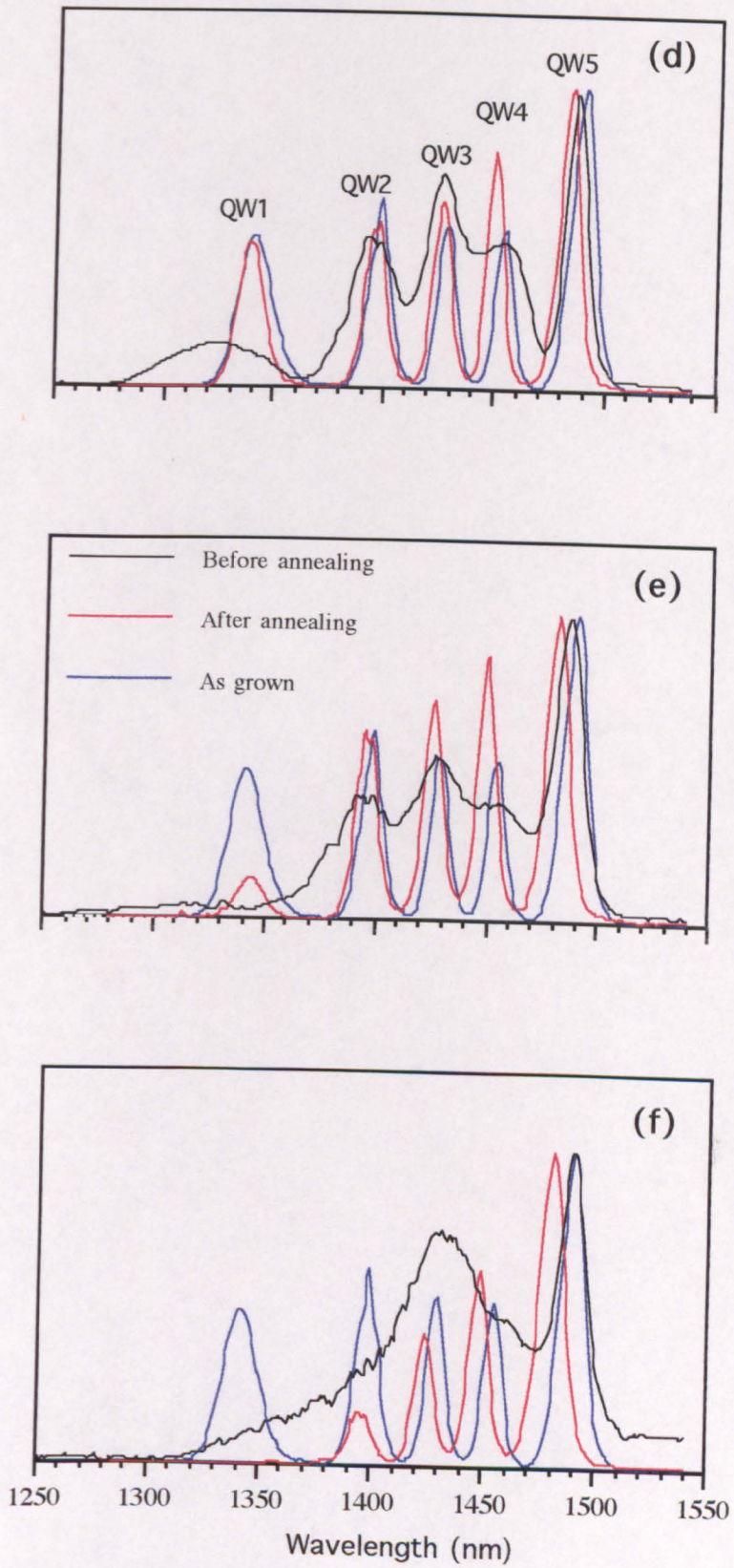

Fig. 5.7 Measured PL spectra for the samples etched using the processes shown in the Table 5.1. The figures(a)-(f) correspond to the processes (a)-(f) in table 5.1, respectively

5.5.4 Discussion

The RIE damage can be estimated by analysing the PL results shown in Fig. 5.7. For simplicity, the damage is assessed in such a way that only one parameter in the RIE conditions was changed at a time. For example, the Fig. 5.7(d)-(f) correspond to the processes in which the plasma power was varied from 20 W to 100 W, while the other parameters remained constant.

As can be seen from Fig. 5.7, the wells which have been damaged during the RIE process exhibit broadening of the PL peaks, the peaks from the different wells are no longer well resolved and the intensities are reduced substantially. Only the deepest well shows no broadening confirming that it is below the damaged region of the samples. QW1 and QW3, from which the PL signals can still be estimated in terms of peak intensity and full width half maximum (FWHM), have been chosen to characterise the damage. Fig. 5.8a shows the ratio of PL peak intensity of QW1 of the etched samples to that of the as-grown sample, as a function of rf power. When 100 W RIE power was used, no signal could be detected from QW1 after etching, even though only about 19 nm of top layer was removed by etching, leaving more than 10 nm of InGaAsP above the first well. Fig. 5.8b shows the FWHM of the PL spectrum of QW3 of the etched sample. The PL peak becomes increasingly broad with increasing plasma power. The reduction in PL intensity and the increased broadening as the plasma power increases indicates that more damage has been incorporated into the samples etched with the higher power plasma.

From Fig. 5.7, it can be seen that significant PL recovery is obtained after annealing at 625 °C for 60 s. In most cases the peak FWHM is reduced to that of the as-grown value and the peak intensity is increased. This effect may be attributed to the removal of damage, both point defects and hydrogen passivation. However, the PL intensity of the shallow wells is not recovered in all cases. For 20 W of rf power, the PL is almost the

same as that of the as-grown sample. When 50 W etch power is used, the top well is not fully recovered and in the case of 100 W etch power there is no PL signal from the top well and the PL signal from QW2 is only partially recovered, suggesting that extended defects may have been formed in this region. It should also be noted that the peaks are shifted to wavelengths shorter than those of the as-grown samples, this being due to quantum well intermixing caused by the diffusion of point defects through the wells. The blue shift increases with plasma power indicating that greater damage is introduced into the sample as the plasma power is increased.

By normalising the PL intensities of the quantum wells of the etched samples to those of the corresponding wells of the as-grown sample, the dependence of the relative intensity of PL emission as a function of the depth can be plotted (Fig. 5.9). From this dependence, it is possible to make an estimate of the damage depth. However, due to the limited number of wells in the material structure used to probe the RIE damage, and the spread of the electron and hole wavefunctions, this estimate has an error of the order of 12 nm. It should be noted that QW1 of the sample etched with 20 W of power, is assumed to be recovered completely after annealing, as its normalised PL intensity is very close to 1, hence the damage range for this plasma power should be less than the distance between the surface of the etched sample and the QW1. From Fig. 5.10, it can be seen that the estimated damage depths after annealing are around 12 nm, 27 nm, and 70 nm corresponding to the plasma power levels of 20 W, 50 W, and 100 W respectively.

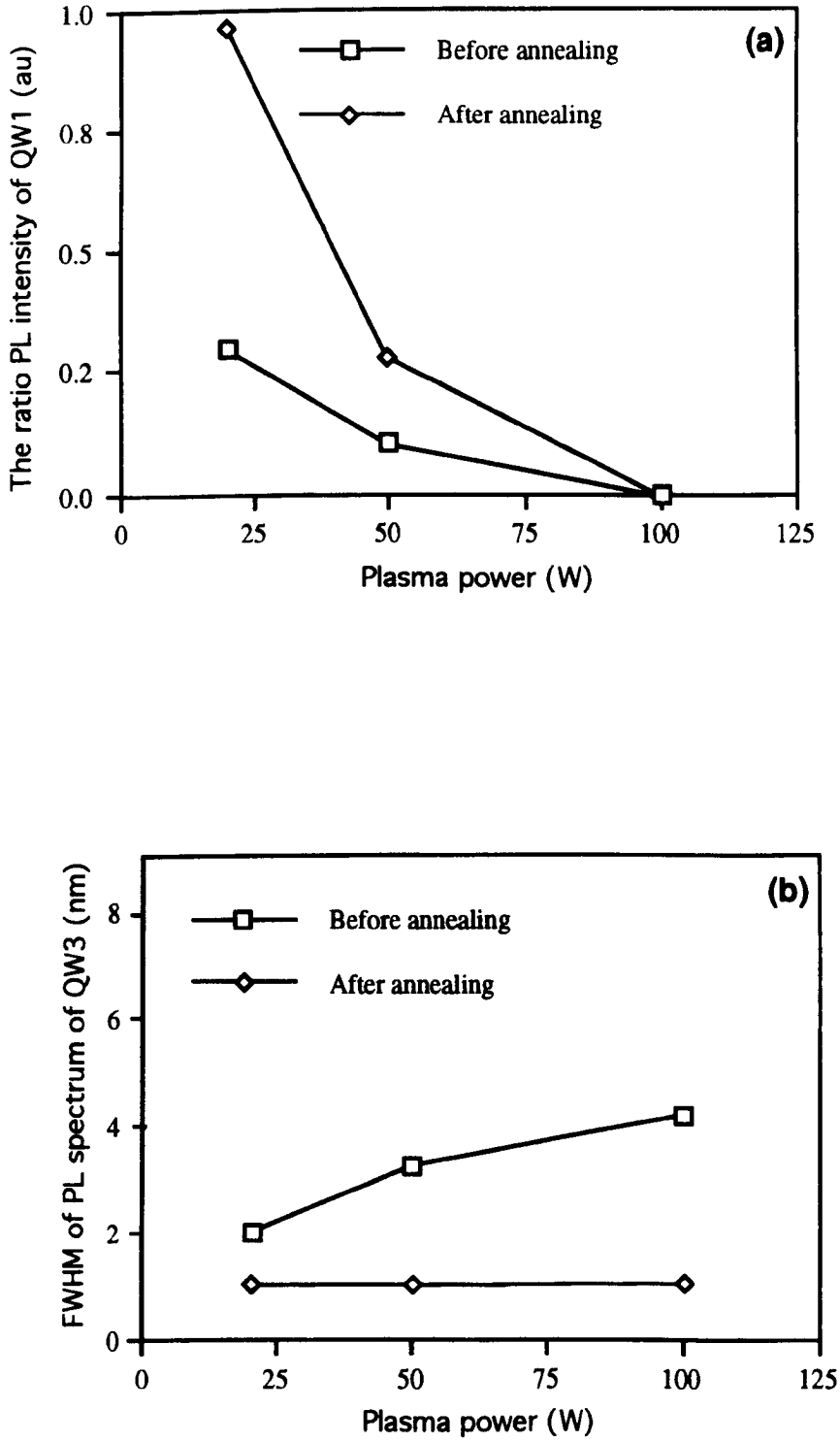

Fig. 5.8 RIE damage as function of plasma power. (a) the ratio of PL intensity of QW1 of an etched sample to that of the corresponding well of an as-grown sample, and (b) FWHM of PL spectra of QW3 normalised to that of the PL spectra of the corresponding well of an as-grown sample.

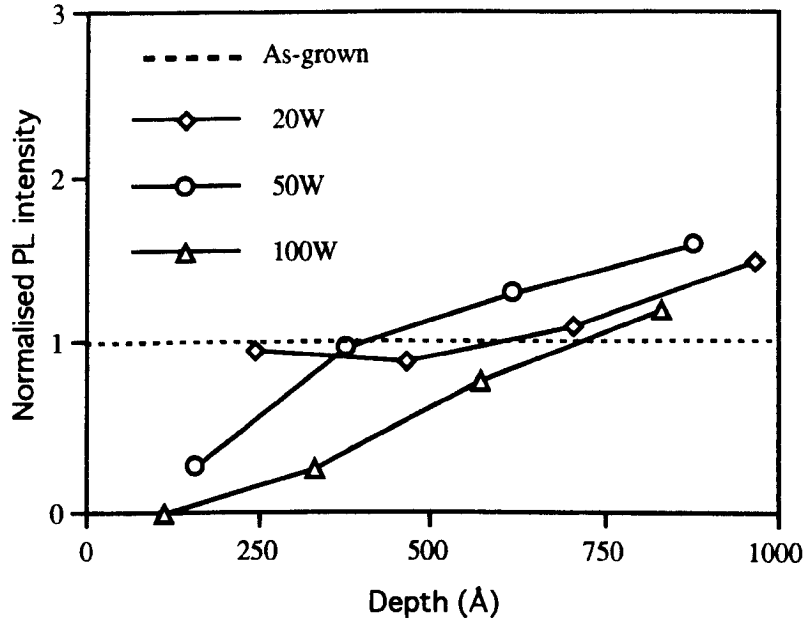

Fig. 5.9 The normalised PL intensity of the QWs as a function of depth after etching and annealing for plasma powers of 20 W (◇), 50 W (○), and 100 W (△).

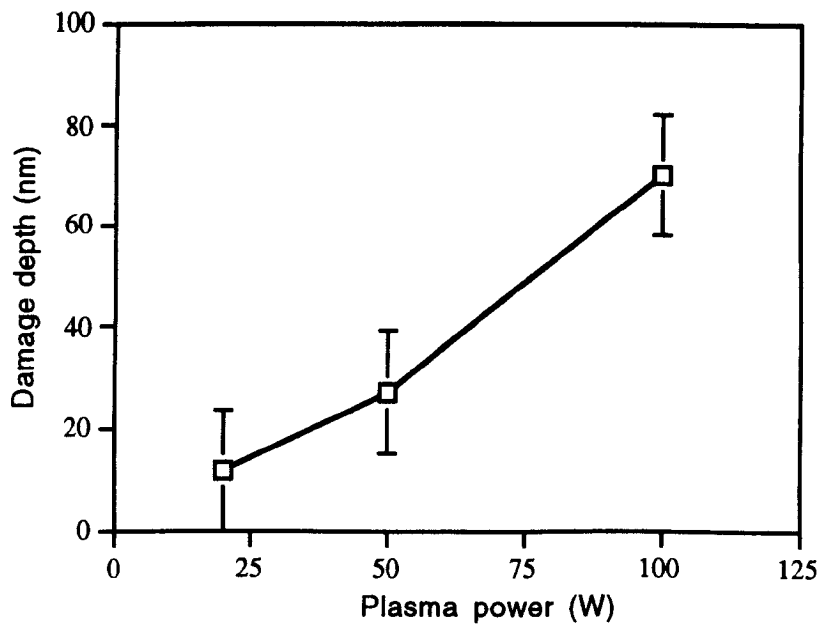

Fig. 5.10 The estimated damage depth as a function of plasma power

5.5.5 Comparison between the RIE Dry Etched Lasers and Wet Etched Lasers

5 μm wide ridge waveguide lasers were fabricated by both wet chemical etching and RIE dry etching to assess the developed RIE process in a device application. The laser material, which contained 5 InGaAs/InGaAsP QWs, was grown by MOVPE and was similar to that described in section 6.8. Process (e) in Table 5.1 was used to form the ridge waveguide, this process being chosen since it produces a relatively high etch rate with lower damage. The sample was etched for around 17 mins to give a ridge height of 1.2 μm. After etching, the sample was annealed at 500 °C for 60 s, then a routine laser fabrication procedure (see section 6.9) was followed. The light-current characteristics of groups of lasers etched by RIE and by wet etching were measured. Fig. 5.11 and Fig. 5.12 show the light-current characteristics of the lasers fabricated using dry and wet etch, respectively. It can be seen that the average threshold currents are 48.4 mA and 45.2 mA for the dry etched and wet etched lasers, respectively, and the lowest threshold currents for the dry etched and wet etched lasers being 44.5 mA and 43 mA, respectively, i.e. essentially indistinguishable given that the ridge widths are not identical. It should also be noted that the slope efficiencies of the lasers are very similar. The very close performance of the lasers suggests that the dry etch damage is small enough to have no significant effect on the laser qualities. This correlates with the results obtained when etching the QW probe sample, despite the much longer dry etch time used for the laser (17 mins), as compared to that used for the probe material (12 s).

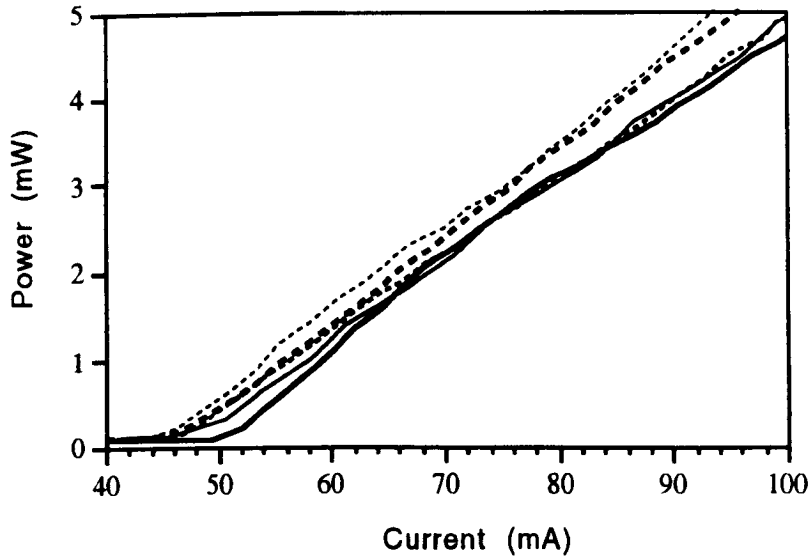

Fig. 5.11 $I - V$ curves of lasers fabricated using dry etch

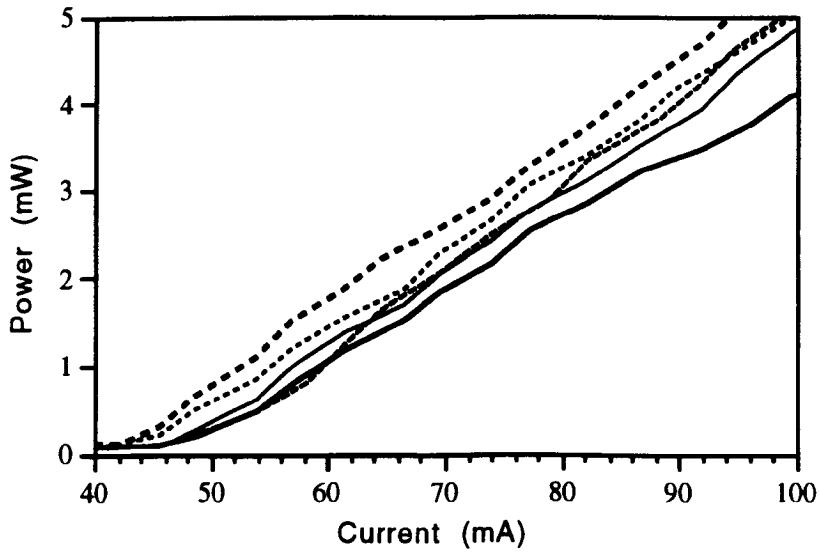

Fig. 5.12 $I - V$ curves of lasers fabricated using wet etch

5.6 Summary

By using the low temperature PL technique together with a specially designed material structure, the damage introduced by RIE CH_4/H_2 process was estimated to be in the range of 12 nm to 70 nm after annealing, for RF plasma powers in the range 20 W to 100 W. The characteristics of InGaAs/InGaAsP multi-quantum well lasers fabricated by the RIE process show that the damage does not significantly affect the laser qualities, provided a relatively low power process and post-dry-etch annealing are used.

References

1. S. Yu, T.F. Krauss, P.J.R. Laybourn, "Multiple output semiconductor ring lasers with high external quantum efficiency", IEE Proceedings-Optoelectronics, **144**, pp. 19-22, 1997

2. C. E. Zah, J. S. Osinski, C. Caneau, S. G. Menocal, L. A. Reith, J. Salzman, F. K. Shokoohi, and T.P.Lee, "Fabrication and performance of 1.5 μm GaInAsP travelling-wave laser-amplifiers with angled facets", Electron. Lett., **23**, pp. 990-992, 1987

3. E.Jahn, N.Agrawal, H.-J.Ehrke, R.Ludwig, W.Piepe, and H. G.Weber, "Monolithically integrated asymmetric mach-zehnder interferometer as a 20 Gbit/s all-optical add/drop multiplexer for OTDM systems", Electron. Lett., **32**, pp. 216-217, 1996

4. S.J. Pearton, W.S. Hobson, U.K. Chakrabarti, G.E. Derkits, and A.P. Kinsella, "Use of hydrogenated chlorofluorocarbon mixtures for reactive ion etching of In-based III-V-semiconductors", J. Vac. Sci. Technol. **B8** , pp. 1274-1284 , 1990

5. M. Moehrle, "Hydrogen passivation of Zn acceptors in InGaAs during reactive ion etching", Appl. Phys. Lett. **56**, pp. 542-544, 1990

6. T. R. Hayes, W. C. Dautremont-Smith, H. S. Luftman, and J. W. Lee, "Passivation of acceptors in InP resulting from CH_4/H_2 reactive ion etching", Appl. Phys. Lett., **55**, pp. 56-58, 1989

7. D. G. Yu, B. P. Keller, A. L. Holmes, Jr. and E. L. Hu, "Analysis of InP etched surfaces using metalorganic chemical-vapor-deposition regrown quantum-well structures", J. Vac. Sci. Technol., **B13**, pp. 2381-2385, 1995

8. E. Andideh, I. Adesida, T. Brock, C. Caneau, and V.Kermidas, "Short-period gratings for long-wavelength optical-devices", J. Vac. Sci. Technol. **B7**, pp. 1841-1845, 1989

9. T. R. Hayes, M. A. Dreisbach, P. M. Thomas, W. C. Dautremont-Smith and L. A. Heimbrook, "Reactive ion etching of InP using CH_4/H_2 mixtures - mechanisms of etching and anisotropy", J. Vac. Sci. Technol., **B7**, pp. 1130-1140, 1989

10. K. Takimoto, K. Ohnaka, and J. Shibata, "Reactive ion etching of InP with Br_2-containing gases to produce smooth, vertical walls - fabrication of etched-faceted lasers", Appl. Phys. Lett. **54**, pp. 1947-1949 , 1989

11. F. C. Chen, "Introduction to Plasma Physics", Plenum, New York, 1977

12. W.S. Ruska "Microelectronics processing", McGraw-Hill, 1987

13. A.J. Carter, B. Thomas, D.V. Morgan, J.K. Bhardwaj, A. M. Mcquarrie and M.A. Stephens , "Dry etching of GaAs and InP for optoelectronic", IEE proceddings-J, **136**, pp. 2-5, 1989

14. S. M. Sze, "VLSI Technology", 2nd ed., Mcgraw-Hill, New York, 1988

15. M.A. Foad, S. Thoms, C.D.W. Wilkinson, "New technique for dry etch damage assessment of semiconductors", J. Vac. Sci. & Technol. B, **11**, pp. 20-25, 1993

16. G. Galvagno, A. LaFerla, F. LaVia, V. Raineri, A. Gasparotto, A. Carnera, E. Rimini, "Hole mobility in aluminium implanted silicon", Semiconductor Sci. & Technol., **12**, pp.1433-1437, 1997

6. Fabrication of Ridge Waveguide Lasers Using InGaAs/InGaAsP Multiple-Quantum Well Structures

6.1 Introduction

Ridge waveguide lasers play important roles in optoelectronics, due to the fact that they have a lot of advantages over the other configurations such as wide oxide stripe lasers, such as possible single transverse mode operation, utilising the change in effective index described in chapter 4, and smaller threshold current which is attributed to the both optical and electrical confinement. Furthermore, ridge waveguide lasers can be inherently integrated with other waveguide components, and therefore offer enhanced performances and/or new device functions. For example, DBR or DFB lasers based on the incorporation of a ridge waveguide laser with gratings can be operated in a single longitudinal mode, such devices have applications in WDM communication systems in which light sources with a very narrow linewidth are of critical importance. Other examples can be found in modulators, multiplexers, and demultiplexers, devices for short pulse generation, as well as other applications.

Successful fabrication of ridge waveguide lasers is, therefore, of prime importance. In this chapter, the parameters of the InGaAs/InGaAsP multiple-quantum well materials used in this work, such as losses, gain and optical confinement are discussed. Particularly, the gain spectrum in the quantum well structure used throughout this research is addressed. The material characterisation is performed by analysing the performance of wide oxide stripe lasers fabricated from the material. Ridge waveguide lasers were fabricated using the RIE

dry etch process developed in the last chapter. Finally, the fabrication and test of ridge lasers with two contacts is also presented.

6.2 Oscillation Condition

The essential elements for a laser device, as shown in Fig. 6.1, are (i) a laser medium consisting of an appropriate collection of atoms, molecules, ions, or a semiconductor material; (ii) a pumping process to excite these atoms (molecules, etc.) into higher quantum-mechanical energy levels to achieve so-called population inversion (the population of the upper energy level is greater than that of lower energy level) to have a net gain for a beam of radiation in the medium; and (iii) suitable optical feedback elements (e.g. Fabry-Perot resonator) which allow a beam of radiation to interact repeatedly with the laser medium.

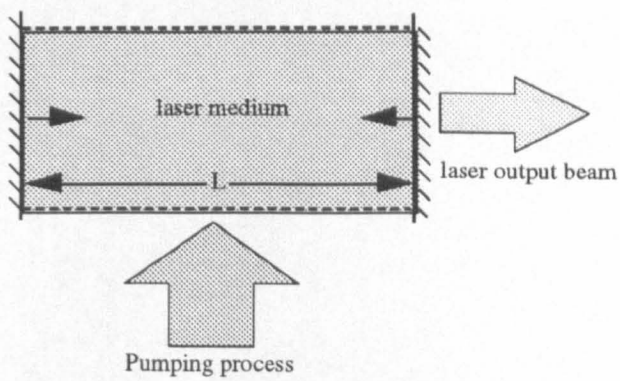

Fig. 6.1 The basic laser structure incorporating plane mirrors

Because of reflection that occurs at the Fabry-Perot surfaces, some of the photons will pass back and forth many times through the inverted population regions and be preferentially multiplied by stimulation emission. The oscillation condition is reached when

$$r_1 r_2 \exp[(g-\alpha)L]\exp(-j\frac{4\pi n}{\lambda_0}L) = 1 \qquad (6.1)$$

where, r_1, r_2 are the electric field reflection coefficients of the two facets of laser cavity, g and α are the intensity gain and loss in the cavity which will be discussed in detail later, n is refractive index of the laser cavity material, L is the cavity length, and λ_0 is the wavelength of laser emission.

The condition for oscillation given by Eq. (6.1) represents a wave making a round trip of $2L$ inside the cavity to the starting plane with the same amplitude and phase, with a multiple of 2π, The amplitude requirement is

$$r_1 r_2 \exp[(g-\alpha)L] = 1 \tag{6.2}$$

or

$$g = \alpha + \frac{1}{L}\ln(\frac{1}{r_1 r_2}) \tag{6.3}$$

The phase condition is

$$\frac{4\pi n}{\lambda_0} L = 2m\pi \qquad m=1, 2, 3... \tag{6.4}$$

The longitudinal mode spacing may be obtained by rewriting Eq.(6.4) as $m\lambda_0 = 2nL$ and differentiating to obtain

$$\lambda_0 dm + m d\lambda_0 = 2Ldn \tag{6.5}$$

For adjacent modes, dm=-1, and Eq.(6.4) can be substituted for m to give

$$d\lambda_0 = \frac{{\lambda_0}^2}{2nL[1-(\lambda_0 / n)(dn / d\lambda_0)]} \tag{6.6}$$

for the spacing between adjacent longitudinal modes.

6.3 Introduction to Semiconductor Lasers

Semiconductor lasers are important for communication and control applications because of their convenience, efficiency, and compatibility with the rest of modern electronics. Since the demonstration of semiconductor lasers in 1962 [1-4], semiconductor laser diodes have been developed from a laboratory curiosity into reliable and commercially available products. To date most laser diodes have been made in GaAs, GaAlAs, AlGaInAs, or GaInAsP, but other materials will no doubt eventually also be used extensively to obtain emission at different wavelengths, once the techniques of growth of the material and fabrication have been well developed.

The basic structure of a p-n homojunction laser diode is usually formed by epitaxial growth of a p-type layer on a n-type substrate. Ohmic contacts are made to each region to permit the flow of electrical current which is the pumping energy source required to produce an inverted population in the active region adjacent to the junction. Two parallel end facets are usually formed by cleaving to function as mirrors providing the optical feedback for the establishment of a lasing mode.

There are many problems associated with simple homostructure p-n junction lasers, which can be attributed to the fact that one is using the same material (i.e. GaAs) for both p and n regions. Two critical problems are

1. The injected minority carriers are "free" to diffuse, so diluting the spatial distribution of recombination and thus gain;
2. There is no optical confinement

both factors above contribute to the very high threshold current density, $\geq$50000 A/cm^2 [5], in homostructure lasers. To overcome the problems and reduce the high threshold current density, the heterostructure was proposed in which a material with a narrower

energy bandgap is sandwiched between two layers of materials with a wider bandgap. It is indeed fortunate that the materials with a narrow bandgap have larger refractive indices than that of materials with a wider bandgap energy. This makes it possible for the both optical and electrical confinement to be realised in the active regions simultaneously. This, in turn, reduces the threshold current density substantially. Even in early heterostructure lasers, threshold current densities were on the order of 10^3 A/cm^2 rather than 10^4 to 10^5 A/cm^2 in comparable homojunction lasers.

When the thickness of the active layer in the heterostructure lasers becomes comparable to the de Broglie wavelength ($\lambda = \frac{h}{p}$), quantum mechanical effects are expected to occur. In double heterostructure lasers with a very thin active layer, around 100 Å or less, the carrier (electron or hole) motion normal to the active layer is restricted. As a result, the kinetic energy of the carriers moving in that direction is quantized into discrete energy levels similar to the well-known quantum mechanical problem of one dimensional potential well. Double heterostructure lasers with a very thin active region or multiple thin active regions are known as quantum well lasers. The semiconductor quantum well lasers have improved performance such as lower threshold current and high differential gain, compared to double heterostructure lasers.

6.4 Optical Confinement in the Multiple Quantum Well Structure

The optical confinement factor, Γ, plays an essential role in deriving the design rules for any semiconductor laser. It depicts the overlap of the optically guided wave with the quantum well. The optical confinement factor is defined as:

$$\Gamma = \frac{\int_{-d/2}^{d/2} |E^2(z)| dz}{\int_{-\infty}^{\infty} |E^2(z)| dz} \qquad (6.7)$$

where $E(z)$ is transverse electric field distribution, and d is thickness of the active region of the quantum well structure. From its definition, optical confinement describes what fraction of the photons of the guided optical power wave interacts with the active region. When g is the volume gain per unit length of the active material, the amplification of the optical power is Γg per unit length. If α_i is the loss per unit length in the active region, then $\Gamma\alpha_i$ is the loss per unit length of a guided wave. Conversely, $1-\Gamma$ is the fraction of the power outside the active material and $(1-\Gamma)\alpha_c$ will be the loss of optical power per unit length if α_c is loss in the material outside the active region.

To calculate the optical confinement factor, the field distribution in the waveguide must be known. This, in turn, requires solution of the following equation (see Eq. (4.13)):

$$\frac{d^2E(z)}{dz^2} - [\beta^2 - n^2(z)K_0^2]E(z) = 0 \qquad (6.8)$$

where $n(z)$ is the refractive index profile in the structure. As an example, Fig. 6.2 shows the refractive index distribution for materials used in this work.

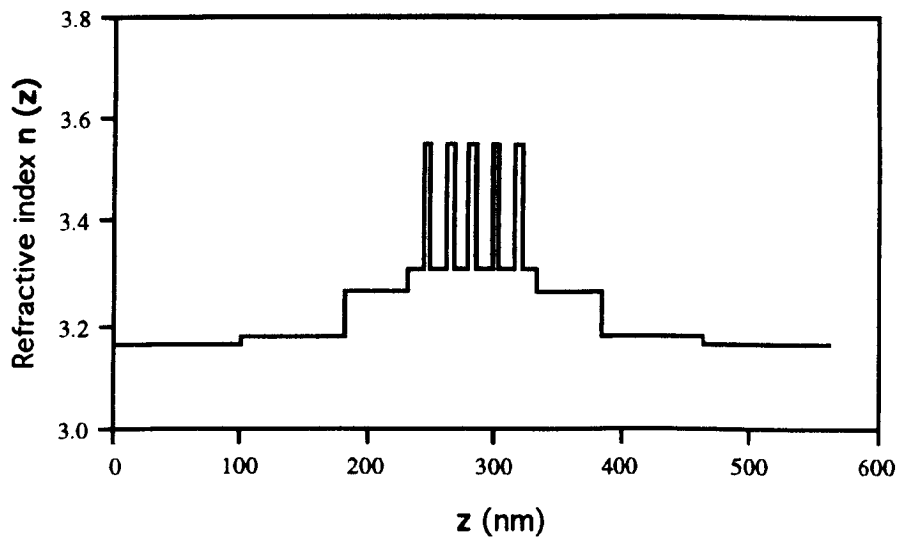

Fig. 6.2 Refractive index profile in an InGaAs-InGaAsP MQW structure

The equation (6.8) can only be solved numerically, due to the features of the refractive index profile. This can be carried out using the shooting method described in chapter 3. Fig. 6.3 shows the calculated optical power which is proportional to the square of the field intensity ($\propto |E^2(z)|$) for a typical laser structure used in this work (a well width of 50 Å).

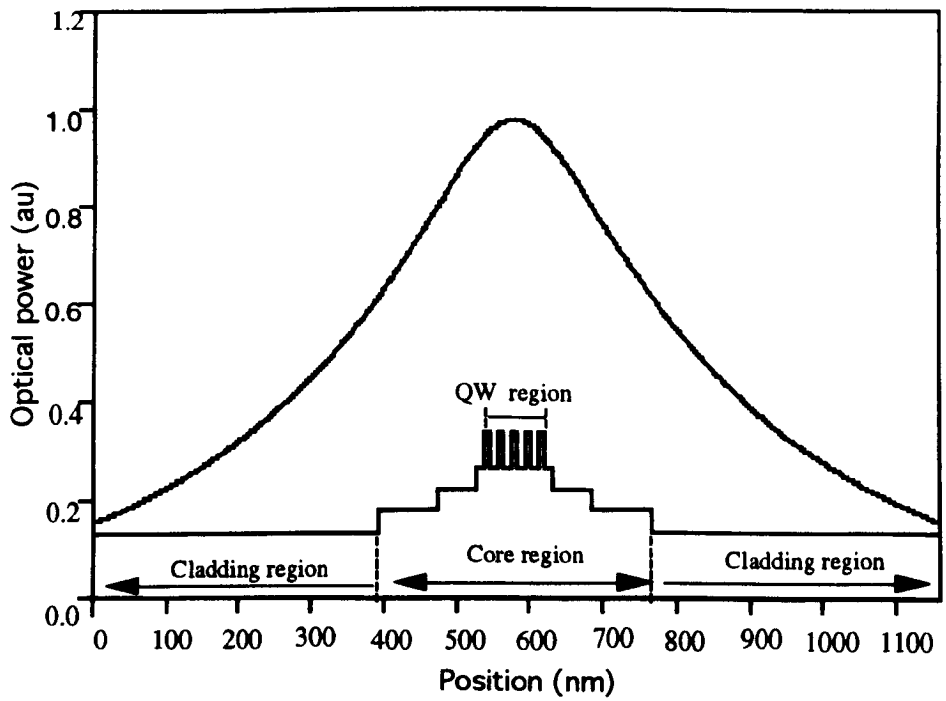

Fig. 6.3. Calculated transverse optical power distribution

From the calculated field distribution, the optical confinement factor which is the optical overlap with the wells, can be found through the following equation for this particular material structure:

$$\Gamma = \frac{\sum \int E^2(z)dz}{\int_{-\infty}^{+\infty} E^2(z)dz} \qquad (6.9)$$

where, n is the number of quantum wells in the structure, which is 5 in our case. The range of the integral in the equation covers the well region.

Fig. 6.4 shows the relationship between the optical confinement factor with the wells and well width. As can be seen from the figure, the optical confinement factor is an approximately linear function of the well width in the range of the investigation which can be expressed as

$$\Gamma_1 = 2.36\text{x}10^{-4} d \qquad (6.10)$$

where d is width of the well in Å.

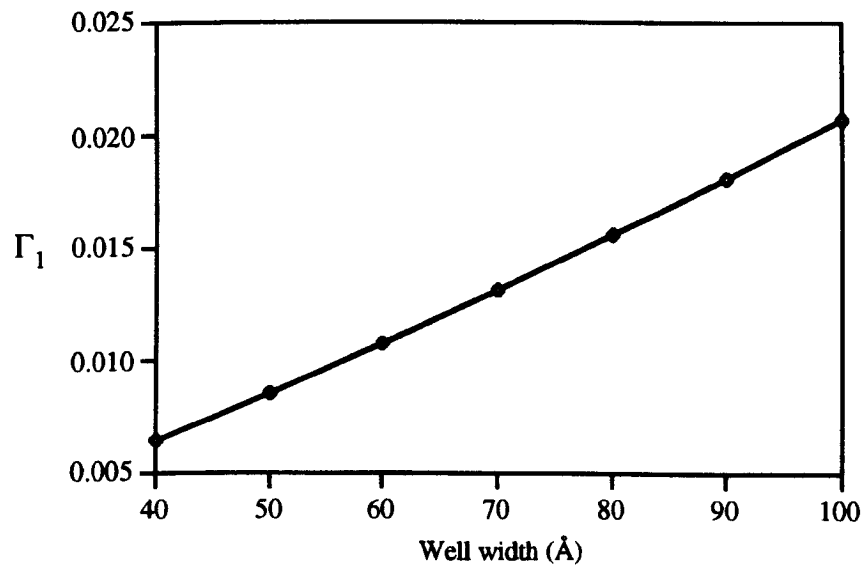

Fig. 6.4 Optical power confinement in the region of wells as function of the well width

The factor of optical confinement in the waveguide core, Γ_2, which is the ratio of the overlap of optical power distribution with the waveguide core region to the total optical power, can also be found in the same fashion, and is shown in Fig. 6.5.

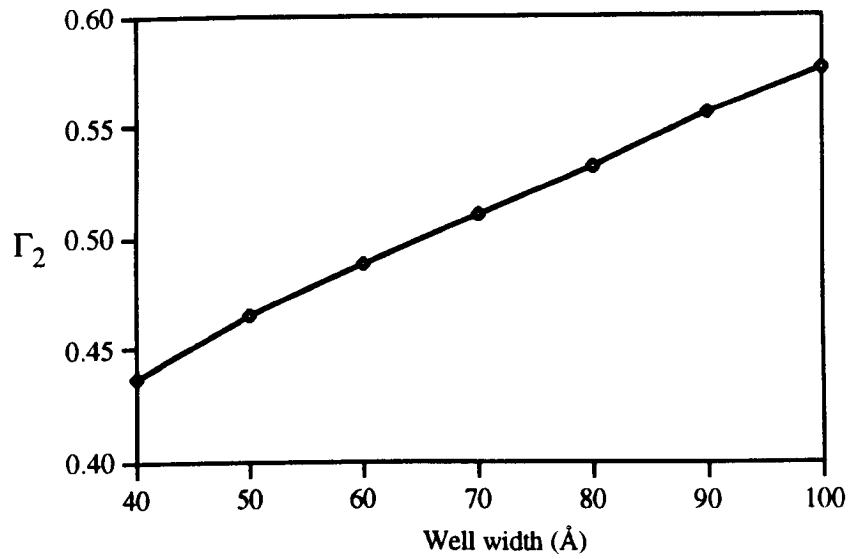

Fig. 6.5 Optical power confinement in the waveguide core region as function of the well width

From the calculation, we can conclude that the optical confinement in the quantum well region is quite weak, between 0.96% - 2.36% for each well for well thickness range from 40 Å - 100 Å. Also we can see that around half of the optical power extends into the cladding layers of the structure.

6.5 Losses in a Multiple Quantum Well Material

The loss in an MQW laser is due to a combination of free-carrier absorption in the cladding layer, bulk absorption within the active regions and scattering of surfaces and interfaces. This can be described as [5]

$$\alpha_i = \Gamma\alpha_{fc} + (1-\Gamma)\alpha_{pg} + \alpha_{sc} \qquad (6.11)$$

where α_{fc} is the loss in the active QW layers, α_{pg} is the loss in passive portions of guide and in the cladding, and α_{sc}, the losses due to the scattering. We know that the optical field extends from the waveguide core region to the doped cladding regions, because of the small optical confinement factor. Free carrier absorption is crucial in semiconductor lasers because it is a major unavoidable loss mechanism. It results from the scattering of carriers

in motion and is therefore influenced by the same scattering mechanisms that influence carrier mobility. A summary of the expressions for free carrier absorption due to various scattering mechanisms has been given by Fan [6]. It is convenient to express α_{fc} in term of the photon capture cross section for holes,

$$\sigma_p = \frac{\alpha_p}{p} \tag{6.12}$$

and capture cross section for electrons

$$\sigma_n = \frac{\alpha_n}{n} \tag{6.13}$$

Various published data [7-10] show that the free carrier loss varies linearly with the carrier concentration.

Another important loss is scattering loss, which is due to scattering of radiation out of optical waveguide by either nonplanar heterostructure interfaces or imperfections in the dielectric layers, and also by etched surfaces and rib sidewalls.

6.6 Nonradiative Recombination

An electron-hole pair can recombine nonradiatively, meaning that the recombination can occur through any process that does not emit a photon. The effect of nonradiative recombination is to increase the threshold current. If τ_{nr} is the carrier lifetime associated with nonradiative processes, the increase in threshold current density is given approximately by

$$J_{nr} = \frac{en_{th}d}{\tau_{nr}} \tag{6.14}$$

where n_{th} is the carrier density at threshold, d is the active layer thickness, and e is the electron charge.

It is generally believed that the Auger effect plays a significant role in determining the observed high temperature sensitivity of the threshold current of InGaAsP lasers emitting near 1.3-1.55 μm [11-16]. The active region of an InGaAsP MQW laser is normally undoped. Under high injection the Auger rate varies approximately as

$$R_A = Cn^3 \tag{6.15}$$

and the current lost to Auger recombination at threshold current density is given by

$$J_A = edCn^3 \tag{6.16}$$

The Auger recombination rate C in QW structure has been calculated [14, 15]. The value for a $\lambda \approx 1.3$ μm InGaAsP QW is around 3 x 10^{29} cm^6 sec^{-1}, which is close to the measured value. The Auger life time is given by

$$\tau = \frac{n}{R_A} = \frac{1}{Cn^2} \tag{6.17}$$

6.7 Gain

The gain equation is calculated from the radiative recombination rate as obtained from standard perturbation theory in solids. The spectral gain curve can be written as[17]

$$g(E_i) = \frac{2\pi\hbar e^2}{n\varepsilon_0 m_0^2 c E_i} \int_{E_g+E_{cn}+E_{vn}}^{\infty} M^2(E)\rho_r[f_{cn}(E) - f_{vn}(E)]L(E - E_i)dE \tag{6.18}$$

where $\hbar = h/2\pi$, h is Planck's constant, n is the refractive index, e is the electron charge, ε_0 is the permittivity of free space, m_0 is the electron rest mass, c is the velocity of light in vacuum. E_{cn}, E_{vn}, related to the bottom of the potential well in the conduction and valence bands for the electrons and the holes respectively, are the quantized energies for electrons and holes respectively. E_g is the bandgap of the well corresponding to the bulk material, $E_i = \hbar\omega$ is energy of the photons, ρ_r is the reduced electron and hole density of states, M is the interband matrix element which is given by [17]

$$M_{hh}^2(E) = \frac{3}{4} M_{DH}^2 [1 + \frac{E_{cn}}{E_{cn} + \frac{m_v}{m_c + m_v}(E - E_g - E_{cn} - E_{vn})}] \tag{6.19}$$

and

$$M_{DH}^2 = \frac{m_0^2 E_g (E_g + \Delta)}{12 m_c (E_g + \frac{2}{3}\Delta)} \tag{6.20}$$

where Δ is the valence band split-off energy.

f_{cn}, f_{vn} are the Fermi-Dirac distribution functions in the conduction and valence band, respectively, which can be written as

$$f_{cn}(E) = \frac{1}{1 + \exp[E_{cn} + \frac{m_v}{m_c + m_v}(E - E_g - E_{cn} - E_{vn}) - E_{fc}]/kT} \tag{6.21}$$

and

$$f_{vn}(E) = \frac{1}{1 + \exp\{-[E_{vn} + \frac{m_v}{m_c + m_v}(E - E_g - E_{cn} - E_{vn}) - E_{fv}]/kT\}} \tag{6.22}$$

E_{fc}, E_{fv} are the quasi Fermi levels which are related to the carrier density through the following equations:

$$N = N_{QW} + N_{ub} \tag{6.23}$$

$$N_{QW} = \frac{4\pi m_c}{L_z h^2} \sum_n \int_{Ecn}^{\Delta E_c} \frac{1}{[1+\exp(\varepsilon_{cn} - E_{fc})/kT]} d\varepsilon_{cn} \qquad (6.24)$$

$$N_{ub} = \frac{4}{\sqrt{\pi}} \left(\frac{2\pi m_c}{h^2} \right)^{3/2} \int_{\Delta E_c}^{\infty} \frac{\sqrt{\varepsilon_{cn}}}{[1+\exp(\varepsilon_{cn} - E_{fc})/kT]} d\varepsilon_{cn} \qquad (6.25)$$

Where ΔE_c is the depth of the conduction band potential well, n is the number of the energy levels in the quantum well. Similar equations can be obtained for the holes. For a given carrier density, the quasi Fermi energies E_{fc} and E_{fv} which are with reference to the bottom of the quantum wells in the conduction and valence bands, respectively, can be found using equations (6.23-6.25).

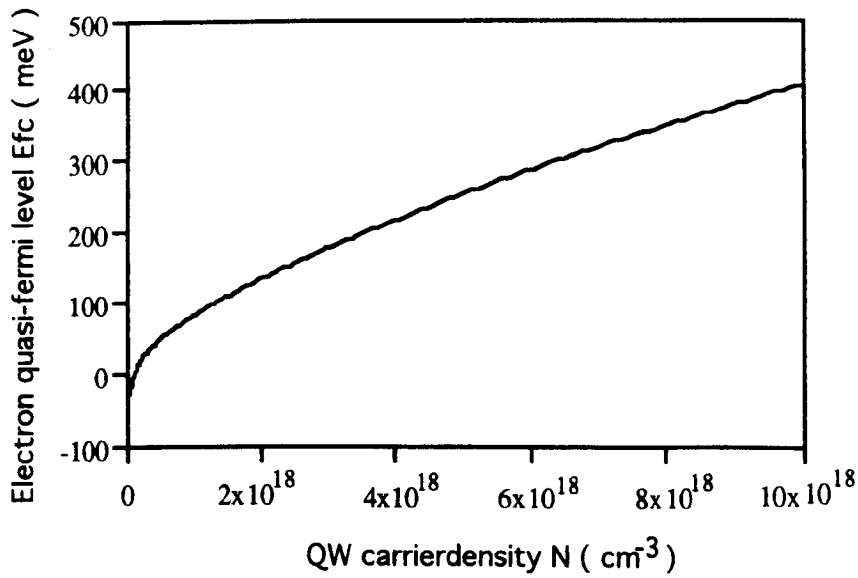

Fig. 6.6 Quasi Fermi level in conduction band

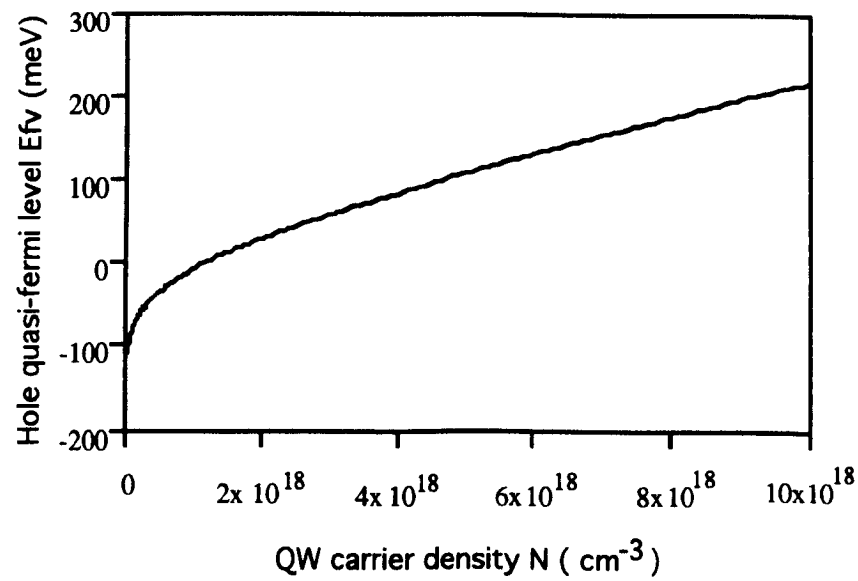

Fig. 6.7 Quasi Fermi level in valence band

Fig. 6.6 and Fig. 6.7 show the dependence of the quasi Fermi levels, E_{fc} and E_{fv}, in an $In_{0.53}Ga_{0.47}As$-InGaAsP quantum well of 80 Å (see Fig. 2.5) on the injection carrier concentration. It can be seen from Fig. 6.6 and Fig. 6.7 that to raise the valence band quasi Fermi level requires much more injected carrier density than that required for raising the conduction band quasi Fermi level. This is directly associated with the fact that the effective mass of the heavy holes is approximately an order of magnitude larger than that of the electrons.

It should be noted that the effect of the light hole is not taken into account in the Eq. (6.18). Assuming that the K-selection role is valid [18-20], the intraband relaxation can be described by the Lorentzian function:

$$L(E) = \frac{1}{\pi} \frac{\frac{\hbar}{\tau_{in}}}{E^2 + \left(\frac{\hbar}{\tau_{in}}\right)^2} \tag{6.26}$$

where τ_{in} is the intraband relaxation time which is typically about 0.1 ps. This corresponds to an energy spread of full-width-half-maximum around 13.2 meV at a wavelength of 1.55 μm.

For a given carrier density, or injection current density, the Fermi energy level can be determined as described previously, and the gain spectrum can be obtained by integrating equation (6.18). For simplicity, in the following calculation, only the transition from the ground level will be considered, because the transition from the ground level accounts for most of the gain. Furthermore, the transitions from higher levels make no contribution to the maximum gain. By integrating Eq. (6.18) numerically, gain spectra, with and without taking the Lorentzian lineshape (Eq. 6.26) into account, can be obtained.

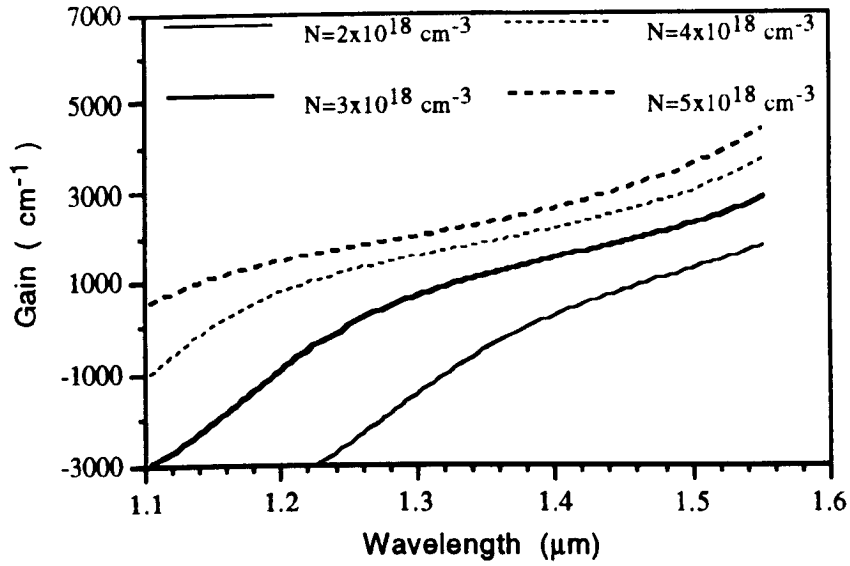

Fig. 6.8 Calculated gain spectra of the InGaAs-InGaAsP well structure (Sheffield material structure) without considering the Lorentzian spread for an emission wavelength of 1.55 μm. The parameter indicated is the carrier concentration.

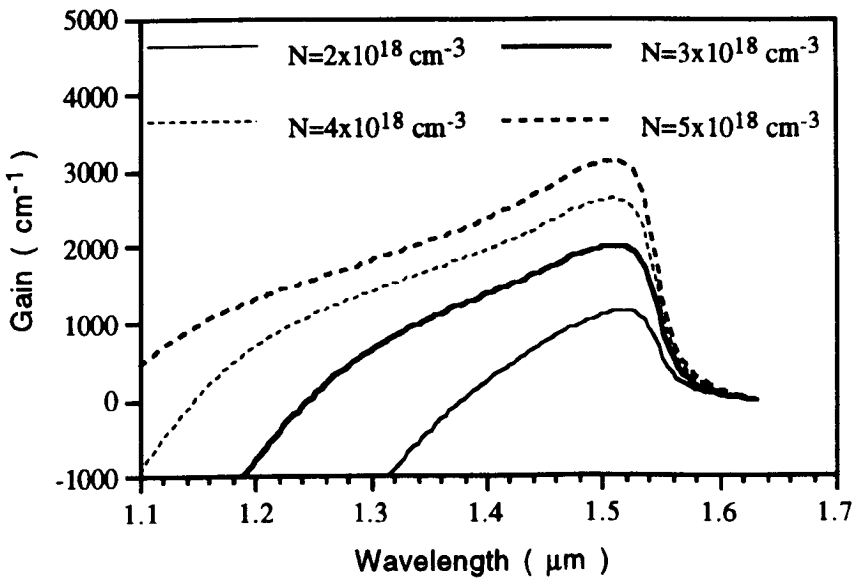

Fig. 6.9 Calculated gain spectra of the InGaAs-InGaAsP well structure (Sheffield material structure) taking the Lorentzian spread into account with τ_{in}=0.1 ps for an emission wavelength of 1.55 μm. The parameter indicated is the carrier concentration.

The gain spectra, with and without taking the Lorentzian spread into account, for an InGaAs/InGaAsP quantum well are shown in Fig. 6.8 and Fig. 6.9, respectively. As can be seen from the figures, the maximum gain always occurs at the wavelength of 1.55 μm for the spectra without considering the Lorentzian effect. However, the maximum shifts to shorter wavelength with increasing carrier concentration when the Lorentzian lineshape effect is included (Fig. 6.10). From Fig. 6.10, it can also be seen that the gain peak wavelength remains constant when the carrier density is greater than about 2.3×10^{18} cm^{-1}, this may be due to the fact that only the transition from the ground level was considered, while the contribution from the other energy levels as well as transition between the conduction band and the light hole band were neglected during the calculation of the gain spectrum above. Comparing Fig. 6.8 to Fig. 6.9, it is clear that the effect of the Lorentzian spread on the spectra is that it compresses the gain and broadens the spectra at peak wavelength range. From the figures, the relation between the maximum gain and the carrier density can be established as shown in Fig. 6.11. Fig. 6.12 is the plot of maximum gain versus the logarithm of carrier density, resulting in an approximately straight line.

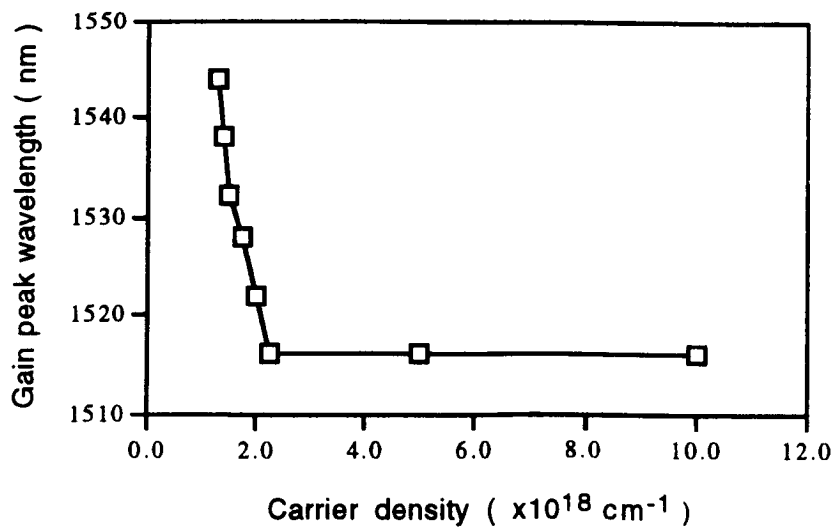

Fig. 6.10 Gain peak wavelength against carrier density

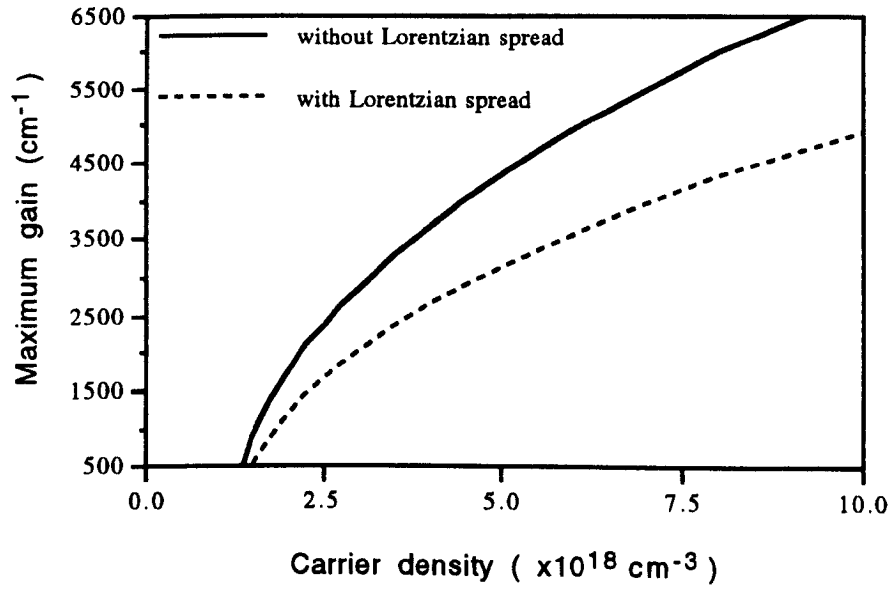

Fig. 6.11 Carrier density dependence of maximum gain. (Calculated for the Sheffield material structure.)

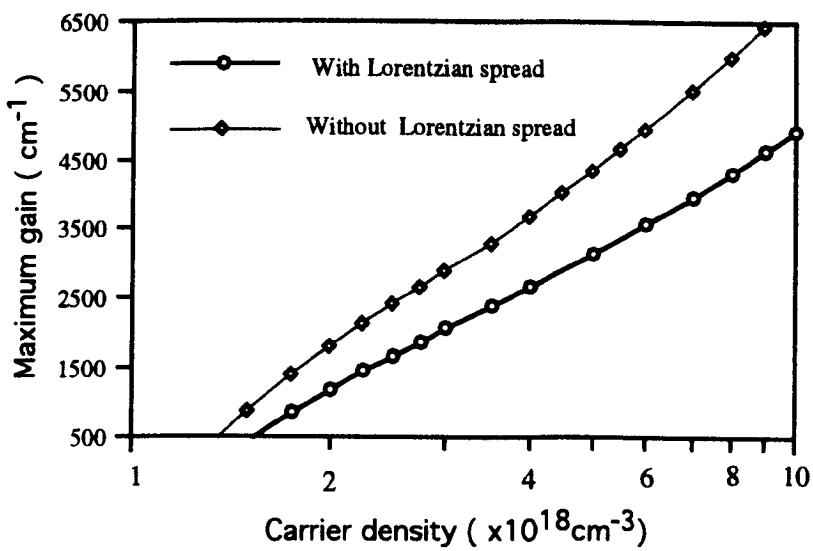

Fig. 6.12 Maximum gain as function of carrier density (in log scale). (Calculated for the Sheffield material structure.)

6.8 Material Characterisation

The structure of the material used to fabricate lasers was grown by metal organic vapour phase epitaxy (MOVPE) on an (100)-oriented n -type InP substrate and consisted of five 65 Å InGaAs wells with 120 Å InGaAsP barriers (λ_g=1.26 μm, where λ_g is the wavelength corresponding to the bandgap). The active region was bounded by a stepped graded index (GRIN) waveguide core consisting of InGaAsP confining layers. The thicknesses and compositions of these layers (from the QWs outward) were 500 Å of λ_g=1.18 μm and 800 Å of λ_g=1.05 μm (λ_g is the wavelength corresponding to the bandgap of the different layers). The structure, which was lattice matched to InP throughout, was completed by an InP cladding layer and an InGaAs contact layer. The first 0.2 μm of upper cladding layer was an undoped spacer layer and the remaining 1.2 μm was doped with Zn to a concentration of 7.0E+17 cm^{-3}. The lower cladding layer was Si doped to a concentration of 5.0E+18 cm^{-3}. The waveguide core was undoped, thus forming a *pin* structure with the intrinsic region restricted to the QWs and GRIN layers.

In order to assess wafers, 75 μm wide oxide stripe lasers were fabricated. The fabrication of the lasers is relatively simple. The cleaned samples were coated with a layer of 200 nm of SiO_2. The 75 μm stripe windows were defined using photolithography and wet etching with buffered HF solution (HF:H_2O_1=1:4). These lasers are gain-guided since the injected current produces population inversion and only photons which remain within the pumped region can cause stimulated emission. The samples were then thinned to a thickness of around 140 μm and metal contacts were evaporated using a computer controlled metal evaporator ('Plassys'). The samples were then annealed in an RTA at 360 °C for 60 s and cleaved into individual lasers with cavity lengths of 400, 600, 800 and 1000 μm. A diagram of an oxide stripe laser is given in Fig. 6.13.

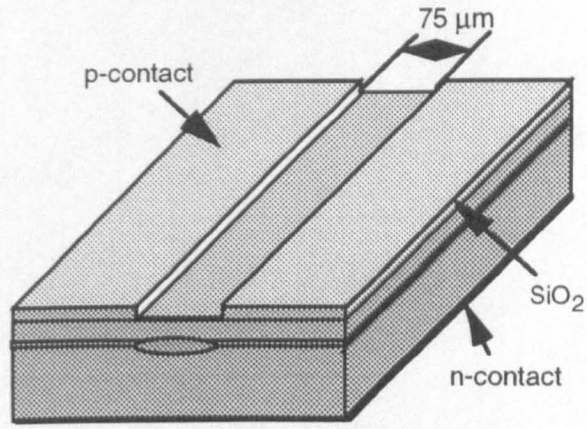

Fig. 6.13 Schematic diagram of a 75 μm wide oxide stripe laser

6.8.1 Laser Test

Fig. 6.14 shows the experimental set-up used to test lasers. The current supply was an Avtech pulsed current generator which has an adjustable pulse width and repetition rate. The pulse generator can be controlled manually or automatically. A variable attenuator was used to adjust the magnitude of the pulses from the pulse generator. The pulse transformer in the set-up was for the purpose of impedance matching. The driving current to the laser being tested was applied through the circuit shown in Fig. 6.15. The voltages across the laser diode and the 1 Ω resistor were measured, and from the latter, the current through the laser was calculated.

Laser power was measured by a germanium photodetector which was reverse biased at 4.5 V. The voltage across the resistor in series with the detector was linearly proportional to the light emitted by the laser. A boxcar averager monitored the current through the laser diode, the voltage across the laser, and the laser output light. It averaged the measurements over 100 cycles which enhanced the ratio of the the signals to noise. These signals were then transferred to the computer, which then calculated the current through the laser, the voltage across the device, and the output power from the device. The output of the boxcar

was also monitored by an oscilloscope which displayed the current through the laser and the laser output.

The lasers were operated in pulsed current mode at room temperature. The current pulse length was 400 ns and the repetition rate was 1 kHz (duty cycle 1:2500). Light-current ($L-I$) characteristics and spectra were measured for lasers of each length cleaved. For each length a group of about 5 lasers were tested. Only the best data (lowest threshold current and the best efficiency) were selected for analysis. Fig. 6.16 shows $L-I$ curves for different cavity lengths. From the measured $L-I$ data, the threshold current can be found.

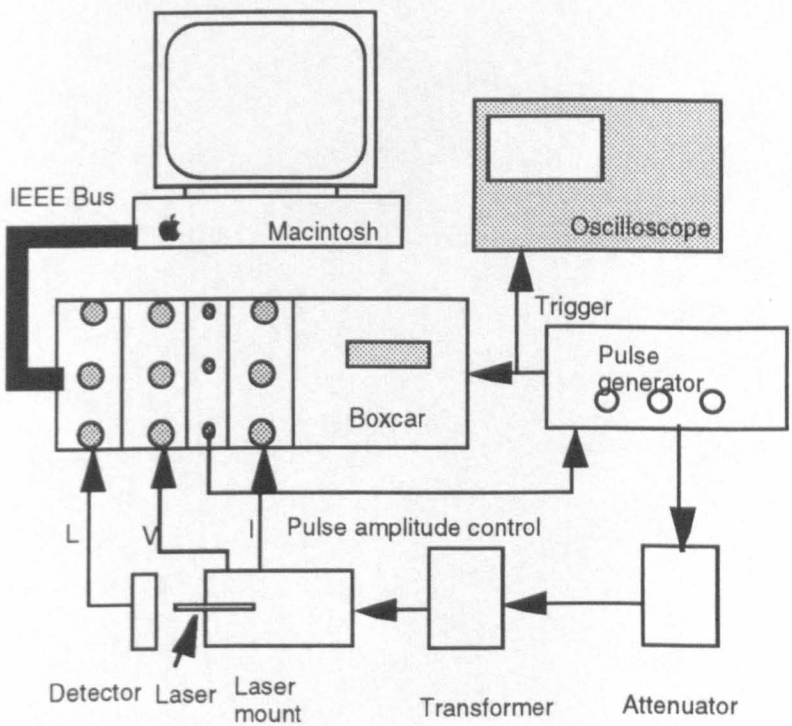

Fig. 6.14 Experimental set-up

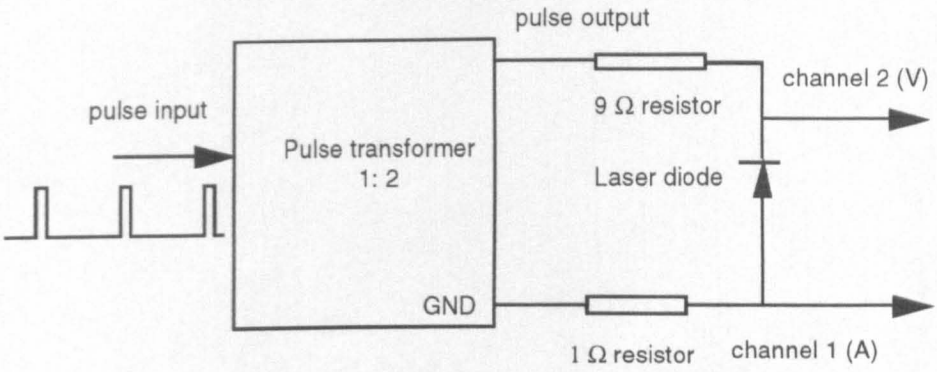

Fig. 6.15 Laser test circuit

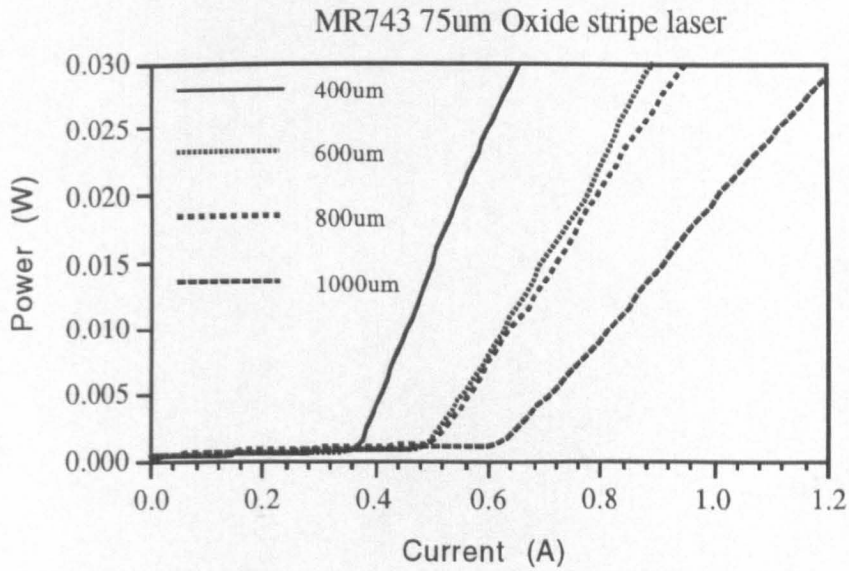

Fig. 6.16 Measured *L-I* curves for lasers with different cavity length

The external quantum efficiency η_e, which is defined as the number of emitted photons from both end facets of laser for one injected electron, was found from the slope of the $L-I$ curve above threshold current multiplied by a factor of $\lambda_0/1.24$, where, λ_0 is the operation wavelength of the laser in μm. Table 6.1 shows the data calculated from the $L-I$ data. It should be noted that the external quantum efficiency, η_e, shown in table 6.1 is multiplied by a factor of 2 because the detector only collected the output light from one end facet in our experimental set-up. Here we assume that the output light from the both facets is identical.

Table 6.1 The measured data of 75μm oxide stripe lasers

L (Cm)	η_e(photon/elctron)	Ith(A)
0.04	0.255	0.38
0.06	0.180	0.47
0.08	0.163	0.51
0.10	0.123	0.61

6.8.2 The Material Characterisation

The material parameters such as internal quantum efficiency, the loss etc. can be determined by analysing the data shown in table 6.1 using the following approach. As we know, laser oscillation occurs when the gain is equal to the total loss in the laser cavity. The gain required at threshold, g_{th}, of a quantum well (QW) semiconductor is given by

$$g_{th} = \alpha + \frac{1}{L}\ln(\frac{1}{R}) \tag{6.27}$$

where α is the loss coefficient, L is the cavity length, and R is the reflectivity of the end facets. Above the threshold the laser action is initialised under a constant g_{th} and the extra injected carriers recombine and emit light. The relationship between g_{th} and the external quantum efficiency is given by

$$\eta_e = \eta_i(1 - \frac{\alpha}{g_{th}}) \tag{6.28}$$

where η_i is the internal quantum efficiency which is defined as the probability that an injected carrier recombines radiatively in the active region.

As can be seen from Fig. 6.12, the gain is approximately a linear function of the logarithm of carrier density, so the gain above threshold is related to the current density in a QW laser by the following relationship:

$$g(J) = n\Gamma g_0 \ln(\frac{\eta_i J}{nJ_t}) \tag{6.29}$$

where n is the number of quantum wells, Γ is optical confinement per well, g_0 is the gain coefficient for one well and J_t is the transparency current. From Eq. (6.27) and (6.28), we can obtain the following relationship:

$$\frac{1}{\eta_e} = \frac{1}{\eta_i} - L(\frac{\alpha}{\eta_i \ln R}) \tag{6.30}$$

Therefore η_i can be obtained from the intercept of a linearly fitted plot of $\frac{1}{\eta_e}$ against the cavity length, L. By assuming a reflectivity R=30% for a cleaved facet, the optical loss α can also be determined. From equation (6.29), the gain coefficient at threshold will be :

$$g_{th} = n\Gamma g_0 \ln(\frac{\eta_i J_{th}}{nJ_t}) \tag{6.31}$$

where J_{th} is the threshold current density. By substituting equation (6.27) into (6.31), and rearranging the equation, we have

$$\ln(J_{th}) = [\frac{\alpha}{n\Gamma g_0} + \ln(\frac{nJ_t}{\eta_i})] - \frac{1}{L}(\frac{\ln R}{n\Gamma g_0}) \tag{6.32}$$

Defining

$$\ln(J_0) = [\frac{\alpha}{n\Gamma g_0} + \ln(\frac{nJ_t}{\eta_i})] \tag{6.33}$$

equation (6.32) will become

$$\ln(J_{th}) = \ln(J_0) - \frac{1}{L}\left(\frac{\ln R}{n\Gamma g_0}\right) \tag{6.34}$$

where J_0 is the threshold current density for infinite length. Therefore J_0 and $n\Gamma g_0$ can be calculated from the intercept and the slope respectively of the plot of $\ln(J_{th})$ against $\frac{1}{L}$

From equation (6.33), J_t can be calculated from J_0, using α, η_i and $n\Gamma g_0$ found previously. From the data in table 6.1, we can obtain the plots of $\frac{1}{\eta_e}$ against L and $\ln(J_{th})$ against $\frac{1}{L}$ as follows

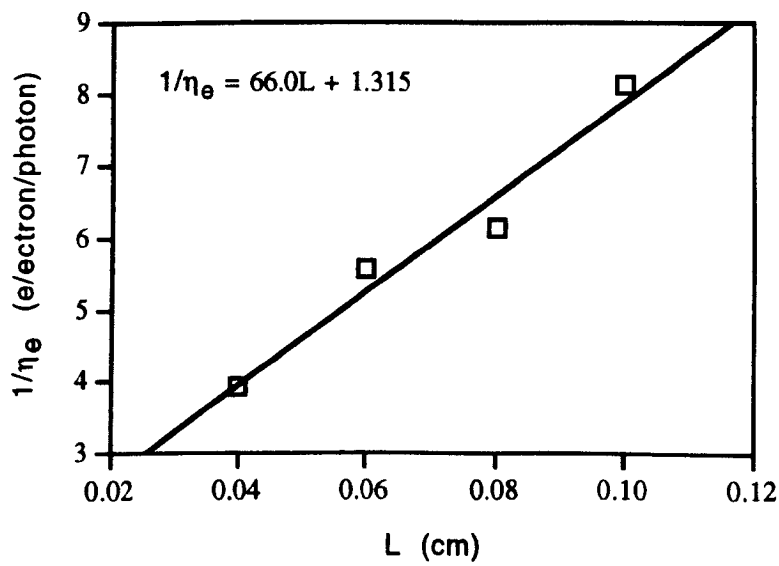

Fig. 6.17. Reciprocal of external quantum efficiency against laser cavity length

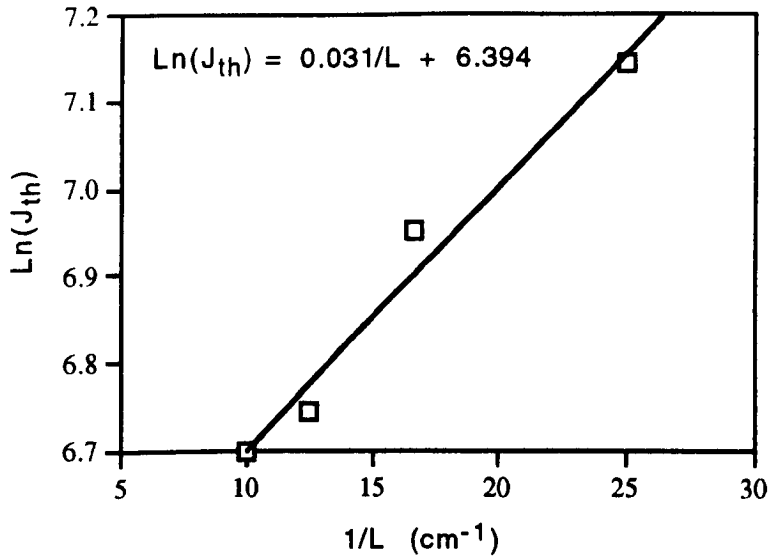

Fig. 6.18 Relationship between $\ln(J_{th})$ and $\frac{1}{L}$

So from Fig. 6.17 and Fig. 6.18, using the equations above, we obtain the material parameters shown in table 6.2. The parameters for the other wafers used in this research are also shown.

Table 6.2 The measured parameters for the material MR743 and other wafers

Wafer No	α (cm^{-1})	η_{int} (photon/electron)	g_0 (cm^{-1})	J_t (A/cm^2)	J_0 (A/cm^2)
MR673	7.6	24%	1042	28.5	679
MR743	60.4	76%	706	18.8	598
MR790	19.5	33%	547	17.6	510
MR876	82.7	55%	952	18	800

It should be noted the optical confinement factor, Γ, is assumed to be a value of 1.1% for each well, as calculated earlier (see Fig. 6.4).

6.8.3 Lasing Spectra of Oxide Lasers

The laser beam was collimated using a collimating lens then focused on to a multi-mode fibre using a X10 objective lens, and guided into a optical spectrum analyser. The laser current was controlled manually from the Avtech pulse generator. The spectra were transferred via an IEEE GPIB to the computer and saved to disk. Fig. 6.19 shows the spectrum of a laser with length of 400 μm at an injection current of 530 mA. As can be seen, the laser emitted at peak wavelength of around 1.55 μm, and the longitudinal wavelength separation was approximately 0.88 nm.

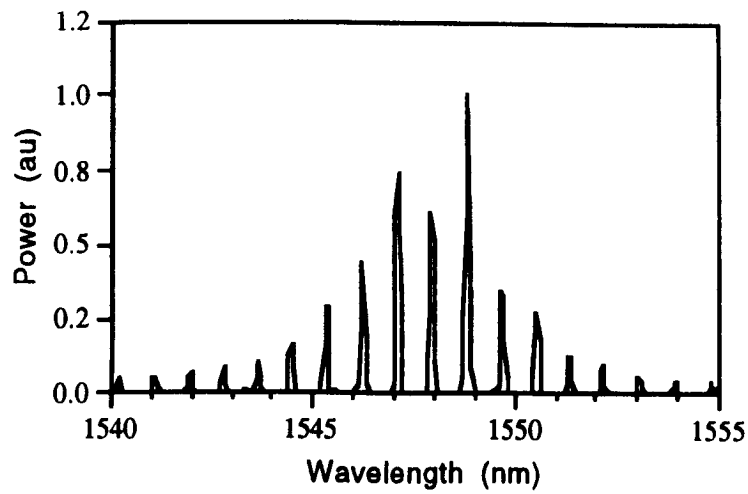

Fig. 6.19 Lasing spectra for the injecting current of 530 mA (material MR 876)

6.9 Fabrication of Ridge Lasers

6.9.1 Fabrication Process

Fig. 6.20 is a schematic representation of a ridge waveguide laser. The structure of material used to fabricate ridge lasers was identical to that of the material used to fabricate wide oxide stripe lasers. The fabrication process was more complicated and critical

compared to the fabrication of oxide stripe lasers, because more techniques were involved. The following are the processes used in the fabrication of ridge lasers:

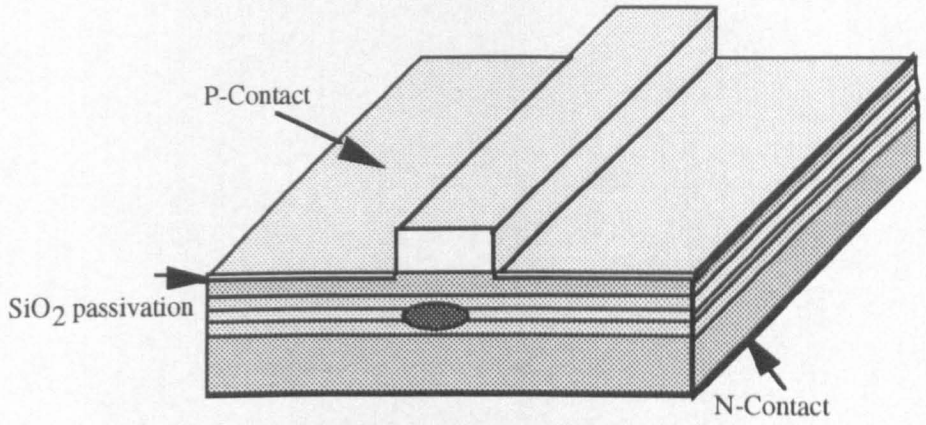

Fig. 6.20 A schematic representation for ridge waveguide lasers

1. **Sample preparation**: Sample was scribed to proper size, typically around 4.5x5.5 mm^2, and then cleaned with acetone and methanol each for 5 minutes. The sample was then rinsed in RO water and blown dry and left to dry in an oven for 5 minutes at a temperature of 90 °C. Subsequently, the sample was coated with a layer of 200 nm of PECVD silicon dioxide.

2. **Pattern definition:** Primer (dihexamethylsylane) was firstly spun on the sample, to improve the adherence of photoresist to the sample, followed by spinning of S1818 photoresist at 4000 rpm for 30 s, this producing a resist thickness of 1.8 μm. The sample was then baked for 30 mins at 90 °C. The sample was exposed to UV light for 10 s, and developed for 50 s in a solution of equal amounts of microposit developer and RO water. The ridge patterns were transferred to the sample from a mask.

3. **Dry etching of SiO_2:** The SiO_2 was etched in a RIE machine (BP 80) using C_2F_6 or CHF_3.

4. **Dry etching of InP:** The InP was etched in an Electro-Tech 340 machine using the process (g) shown in table 4.1 for 13 mins which produced an etch depth of 1.0 μm.

5. Wet etch of InP: The InP was wet-etched in a solution of Acetic acid : HCl : H_2O_2 : H_2O_1 (40:20:3:15) until a ridge step of around 1.2 μm was achieved. The etch rate is about 5 nm per second at temperature of 5 °C, hence, this process took about 40 seconds. It should be pointed out that lasers fabricated completely using the dry etch process had a very similar performance to that of those fabricated using the wet etch (see the Fig. 5.11 and Fig. 5.12), although the process of dry etch plus subsequent wet etch was usually employed.

6. Remove SiO_2 with buffered HF: Sample was placed in buffered HF to remove the SiO_2. Due to the deposition of a polymer on the surface of sample during processing in the ET-340, it took couple of minutes to remove the SiO_2 completely.

7. Deposit SiO_2 and annealing to remove dry etch damage: 200 nm of PECVD SiO_2 was deposited which formed an isolation layer, and the sample was then annealed for 60 seconds at 500 °C in RTA to remove the RIE damage.

8. Second Photolithography: As for the first photolithography stage (step 2), primer was firstly spun on the sample, followed by spinning of S1805 photoresist (instead of S1818) at 4000 rpm for 30 s, then baked for 30 mins at 90 °C. The sample was exposed to the UV light for 3.5 s, and developed for 10 s in a mixed solution of equal amounts of the microposit developer and RO water. The sample was inspected using an optical microscope to ensure that the contact window was properly opened. A post-bake in an oven at 120 °C for 15 minutes was necessary, which would further harden the photoresist and prevent subsequent silica-etching from diffusing into the region at the side of the windows. Silica-etching was performed using buffered HF (1 part of HF + 4 parts of RO water) for 14 seconds.

9. P-contact: A Ti/Pd/Au (40 nm/40 nm/200 nm) metal layer was evaporated onto the sample, forming a tunnelling Schottky contact.

10. Thinning and n-Contact: the sample was then thinned to reduce the substrate thickness to around 140-160 μm. This was achieved by polishing the substrate mechanically using 9 μm and 3 μm Al_2O_3 powder. The sample was cleaned and dried. A Au/Ge/Au/Ni/Au (14/14/14/14/200 nm) layer was evaporated on to the sample to form the n-contact.

11. Contact annealing: A high contact resistance produces heat which degrades the overall operation of devices, or even damages devices by breaking down their p-n junctions. The sample was therefore annealed for 60 seconds at 360 °C in the RTA, to reduced the contact resistance. Fig. 6.21 shows the measured *I-V* curves for a ridge laser diode. As can be seen, the dynamic resistance and threshold voltage have been reduced substantially after annealing.

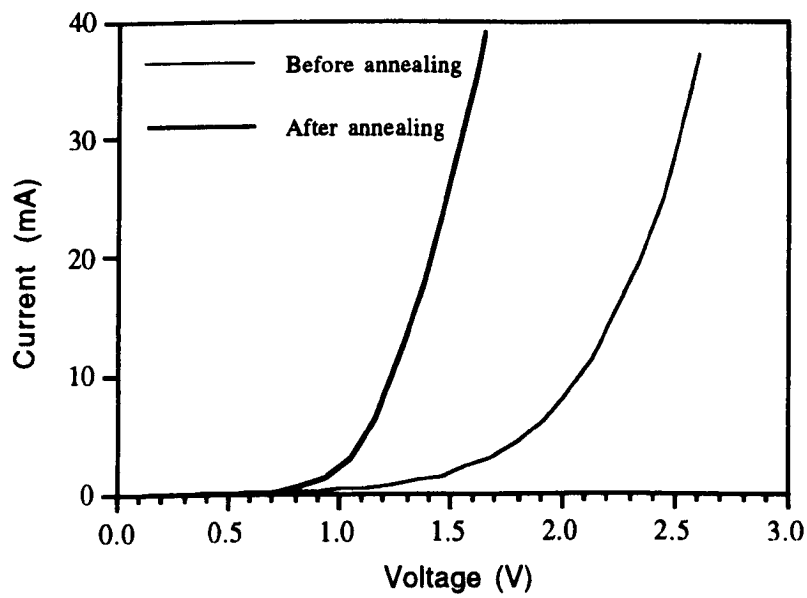

Fig. 6.21 *I-V* curves of a laser diode

12. Cleaving: Cleaving was performed by scribing small marks at the edge of the sample along the direction perpendicular to the waveguides. The devices were cleaved by aligning

the scribe marks with the edge of a blade, whilst gently applying force to the sample. In the direction parallel to the waveguide, the end facet reflection is not desired, therefore, scribing was performed across the whole sample, then cleaved using a blade as before.

6.9.2 $L-I$ Measurement

Measurement of the lasers was performed under pulsed current conditions as for oxide stripe lasers. Fig. 6.22 and Fig. 6.23 are the measured $L-I$ curves for the wafers MR743 and MR790, respectively. As can be seen, with the increase of the cavity length, the threshold current increases and the slope efficiency decreases. By analogy with OSLs, although the equations in section 6.8.2 can also be used to characterise ridge lasers, the results would be less accurate due the fact that injection current spreading in ridge lasers is more significant than that in OSLs. Comparing Fig 6.22 to Fig. 6.16, we can see that the threshold currents in the ridge devices were reduced substantially, because of the reduction of the device dimension (with width of 5 μm for ridge lasers, compared to 75 μm for OSLs) and both the optical and electrical confinements. Comparing Fig. 6.22 to Fig. 6.23, it can be seen the devices fabricated using material MR743 had a better performance than that of devices fabricated using material MR790, in terms of threshold current, this being consistent with the results of the OSLs fabricated using both materials.

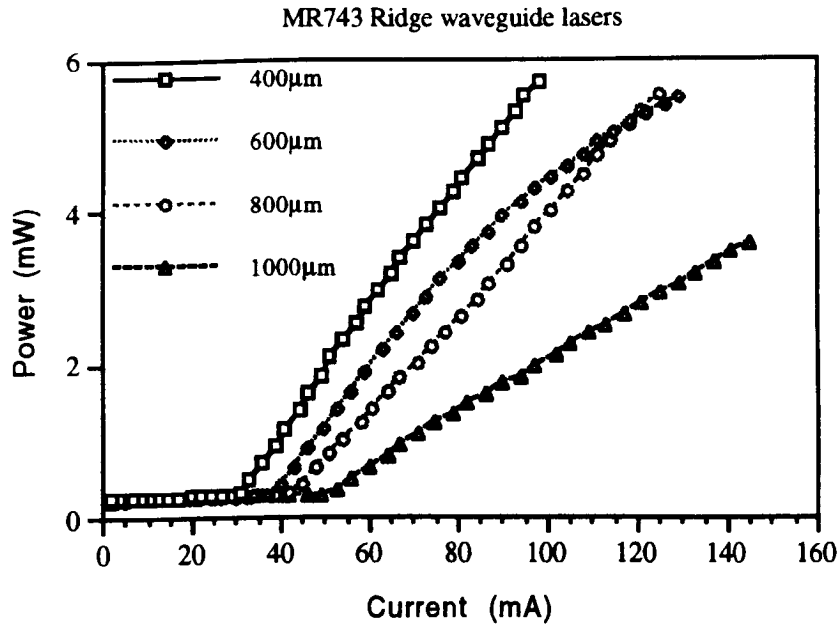

Fig. 6.22 Emitted light from one of the device facets as function of injection current

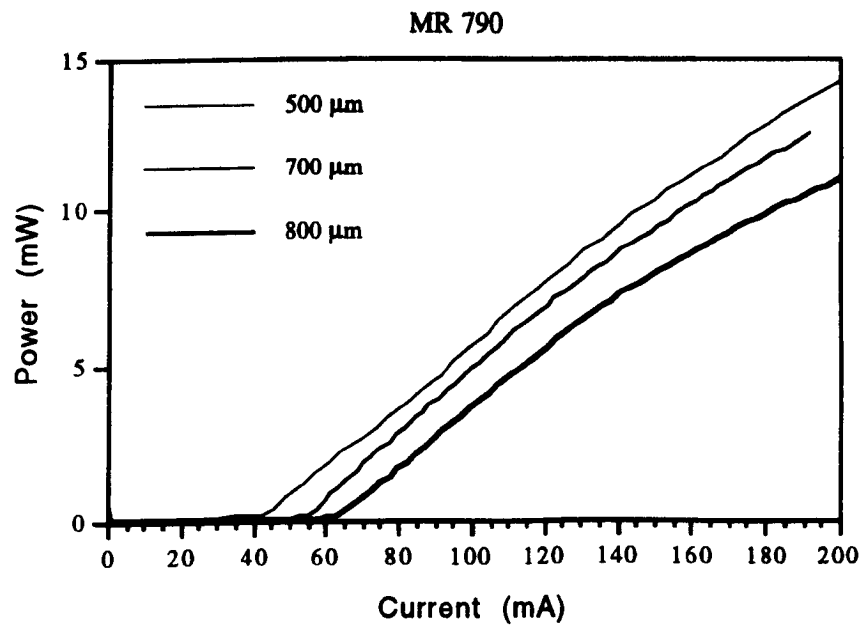

Fig. 6.23 Emitted light from one of the device facets as function of injection current

6.10 Fabrication of Two-section Ridge Lasers

6.10.1 Fabrication of Two-Section Ridge Lasers

Two-section lasers, as the name suggests, have two separated electrical contacts, as shown in Fig. 6.24. Due to their unique performance such as optical switching[21, 22], short pulse generation, either using Q-switching[23, 24], or mode-locking regime[25-29] as well as application to clock recovery [30, 31], two-section lasers have attracted considerable interest over the past few years. Successful fabrication of two section lasers is, therefore, of significance for the demonstration of pulse generation .

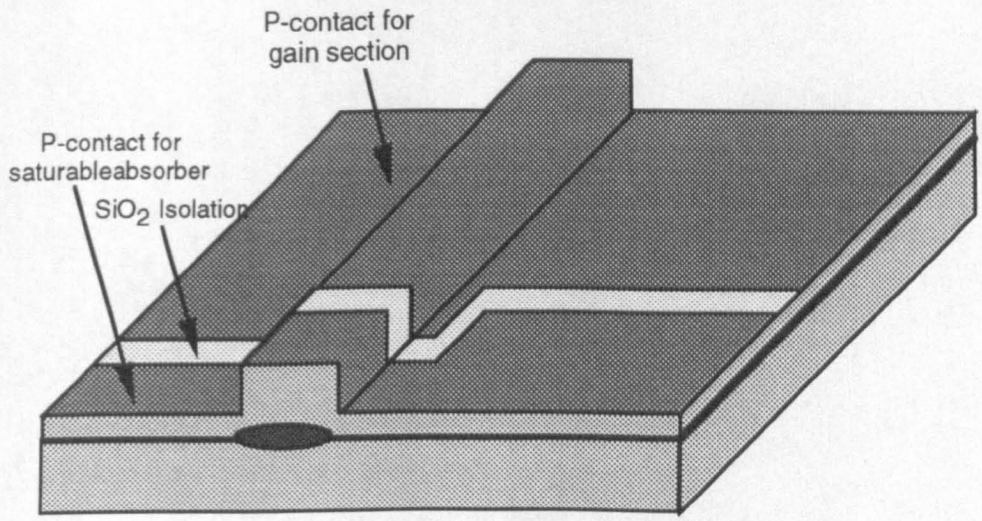

Fig. 6.24 A schematic representation of a two-section ridge laser

The structure of the material used to fabricate two-section lasers was identical to that of the material for fabrication of the ridge lasers. Essentially, the fabrication process is similar to the process for ridge lasers. However, before the p-contact evaporation is carried out, an extra photolithography stage was required to achieve the isolation between two contacts. The sample was spun with S1818 photo resist at 4000 rpm for 30 s, and then baked in an oven for 15 mins at 90 °C. The sample was subsequently immersed in chlorobenzene (C_6H_5Cl) for 18 mins, which improves the metal layer lift off process, and baked again at 90 °C for 8 mins. After p-contact evaporation, the sample was soaked in hot acetone, at

around 50-60 °C for from 30 mins to couple of hours, depending on the progress of the lift off process. To achieve a high isolation resistance between the two contacts, the highly doped InGaAs contact layer between the contacts was removed using a wet etching solution of H_2SO_4:H_2O_2:H_2O_1 (1:8:40) for 30 s; this etching solution selectively etches InGaAs over InP. The typical resistance between the two contacts, which was measured using an HP semiconductor parameter analyser, was around 5 kΩ. The sample was cleaved into individual devices, with the gain section and the absorption section lengths being 470 μm and 30 μm respectively.

6.10.2 Measurement of Light-Current Characteristics

The measurement of light-current ($L-I$) characteristics of the fabricated devices was performed under pulsed conditions. During the measurement, the gain section was forward biased, while the absorption section floated. Fig. 6.25 and Fig. 6.26 shows the typical $L-I$ curves for the materials MR743 and MR790. In contrast to normal ridge lasers, the $L-I$ curves of the two-section lasers exhibit a jump when the devices start to lase; this is due to the incorporation of the absorption section which must be bleached before lasing can take place.

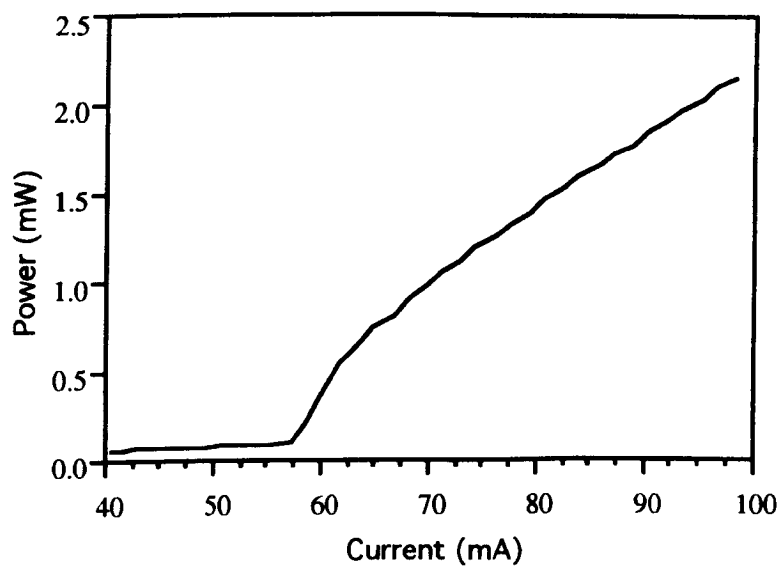

Fig. 6.25 $L-I$ curve of a two-section laser fabricated using MR743

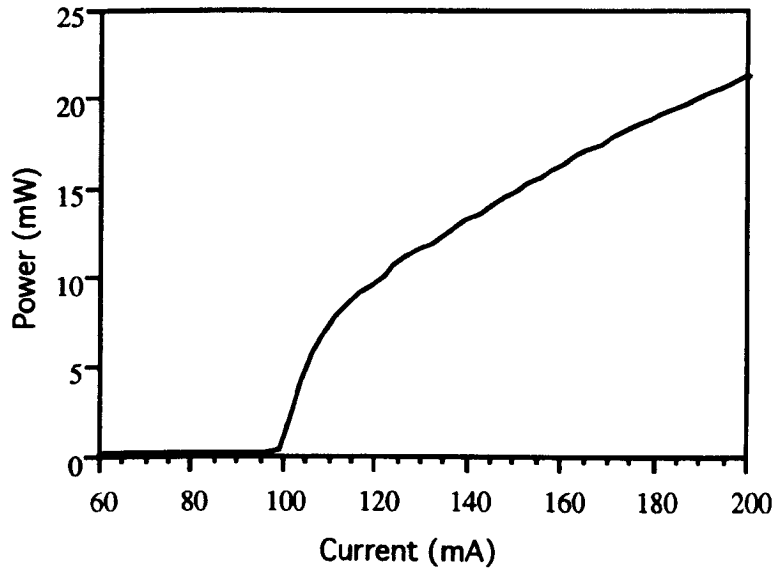

Fig. 6.26 $L-I$ curve of a two-section laser fabricated using MR790

6.10.3 Demonstration of Q-switching Using Two-section Lasers

The ability of the two-section lasers to generate Q-switched pulses was investigated. Fig. 6.27 shows the experimental set-up. The device was driven by a pulse generator as indicated in Fig. 6.27. Using a pulsed source instead of a constant source has two advantages: one is that device bonding, the process in which devices are bonded to a metal mount which acts as a heatsink, is not required, therefore avoiding the possible damage to the devices, and contamination to the facets of the devices, which can result in considerable degradation of the performance of the devices; the other advantage was that the sampling oscilloscope was triggered directly from the pulse generator.

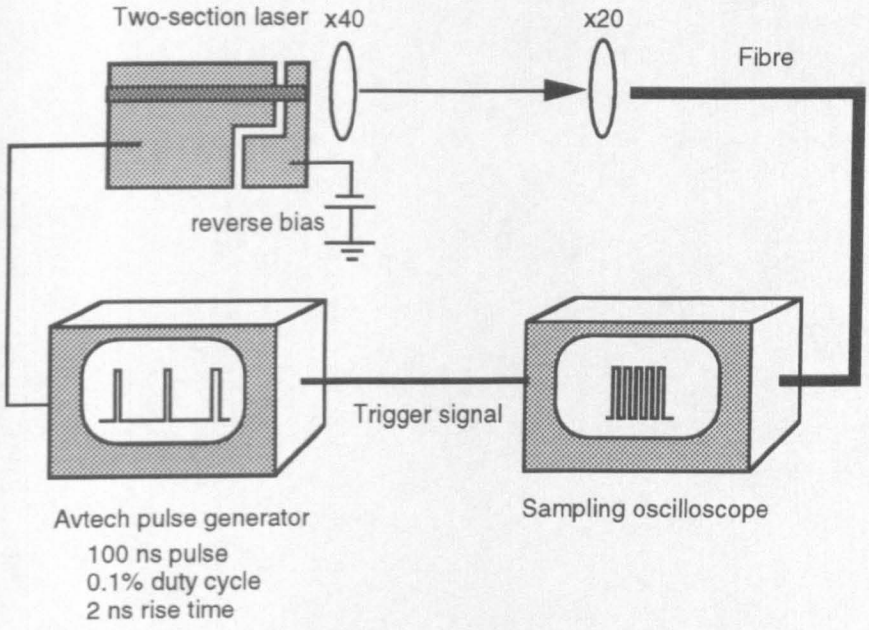

Fig. 6.27 Diagram for experimental set-up

Fig. 6.28 shows the observed pulses for I_g, the current of gain section, equal to 200 mA, while the saturable absorber was left floating.

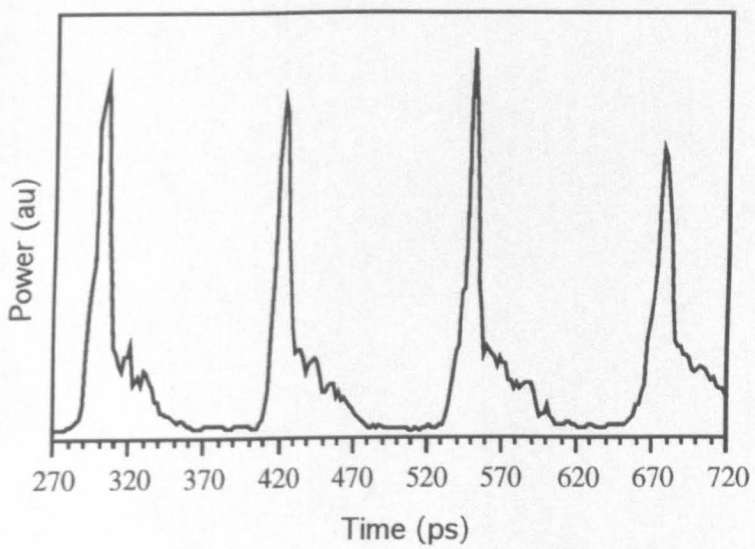

Fig. 6.28 Observed Q-switched pulses from a two-section laser

As can be seen from the figure, the repetion rate of the pulse were about 0.9 GHz, while average pulse width was around 90 ps. Unfortunately, the effect of reverse bias on performance of the 2-section laser has not been fully investigated.

6.11 Summary

In this chapter, the parameters which affect the performance of a laser device, such as losses, gain spectrum, and optical confinement in the quantum well structure were discussed and calculated. By fabricating oxide stripe lasers, parameters such as quantum efficiency, loss, threshold current density for infinite cavity length were obtained. Ridge waveguide lasers and two-section lasers were successfully fabricated and measured.

References

1. B. N. Hall, G.E. Fenner, J. D. Kingsley, T. J. Soltys, R. O. Carlson, "Coherent light emission from GaAs junction", Phys. Rev. Lett., **9**, pp. 366-368, 1962

2. M. I. Nathan, W. P. Dumke, G. Burns, F. H. Dill, Jr., G. Lashar, "Stimulated emission of radiation from GaAs P-N junction", Appl. Phys. Lett., **1**, pp. 62-64, 1962

3. T. M. Quist, R. H. Rediker, R. J. Keyes, W. E. Krag, B. Lax, A. L. McWhorter, H. J. Zeiger, "Semiconductor master of GaAs", Appl. Phys. Lett., **1**, pp. 91-92, 1962

4. N. Holonyak, Jr., S. F. BeVacqua, "Coherent (visible) light emission from $Ga(As_{1-x}P_x)$ junction", Appl. Phys. Lett., **1**, pp. 82-83, 1962

5. R.W.H. Engelmann, Chan-Long Shieh, C. Shu, "Multiquantum well lasers: threshold considerations", pp. 166, in "Quantum well lasers", Edited by Peter S. Zory Jr., Academic Press, 1993

6. H. Y. Fan, " Semiconductors and semimetals ", (R. K. Willardson and A. C. Beer, eds.), **3**, pp. 405, Academic Press, New York, 1967

7. D. E. Hill, "Infrared transmission and fluorescence of Doped Gallium Arsenide", Phys. Rev., **133**, A866-A875, 1964

8. W. G. Spitzer, and J. M. Whelan, "Infrared absorption and electron effective mass in n-type Gallium Arsenide", Phys. Rev., **114**, pp. 59-63, 1959

9. J. L. Merz, R. A. Logan, and A. M. Sergent, "Loss measurements in GaAs and $Al_xGa_{1-x}As$ dielectric waveguides between 1.1 eV and the bandgap", J. Appl. Phys., **47**, pp. 1436-1450, 1976

10. A. Sugimura, "Photon assisted gain coefficient in AlGaAs quantum well lasers"Appl. Phys. lett., **43**, pp. 728-730, 1983

11. N. K. Dutta, and R. J. Nelson, " The case for Auger recombination in $In_{1-x}Ga_xAs_yP_{1-y}$", J. Appl. Phys., **53**, pp. 74-92, 1982

12. L. C. Chiu, and A. Yariv, "Auger recombination in quantum-well InGaAsP heterostructure lasers", IEEE J. Quantum Electron.., **QE-18**, pp. 1406-1409, 1982

13. N.K.Dutta, "Photo-excited carrier lifetime and Auger recombination in 1.3 μm InGaAsP", J. Appl. Phys., **54**, pp. 1236-1409, 1983

14. A. Sugimura, "Comparison of band-to-band auger processes in InGaAsP", IEEE J. Quantum Electrron., **QE-19**, pp. 923-941, 1983

15. C. Smith, R. A. Abram, and M. G. Burt, " Auger recombination in a quantum well heterostructure", J. Phys. C, **16**, pp. L171-L173, 1983

16. W. T. Tsang, "A graded-index waveguide separate-confinement laser with very low threshold and a narrow gaussian-beam", Appl. Phys. Lett., **39**, pp. 134-137, 1981

17. M. Rosenzweig, M. Möhrle, H. Düser, and H. Venghaus, "Threshold-current analysis of InGaAs-InGaAsP multiquantum well separate-confinement lasers", IEEE J. Quantum Electron.., **QE-27**, pp. 1804-1810, 1991

18. M. Asada, A. Kameyama, and Y. Suematsu, " Gain and intervalence band absorption in quantum-well lasers", IEEE J. Quantum Electron.., **QE-20**, pp. 745-753, 1984

19. R. H. Yan, S. W. Corzine, L. A. Coldren, and I. Suemune, "Corrections to the expression for gain in GaAs", IEEE J. Quantum Electron.., **QE-26**, pp. 213-216, 1990

20. E. Zielinski, H. Schweizer, S. Hausser, R. Stuber, M. Pilkuhn, and G.Weimann, "Systematic of laser operation in GaAs/AlGaAs multiquantum well heterostructures", IEEE J. Quantum Electron.., **QE-23**, pp. 969-975, 1987

21. H. Uenohara, H. Iwamura, M. Naganuma, "Switching characteristics of InGaAs/InP multiquantum well voltage controlled bistable laser diode", Jpn. J. Appl. Phys., **29**, pp. L2442-L2444, 1990

22. J. Hörer, K.Weich, M. Möhrle, and B. Sartorius, "Optimisation of the optical switching characteristics of two-section Fabry-Perot lasers", IEEE photonics Technol. Lett., **5**, pp. 1273-1276

23. D.Z. Tsang, J.N. Walpole, "Q-switched semiconductor diode lasers ", IEEE J. Quantum Electron. **19**, pp. 145-156, 1983

24. P.E. Barnsley, H.J. Wickes, G.E. Wichens, and D.M. Spirit, "All-optical clock recovery from 5 Gb/s RZ data using a self-pulsation 1.56 μm laser diode", IEEE photonics Technol. Lett. **3**, pp. 942-945, 1991

25. D.J. Derickckson, R.J. Helkey, A. Mar, J.R. Karin, J.G. Wasserbauer, and J.E. Bowers, "Short pulse generation using multisegment mode-locked semiconductor lasers", IEEE J. Quantum Electron. **28**, pp. 2186-2202,1992

26. T. Schrans, R.A. Salvatore, S. Sanders, and A. Yariv, "Subpicosecond (320 fs) pulses from cw passive mode-locked external cavity two-section multiquantum well lasers", Electron. Lett. **28**, pp. 1480-1482, 1992

27. P.P. Vasil'ev, A.B. Sergeev, "Generation of bandwidth-limited 2 ps pulses with 100 GHz repetition rate from multi-segmented injection laser", Electron. Lett., **25**, pp. 1049-1050, 1989

28. F. Camacho, E.A. Avrutin, P. Cusumano, A.S. Helmy, A.C. Bryce, and J.H. Marsh, "Improvements in mode-locked semiconductor diode lasers using monolithically integrated passive waveguides made by quantum-well intermixing", IEEE Photonics Technol. Lett., **9**, pp. 1208-1210, 1997

29. F. Camacho, D.A. Barrow, E.A. Avrutin, A.C. Bryce, J.H. Marsh, "Two-contact semiconductor mode-locked lasers", International J. of Optoelectron., **10**, pp. 433-437, 1995

30. D.J. As, R. Eggemann, U. Feiste, M. Möhrle, E. Patzak, and K. weich, "Clock recovery based on new type of selfpulsation in 1.5 μm two-section InGaAsP-InP DFB laser", Electron Lett., **29**, pp. 141-142, 1993

31. K. Weich, R. Eggemann, J.Hörer, D.J. As, M. Möhrle, and E. Patzak, "10 GHz/s all-optical clocked decision circuit using two-section semiconductor lasers", Electron Lett., **30**, pp. 784-785, 1994

32. M. Mehdi Karkhanehchi, "Generation and detection of short optical pulses using semiconductor devices", Ph.D. Thesis, University of Glasgow, 1997

7. Fabrication of Extended Cavity Ridge Waveguide Lasers

7.1 Introduction

The various techniques of quantum well intermixing offer the possibility of monolithic integration of active devices and passive devices. One of the simplest forms of such an integrated circuit is an extended cavity ridge waveguide laser in which a bandgap widened passive section is incorporated. Fig. 7.1 is a schematic representation of an extended cavity ridge laser.

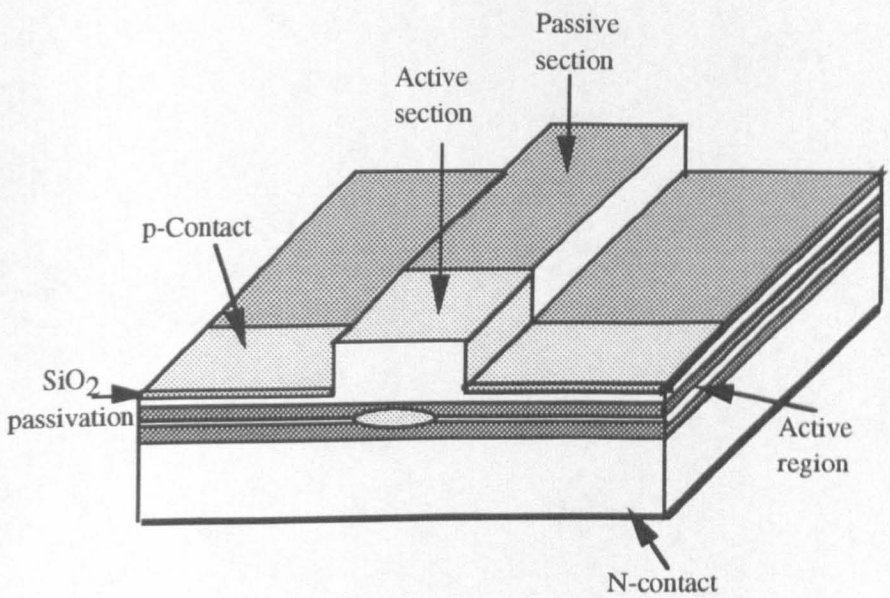

Fig. 7.1 An illustration of extended cavity ridge lasers

A device such as this also has practical application. For example, the use of an external cavity to narrow the linewidth of a semiconductor laser is commonplace, but most

configurations use bulk optics and require careful alignment with good mechanical stability. An internal cavity promises to be appreciably more stable and requires a cavity approximately four times [1] shorter than an equivalent air cavity. Experiments [2] have shown that GaAs/AlGaAs mode-locked extended cavity lasers with integrated low loss passive waveguides display superior performance to devices in which the entire waveguide is active. Advantages include the reduction of the threshold current by a factor of 3 to 5, reduction of the pulse width from 10.2 ps to 3.5 ps, and decrease in the free-running jitter from 15 to 6 ps.

Fabrication of a laser with a built-in passive waveguide section can be accomplished by using some form of intermixing process to produce a bandgap-widened passive waveguide which is transparent to the laser wavelength. This chapter documents the results from extended cavity lasers fabricated using the laser process and the plasma process.

7.2 Measurement of the Optical Propagation Loss in Bandgap Widened Waveguides

Fabrication of an extended cavity ridge laser relies on the realisation of a low loss waveguide in the passive section of the laser but, due to the fact that the lasing action always occurs at a wavelength very close to the band edge, an unpumped passive waveguide section will be highly absorbing. One of the solutions to this problem is to use QWI, because QWI shifts the absorption edge to a higher energy, which would make an intermixed waveguide transparent to the laser light at the wavelength of a non-disordered active section. Apart from the bandedge absorption, absorption can also arise from free carriers and scattering due to both the roughness between the interfaces of the epitaxial layers and the roughness of the etched waveguides. The loss in the passive waveguide of an extended cavity lasers has an important impact on the overall performance of the device.

therefore it is important to measure the loss in waveguides which are processed using QWI before fabrication of extended cavity ridge lasers.

7.2.1 Material Structure

The structure of the material (wafer No: MR790) used to fabricate low loss waveguide was grown by metal organic vapour phase epitaxy (MOVPE) on a (100)-oriented n -type InP substrate and consisted of five 65Å InGaAs wells with 120Å InGaAsP barriers(λ_g=1.26μm, where λ_g is the wavelength corresponding to the bandgap). The active region was bounded by a stepped graded index (GRIN) waveguide core consisting of InGaAsP confining layers. The thicknesses and compositions of these layers (from the QWs outward) were 500Å of InGaAsP with λ_g=1.18μm and 800Å of λ_g=1.05μm. The structure, which was lattice matched to InP throughout, was completed by an InP cladding layer and an InGaAs contact layer. The first 0.2μm of upper cladding layer was an undoped spacer layer and the remaining 1.2μm was doped with Zn to a concentration of $7X10^{17}$ cm^{-3}. The lower cladding layer was Si doped to a concentration of $5X10^{18}$ cm^{-3}. The waveguide core was undoped , thus forming a *pin* structure with the intrinsic region restricted to the QWs and GRIN layers.

The material was coated with PECVD SiO_2 and then processed using a combination of PAID and P-PAID simultaneously to widen the bandgap of the material. 77 K PL measurements indicated that the intermixed material had blue-shifted by around 110 nm relative to as-grown material. 2 μm wide waveguides were formed by RIE dry etching using the ET340 with gases $CH_4/H_2/O_2$ to a depth of 1.2 μm. Individual waveguides were cleaved with a length of 3.5 mm. Fig. 7.2 shows an SEM picture of the waveguide. The loss measurement was carried out using the Fabry-Perot method.

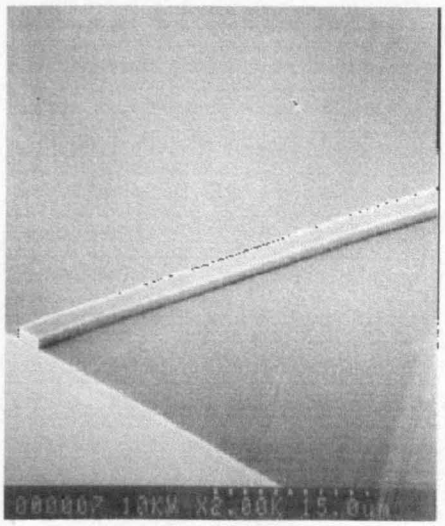

Fig. 7.2 Dry etched waveguide.

7.2.2 Fabry-Perot Loss Measurements

The Fabry-Perot loss measurement technique was developed by Walker [3]. As its name suggests, the technique is based on the Fabry-Perot cavity resonance action of a semiconductor waveguide. The measurement is simple, non-destructive, and is insensitive to input and output intensities.

Assuming the wave transmitted through the device cavity is coherent and monochromic, the resonant T_R and antiresonant T_A transmitted intensities are given by [3]:

$$T_R = I_0\left(\frac{\gamma}{1-\gamma^2 R}\right)^2 \tag{7.1}$$

$$T_A = I_0\left(\frac{\gamma}{1+\gamma^2 R}\right)^2 \tag{7.2}$$

where I_0 is the input intensity of the incident light, γ is the single-pass amplitude reduction factor and R is the geometric mean of the two power reflection coefficients at the facets of the waveguide, which can be written as:

$$R = \left(\frac{n-1}{n+1}\right)^2 \tag{7.3}$$

where n is the refractive index of the material, which can be replaced using an effective index in the case when the material structure is a multilayer structure, e.g. a waveguide structure. Defining the ratio $k = \frac{T_R}{T_A}$, then the single round trip loss in the F-P cavity is

$$\gamma = e^{-2\alpha L} = \frac{\sqrt{k}-1}{R(\sqrt{k}+1)} \tag{7.4}$$

From Eq.(7.4), the propagation loss α can be written as:

$$\alpha = -\frac{1}{2L}\ln\left[\frac{\sqrt{k}-1}{R(\sqrt{k}+1)}\right] \text{ (cm}^{-1}\text{)} \tag{7.5}$$

or

$$\alpha = -\frac{2.17}{L}\ln\left[\frac{\sqrt{k}-1}{R(\sqrt{k}+1)}\right] \text{ (dB.cm}^{-1}\text{)} \tag{7.6}$$

where L is the device cavity length in cm. As can be seen from equation (7.5), this loss measurement technique is independent on the input and output intensities, therefore accurate coupling of light into the waveguide is not crucial and high accuracy of measurement can be achieved.

7.2.3 Experiment

Fig. 7.3 shows the experimental set-up for loss measurements using the Fabry-Perot technique. The beam from a DFB semiconductor laser, operated at a wavelength of 1.56 μm, was collimated and coupled into the waveguide devices; the transmitted light from the devices was coupled into a multi-mode fibre then to a spectrum analyser to measure its

power. The spectrum analyser was used for convenience, as it has a high sensitivity. During the measurement, it was set to a fixed wavelength of 1.56 μm, corresponding to the DFB emission wavelength. The camera and monitor were used to assist the alignment; the aperture was adjusted such that only the guided light from waveguides was coupled into the fibre. During the experiment, heat was supplied to the sample in the form of a fine tipped soldering iron, which in turn changed the refractive index and cavity length of the device due to the change of temperature of the device, resulting in Fabry-Perot oscillations being observed on the optical spectrum analyser. Fig. 7.4 shows the recorded oscillations. The oscillation fringes are not perfectly of the form expected from a F-P resonator, which may be due to higher transverse modes in the waveguide. This would result in superposition of corresponding oscillation fringes.

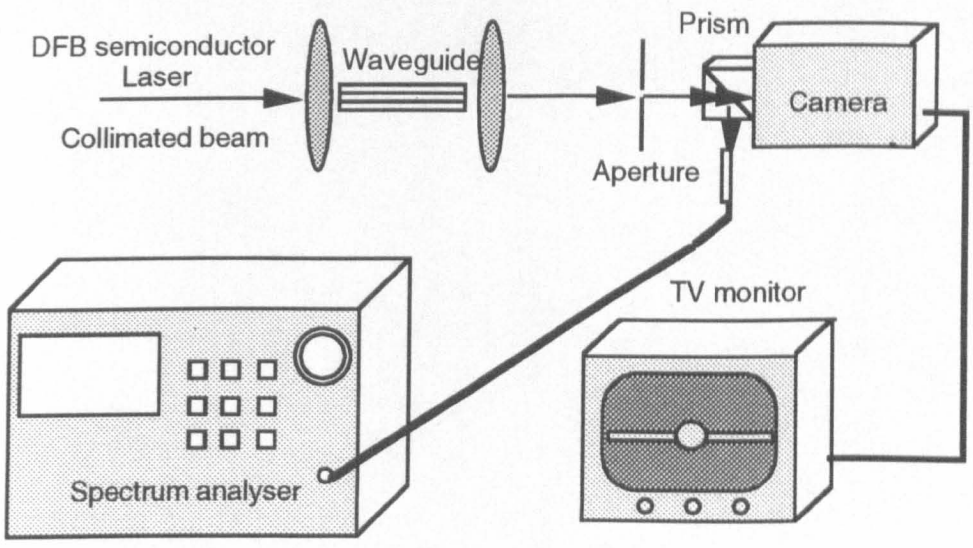

Fig. 7.3 Experimental set-up for measuring waveguide loss

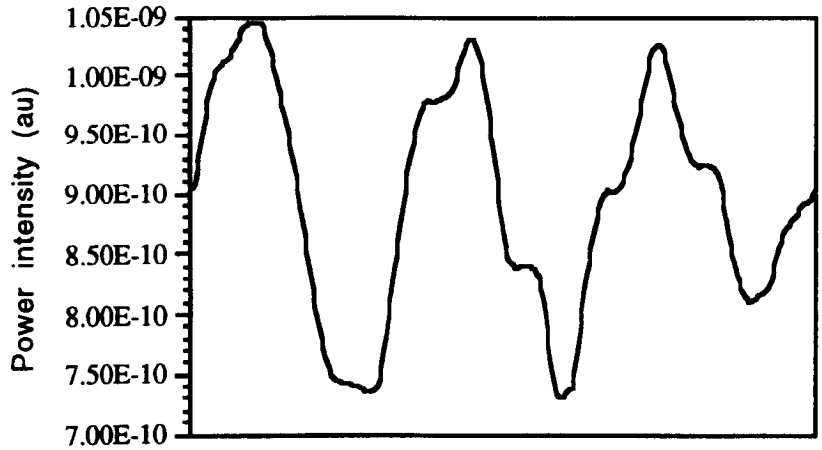

Fig. 7.4 Observed Fabry-Perot oscillation from a single mode waveguide

The contrast k, which is the ratio of maximum to the minimum transmitted intensity, can be obtained from Fig. 7.4, then using Eq. (7.5), it yields a loss of approximately 2.1 cm^{-1} in the waveguide. This is a dramatic reduction in the loss of waveguide, compared to the loss of the as-grown material, which is 19.5 cm^{-1} at the wavelength of 1.55 μm.

7.3 Fabrication of Extended Cavity Ridge Lasers Using a Combination of both P-PAID and PAID Technique

The structure of the material (wafer No: MR790) used to fabricate extended cavity lasers (ECL) is a normal laser p-i-n structure which has been described in section 7.2.1 in detail. As pointed out before, fabrication of extended cavity lasers relies on the formation of low loss waveguides, which in turn require that the bandgap of the material is widened in the passive sections of the lasers. QWI is a simple and effective way to meet this requirement. The following describes the process steps.

7.3.1 QWI using a Combination of both P-PAID and PAID

1. Deposition of SiO_2: The sample was coated with a layer of 500 nm silicon dioxide by plasma enhanced chemical vapour deposition (PECVD). Deposition of a layer of 200 nm of SiO_2 was also tried, but the surface quality of material after intermixing was rather bad. This is because a thinner layer of SiO_2 cannot effectively mask diffusion of the Ni/Cr-Au metal layer, which was evaporated on top of the SiO_2, to acts as a laser reflection mask during subsequent laser intermixing. (see Fig. 7.6a).

2. Alignment marks: alignment marks are required for the definition of the interface between the active and passive sections of devices. Alignment marks were defined on the sample by photolithography, followed by silicon dioxide etching with HF to remove the SiO_2 of 500 nm in the alignment mark regions. Finally, using a etching solution of H_2SO_4:H_2O_2:H_2O=1:8:40 to etch the InGaAs contact layer, alignment marks were transferred onto the sample permanently. (see Fig. 7.6 b).

3. Evaporation of metal layer: metal layers of 10 nm NiCr and 200 nm Au were evaporated to protect the active regions of the sample using photolithography and lift-off. The metal layer acts as a reflection layer to the incident laser light during the subsequent laser intermixing process. The intermixing experiments show that the NiCr/Au metal layers effectively reflect the incident laser beam (see Fig. 7.6c, d).

4. Intermixing: The sample was then placed on a piece of polished ceramic on a hotplate at around 340 °C, to reduce the incident CW laser power density required to heat the sample to a temperature at which the QWI occurs. The material was irradiated simultaneously with light from CW and pulsed Nd:YAG lasers, both emitting at 1.064 μm, for times of around 3-5 mins. The pulsed laser operated at repetition frequency of 10 Hz with a pulse length of around 7 ns. The power density of the CW laser, which was around 2W/mm^2, was chosen such that no significant disordering occurs if the pulsed

laser is not involved. The energy density of the pulsed laser was around 0.2 mJ/mm^2 (Fig. 7.6e).

5. 77 K PL measurement: PL measurements were performed at 77 K on the intermixed sample to check if the required blueshift had been achieved. If not, step 4 was repeated until the required blueshift was obtained.

6. Removal of the metal layer: The Au layer was removed using gold etching solution for 2 mins, and then the NiCr layer was lifted-off by etching the SiO_2 with buffered HF for around 3-5 mins. The sample still retained a good surface quality after removing the metal layer, although it was found that the gold etching attacked the InGaAs layer of the material due to pinholes in the SiO_2 layer (Fig. 7.6f).

7. Spatial resolution: Due to the fact that the above intermixing process has a graded region of several hundreds μm, PL measurements should be performed again to define the pumping regions of the lasers, as is shown in Fig. 7.5.

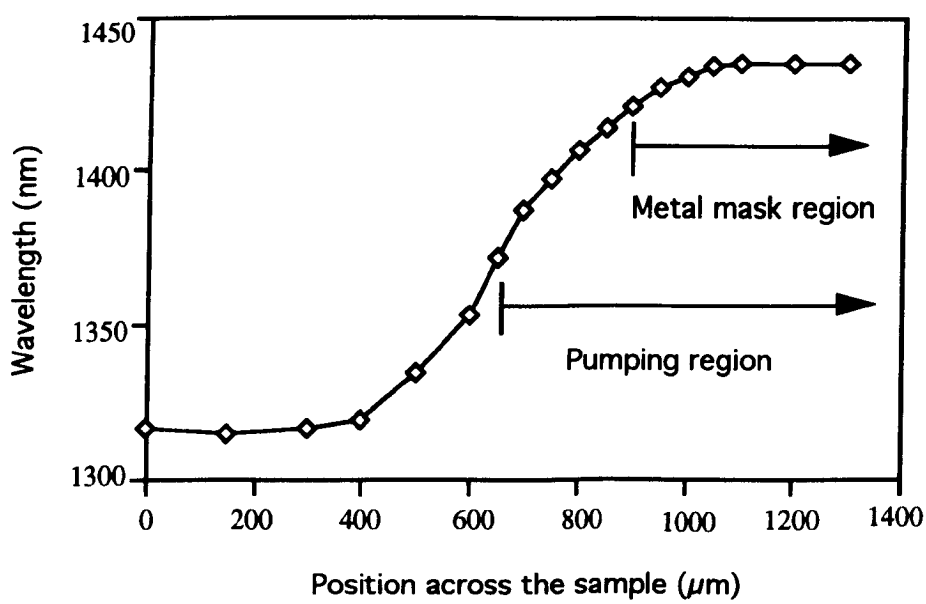

Fig. 7.5 Grade region was also pumped.

8. Deposition of SiO_2 of 200 nm: A layer of 200 nm SiO was deposited again for the fabrication of devices (Fig. 7.6g).

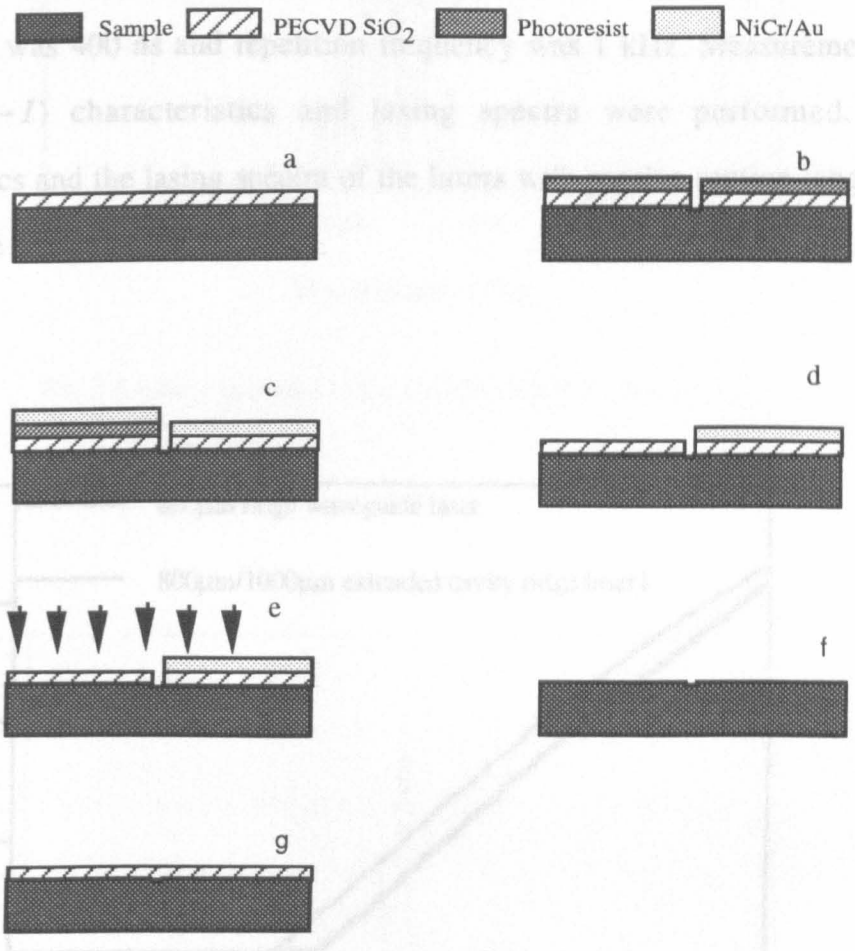

Fig. 7.6 Diagram of the processes for the intermixing Using P-PAID+PAID

7.3.2 Fabrication Of Extended Cavity Lasers

Ridge waveguides were formed by chemical wet etching to a depth of 1.2 μm. Before silicon dioxide was removed, the InGaAs contact layers in the passive region of the sample were removed to avoid electric current spreading into the passive region of devices through the heavily doped layers. SiO_2 of 200 nm was deposited again as a passivation layer, and a contact window was opened on top of the ridges. The sample was then

thinned, and metal contacts (p-Ti-Au, n-Au-Ge-Au-Ni-Au) were evaporated on both surfaces and annealed in an RTA for 60 s at 360 °C. Finally, the sample was cleaved into individual lasers with 800 μm long active sections and passive sections of 1000 μm.

The lasers were tested under pulsed current conditions at room temperature. The current pulse width was 400 ns and repetition frequency was 1 kHz. Measurements of light-current ($L-I$) characteristics and lasing spectra were performed. The $L-I$ characteristics and the lasing spectra of the lasers with passive section lengths of 0 and 1000 μm are shown in Fig. 7.7 - 7.9.

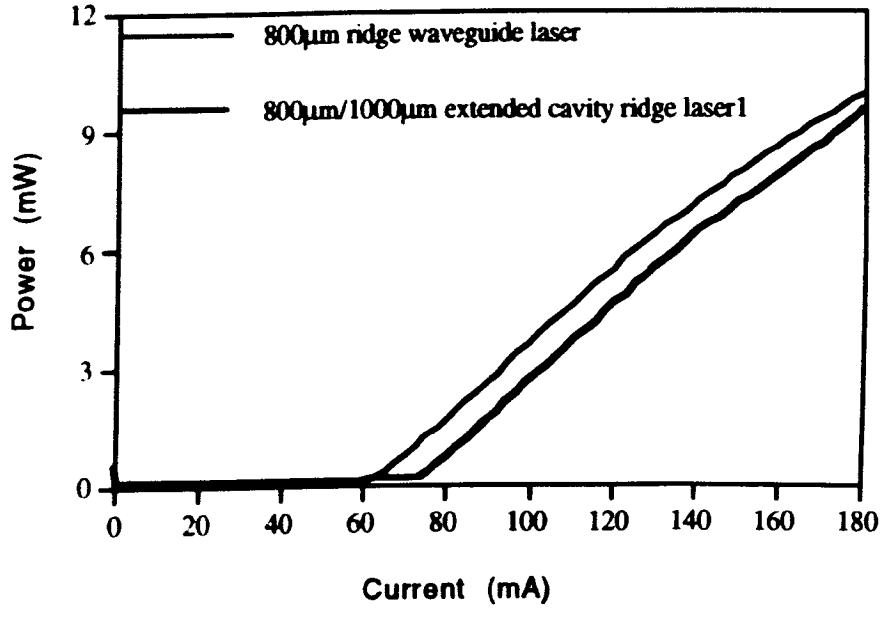

Fig. 7.7 Measured $L-I$ of ridge lasers with and without extended cavity.

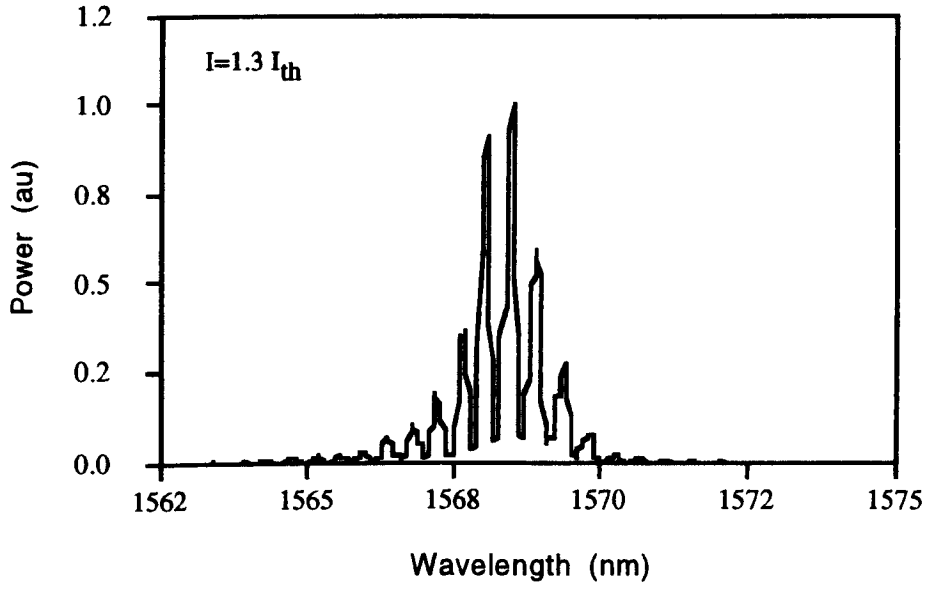

Fig. 7.8 Lasing spectrum of the 800 μm all active ridge laser

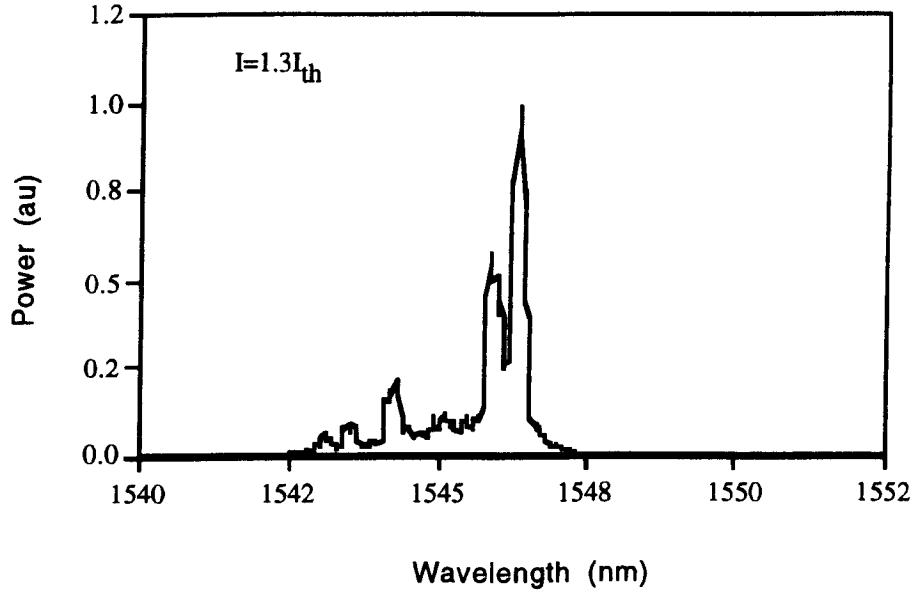

Fig. 7.9 Lasing spectrum of the 800 μm/1000 μm extended cavity laser

7.3.3 Discussions

It can be seen from Fig. 7.7 that the slope efficiency of the extended cavity lasers, which had lengths of 800 μm and 1000 μm for the active section and passive sections, is very

close to that of lasers with same length of active section, and the increase in threshold current is 10 mA compared to the 800 μm long all-active device. This suggests that the loss in the passive section has been reduced considerably by QWI.

From the measured threshold currents for the all-active and extended cavity lasers, the loss in the passive region can be calculated from the measured threshold current data shown in Fig. 7.7 by applying the following formula [4]:

$$\frac{I_{ex}}{I_{nor}} = \exp\left(\frac{\alpha_p L_p}{n\Gamma g_0 L_a}\right) \tag{7.7}$$

where I_{ex}, I_{nor} are the threshold currents of the lasers with and without passive section. L_p, L_a are the lengths of the passive section and the active section, α_p is the loss in the passive region, n is the number of wells, Γ the optical overlap per well and g_o the QW gain parameter. The product $n\Gamma g_0$ was 30 cm^{-1} calculated from measurements performed on wide oxide stripe lasers fabricated for the characterisation of the material. If the gain section is taken to be 800 μm in both lasers, the calculated loss α_p is then 3.8 cm^{-1}. This is significantly larger than that measured in the waveguide sample, a disagreement which is due to the fact that current is injected into the graded bandgap interface region in the extended cavity lasers. Pumping the transition region has effect of increasing current and whilst making little contribution to the gain at the operating wavelength. If this factor is taken into account by assuming the effective length of gain section in the extended cavity laser is 600 μm, the calculated loss is 2.4 cm^{-1}, in good agreement with the loss measured by the Fabry-Perot technique.

7.4 Fabrication of Extended Cavity Ridge lasers Using Plasma Process

As pointed out in the previous chapter, this process is a simple, reliable, and reproducible technique. To investigate further the possibility of this approach for use in photonic integration, extended cavity ridge lasers were again fabricated. The structure of material

(wafer No: MR876) used to fabricate the extended cavity ridge lasers was almost identical to that used to fabricate the same devices using PAID plus P-PAID laser process, except that an undoped layer of 50 Å InGaAs with bandgap corresponding to a wavelength of λ_g=1.1 μm, was introduced to the structure, located above the 2000 Å InP spacer layer to act as a wet etch stop layer. The following will describe the fabrication process and measured results.

7.4.1 Fabrication process

1. 200 nm PECVD SiO_2 was deposited onto the cleaned sample (Fig. 7.10a).

2. Defining the active and passive sections: Photoresist type S1818 was spun onto the sample at spinning speed of 4000 rpm for 30 s; the thickness of resist would be 1.8 μm. The sample was then baked for 30 mins at 90 °C. Alignment marks were then transferred to the sample by exposing the sample to the UV light for 13 s using the mask aligner, followed by developing the sample for 75 s in the mixture solution of equal amounts of the microposit developer and RO water. Etching of the SiO_2 layer using HF for 30 s and subsequent etching of InGaAsP contact layer of the material using a etching solution of H_2SO_4:H_2O_2:H_2O=1:8:40 were used to transfer the alignment marks to the sample (Fig. 7.10b). The photoresist over the passive sections of the sample was removed by exposing the sample to UV light again using mask aligner and subsequent developing, as illustrated in Fig. 7.10c.

3. Etching SiO_2: Bake the sample for 15 mins and then remove the SiO_2 from the passive section of the sample (see Fig. 7.10d).

4. Deposition of Sputter SiO_2: 200 nm of sputtered SiO_2 was deposited in a Nordiko sputtering machine at a RF power of 100 W and a DC bias of 1 kV, using a 9:1 Ar:O_2 gas mixture (see Fig. 7.10e).

5. Clean the photoresist on the sample using Acetone: as is shown in Fig. 7.10f.

6. Anneal the sample using CW laser: The sample was annealed using the CW Nd:YAG laser operating at 1.064 μm with power density of 1.3 W/mm^2 (which is lower than the power density used for the PAID+P-PAID (2 W/mm^2) for 3 mins (Fig. 7.10g).

7. 77 k PL measurement: 77 K PL measurement was performed to check if the required blueshift had been achieved; if not the process 6 was repeated for 1-2 mins.

8. Deposition of PECVD SiO_2: The SiO_2 layer was removed from the sample using buffered HF (Fig. 7.10h), then deposition of 200 nm PECVD SiO_2 was carried out, as shown in Fig. 7.10i.

9. Fabrication of Ridge lasers: The ridge waveguides were formed by RIE dry etching to a depth of 1.2 μm, using a $CH_4/H_2/O_2$ gas mixture. 200 nm of SiO_2 was deposited again as a passivation layer. A contact window was opened on top of the ridges. The sample was then thinned, and metal contacts (p-Ti-Au, n-Au-Ge-Au-Ni-Au) were evaporated on both surfaces and annealed in an RTA for 60 s at 360 °C. Finally, the sample was cleaved into individual lasers with 800 μm long active sections, and passive sections of 1000 μm.

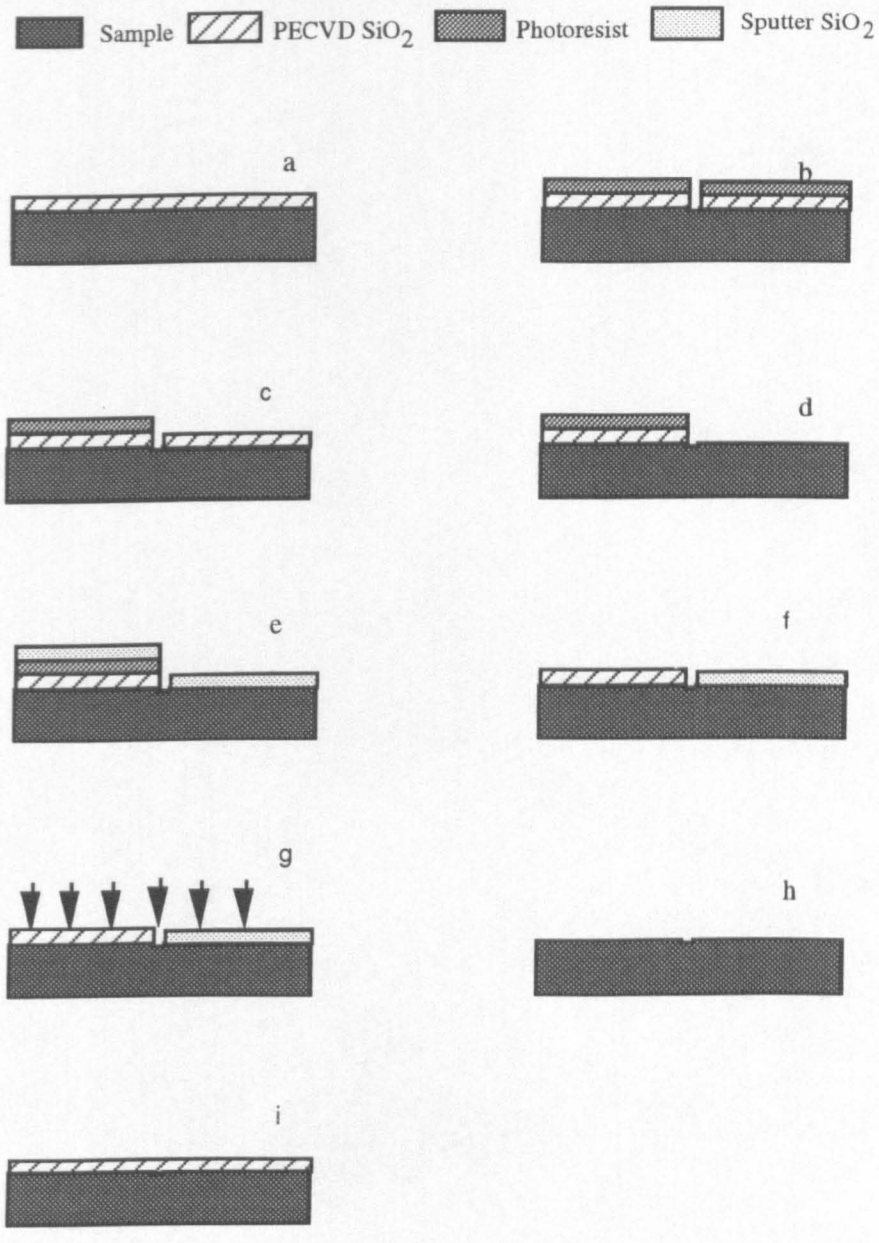

Fig. 7.10 Diagram of plasma processes

7.4.2 Results

The lasers were tested under pulsed current conditions at room temperature. The current pulse width was 400 ns and repetition frequency was 1 kHz. Measurements of light-current ($L-I$) characteristics and lasing spectra were performed. The $L-I$ characteristics and the lasing spectra of the lasers with passive section lengths of 0 and 1000 μm are shown in Fig. 7.11-7.16.

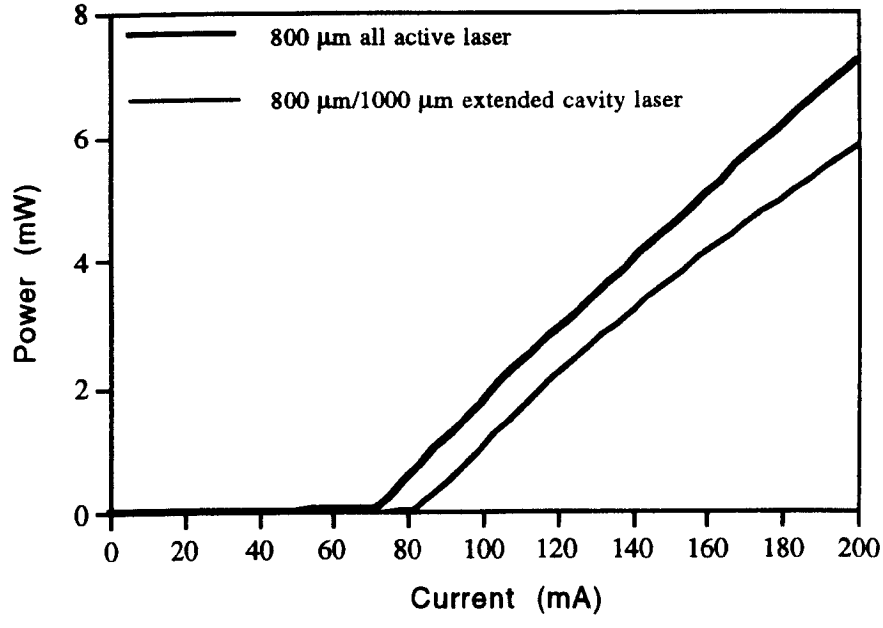

Fig. 7.11 Comparison of the $L-I$ characteristics for all active and extended cavity ridge lasers.

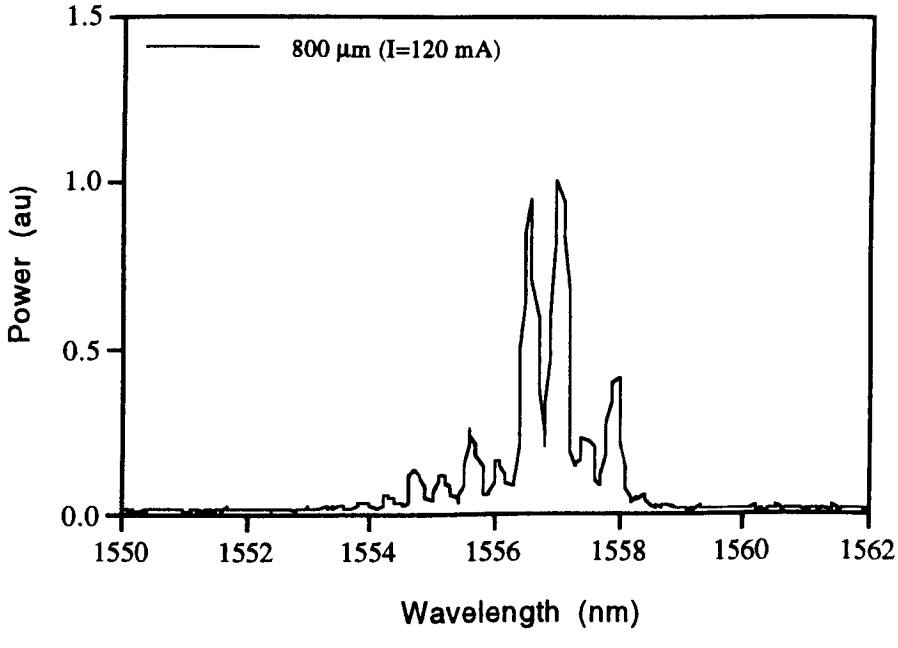

Fig. 7.12 Spectrum of an all active ridge laser.

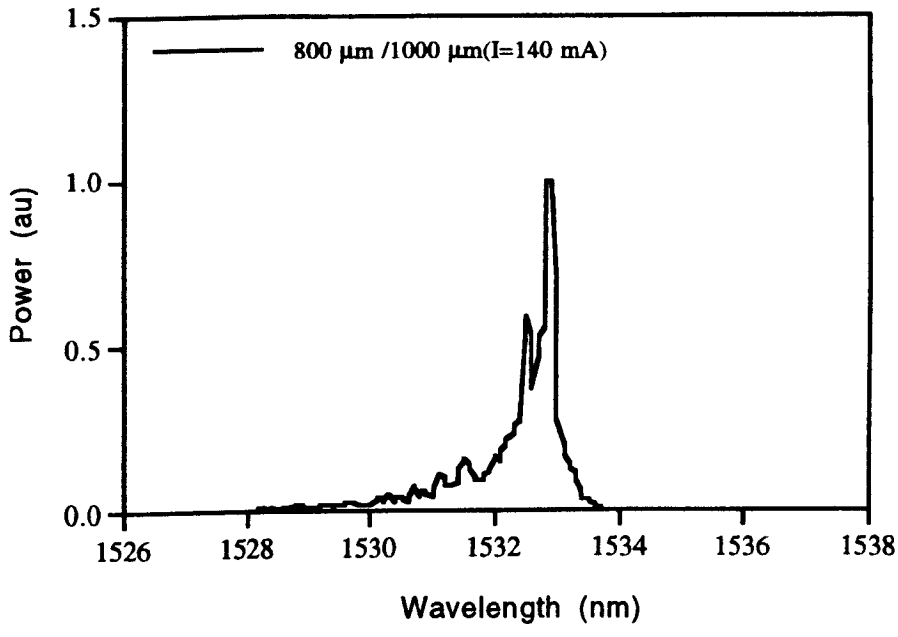

Fig. 7.13 Spectrum of an extended cavity laser.

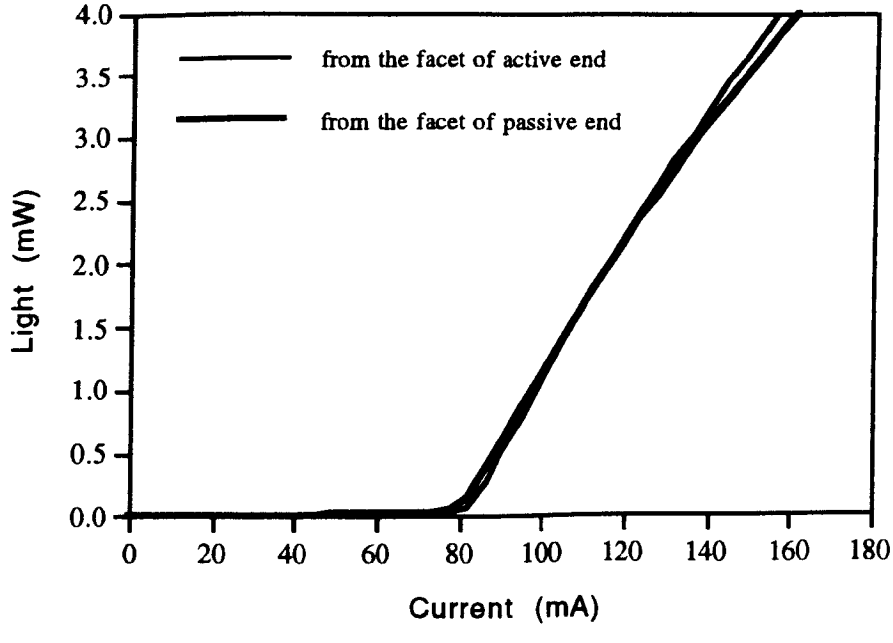

Fig. 7.14 Measured laser emission from the both facets of the extended cavity laser.

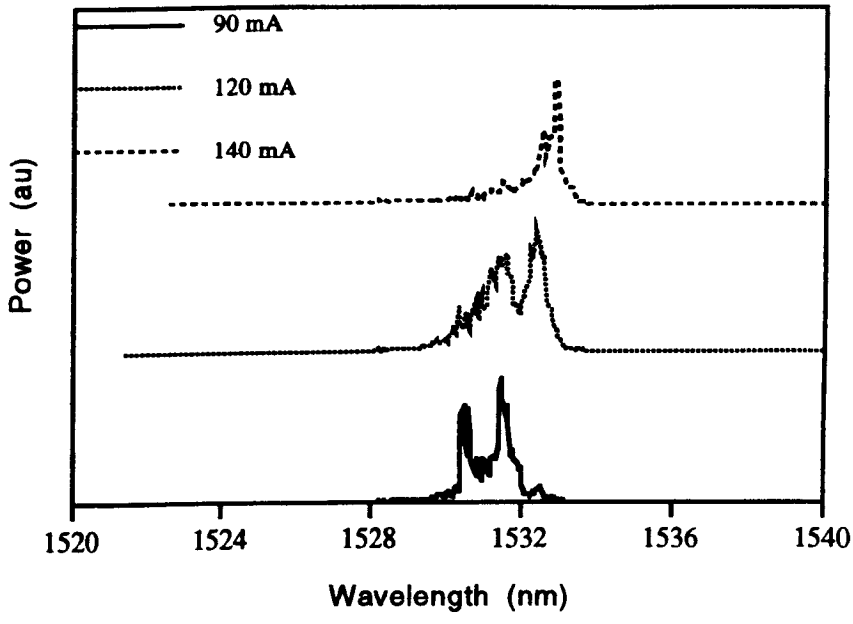

Fig. 7.15 Lasing spectra of the extended cavity laser from the facet of active end

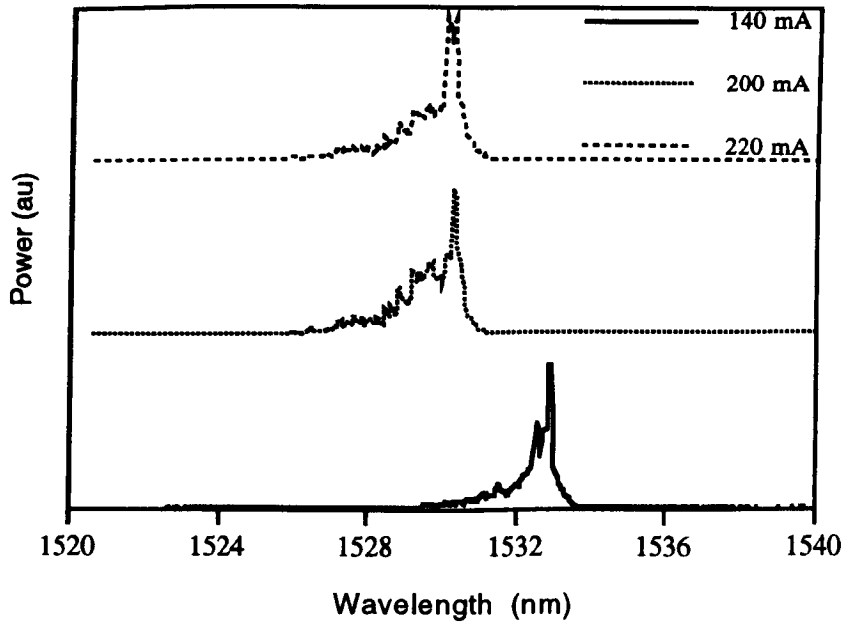

Fig. 7.16 Lasing spectra of the extended cavity laser from the facet of passive end

7.4.3 Discussions

As can be seen from Fig. 7.11, the increase in threshold current for the extended cavity ridge laser (ECL) with an active section length of 800 μm and 1000 μm long passive section is only 8 mA, compared to the all-active laser (AAL) with length of 800 μm. In the same fashion that the loss in the passive section was calculated using the Eq. (7.7) in section 7.3.4, the calculated loss in the passive section of the extended cavity lasers is 4.4 cm^{-1}. Comparing this value to the loss (being 2.4 cm^{-1}) in the passive section of the ECL using laser processing (see section 7.3.4), it seems the loss is considerably larger. We attribute this to the fact that different wafers were used to fabricate the devices; the material parameters of the wafers have considerably large difference (see table 6.2). Fig. 7.12 and Fig. 7.13 are the lasing spectra for the all-active laser and extended cavity laser, respectively. It is noticeable that a blue-shift of 24 nm of the spectrum occurs for the ECL, compared to that of AAL. As can be seen from Fig. 3.16 that QWI is almost completely suppressed in the gain regions, the blue-shift of the lasing spectrum of ECL is, therefore, assumed to be associated with the passive section of the device. This was verified by measuring the lasing spectrum after the passive section of the ECL was removed by cleaving. The spectrum moved back to the same position as that of lasing spectrum of the AAL, Fig. 7.14 shows $L-I$ curves measured from both cavity facets of the ECL. Essentially, the $L-I$ characteristics from both the facets are indistinguishable, given that the curves could not be measured simultaneously because of the arrangement of our experimental set-up. This suggests that the loss in the passive section is indeed low. Fig. 7.15 and Fig. 7.16 show the lasing spectra measured from both facets of the ECL under different current pumping conditions. The spectrum has a small red shift under lower pumping conditions (Fig. 7.15), but turns to have a blue shift at higher pumping levels (Fig. 7.16). From the figures, it can be seen that lasing spectra are identical at the same pumping level.

7.5 Conclusions

Extended cavity ridge lasers in InGaAs/InGaAsP multiple-quantum well structure have been successfully fabricated using two types of QWI technique, namely, a laser irradiation process using a combination of CW and Q-switched Nd:YAG lasers, and a plasma process. The increases in threshold current are only 10 mA and 8 mA, and the losses in the passive sections of ECLs were calculated to be 2.4 cm^{-1} and 4.4 cm^{-1} for the two respective processes. The loss in a bandgap widened single mode waveguide using the laser irradiation process was measured to be 2.1 cm^{-1}, and compared to that the calculated loss of 2.4 cm^{-1} in the passive section of the ECLs using the same process. This is essentially very good agreement.

References

1. J.H.Marsh, S.R. Andrew, S.G. Ayling, J. Beauvais, S.A. Bradshaw, A.C. Bryce, S.I. Hansen, R.M. De La Rue, R.W. Glew, " Neutral impurity disordering of III-V quantum-well structures for optoelectronic integration", Advanced III-V Compound Semiconductor Growth, Processing and Devices, 1992, **Ch. 133**, pp. 679-690

2. F. Camacho, E.A. Avrutin, P. Cusumano, A. Saher Helmy, A.C. Bryce, J.H. Marsh, "Improvements in mode-locked semiconductor diode lasers using monolithically integrated passive waveguides made by quantum-well intermixing", IEEE Photonic Technol. Lett., **9**, pp. 1208-1210, 1997

3. R.G. Walker, "Simple and accurate loss measurement technique for semiconductor optical wave-guides", Electron Lett. **21**, pp. 581-583, 1985

4. P. W. A. McIlroy, A. Kurobe, and Y. Uematsu, "Analysis and application of theoretical gain curves to the design of multi-quantum-well lasers IEEE J. Quantum Electron., QE-**21**, pp. 1958-1963, 1985

8. Conclusions and Future Work

8.1 Conclusions

This research has been concerned with the fabrication of monolithically integrated devices in InGaAs/InGaAsP MQW material structures using quantum well intermixing. To this end, a lot of work, including the development of a reduced damage RIE process, QWI using laser process and plasma process, fabrication of a wide range of devices such as low loss waveguides, 3-dB MMI couplers, ridge waveguide lasers, and extended cavity ridge lasers, was been carried out. The conclusions from this study are summarised below.

1. The damage introduced into an InGaAs/InGaAsP quantum well structure during CH_4/H_2 reactive ion etching (RIE) processes was measured, for plasma powers from 20 W to 100 W, using low temperature photoluminescence. The damage depth profile was estimated to be around 12 nm - 70 nm after annealing at 500 °C for 60 seconds using rapid thermal annealer (RTA). A reduced damage RIE process has been developed to fabricate InGaAs/InGaAsP multi-quantum well ridge waveguide lasers. The performance of these lasers has been compared to that of lasers fabricated from the same epilayer using wet etching to form the ridge. The resultant threshold currents were essentially indistinguishable, being 44.5 mA and 43 mA respectively for dry and wet etched lasers with 500 μm long laser cavities.

2. Quantum well intermixing in the InGaAs/InGaAsP material system was demonstrated using laser processes and plasma process. Photon-absorption induced disordering (PAID) is a reliable and reproducible process, the blue-shifts of up to 140 nm were obtained. However, unfortunately, the spatial selectivity is limited to around 100 μm. In contrast, the Pulsed-PAID (P-PAID) process offers much better spatial resolution, being about 20 μm, however, the intermixed material suffers from poor optical quality as is indicated by the reduced PL intensity and broader PL linewidth. The maximum intensity has dropped by a factor of 12, and the spectrum has broadened from 16 to 39 meV. In addition this process is less reproducible and more sensitive to the quality of the substrate of wafers. An alternative approach is to use the combination of P-PAID and PAID. This process offers similar yields to that of PAID. The plasma process has proven to be highly successful, in the sense of larger differential blue-shift (up to 120 nm), almost complete suppression of bandgap shift in control regions, as well as potentially high spatial resolution.

3. The design, fabrication and characterisation for 3-dB MMI couplers were carried out using both as-grown (peak emission wavelength of 1.48 μm) and bandgap widened material. The measured results show good agreement with the design. A splitting ratio of around 0.12 dB (51:49) has been achieved for the MMI section length of 470 μm.

4. Low loss waveguides have been fabricated using laser process. A loss as low as 2.1 dB/cm was obtained for the operational wavelength of 1.556 um.

5. Ridge waveguide lasers and 2-section ridge lasers were successfully fabricated using the RIE process developed in this work. Self pulsation of 2-section ridge lasers was observed.

6. Extended cavity ridge lasers in InGaAs/InGaAsP multiple-quantum well structures have been successfully fabricated using two types of QWI techniques, namely laser

irradiation processes using a combination of CW and Q-switched Nd:YAG lasers, and the plasma process. The increases in threshold current are only 10 mA and 8 mA, and the losses in the passive sections of ECLs were calculated which were 2.4 cm^{-1} and 4.4 cm^{-1}, for the two processes, respectively.

7. Considerable theoretical work was carried out, including the calculation of the optical confinement and gain in the InGaAs/InGaAsP MQW structure used through out this thesis. Modelling of the intermixing of quantum wells was also performed and the results indicate that the changes of bulk bandgap energy is the principal reason for the blue-shift of the PL.

8.2 Future Work

Further work needs to be carried out on the laser irradiation intermixing process to improve the spatial selectivity of the process. One of the possible approaches to this is to scan the laser beam, in this case, the laser beam can be focused to a considerably smaller size, and therefore the spatial selectivity is improved.

Based on the successful demonstration of QWI, the focus of future work should be shifted to the fabrication of various photonic integrated circuits, e.g. a 3-section ridge laser, in which a passive waveguide is monolithically integrated with a normal 2-section laser, can be used to generate high quality pulse streams in the range of tens of Gigabit which are needed in OTDM systems. The other device to be fabricated is an integrated terahertz optical asymmetric demultiplexer (TOAD). An important application of the TOAD is as a high speed demultiplexer in OTDM system. The operating speed of the device can be, in principle, up to terahertz frequencies.

References

1. F. Camacho, E.A. Avrutin, P. Cusumano, A. Saher Helmy, A.C. Bryce, J.H. Marsh, "Improvements in mode-locked semiconductor diode lasers using monolithically integrated passive waveguides made by quantum-well intermixing", IEEE Photonic Technol. Lett., **9**, pp. 1208-1210, 1997

2. J.P. Sokoloff, P.R. Prucnal, I. Glesk, and M. Kane, " A Terahertz optical asymmetric demultiplexer (TOAD)", IEEE photonic Technol. Lett., **5**, pp. 787-790, 1993

3. E. Jahn, N. Agrawal, H.-J., Ehrke, R. Ludwig, W. Pieper, and H.G. Weber, "Monolithically integrated asymmetric Mach-Zehnder interferometer as a 20 Gbit/s all-optical add/drop multiplexer for OTDM", Electron. Lett., **32**, pp. 216-217, 1996